

South Dakota State University

Open PRAIRIE: Open Public Research Access Institutional Repository and Information Exchange

Electronic Theses and Dissertations

2020

Lithium-Ion Battery and Beyond: Oxygen Vacancy Creation in Tungsten Trioxide and Surface Modification of Lithium Metal

Rajesh Pathak
South Dakota State University

Follow this and additional works at: <https://openprairie.sdstate.edu/etd>



Part of the [Power and Energy Commons](#)

Recommended Citation

Pathak, Rajesh, "Lithium-Ion Battery and Beyond: Oxygen Vacancy Creation in Tungsten Trioxide and Surface Modification of Lithium Metal" (2020). *Electronic Theses and Dissertations*. 4854.
<https://openprairie.sdstate.edu/etd/4854>

This Dissertation - Open Access is brought to you for free and open access by Open PRAIRIE: Open Public Research Access Institutional Repository and Information Exchange. It has been accepted for inclusion in Electronic Theses and Dissertations by an authorized administrator of Open PRAIRIE: Open Public Research Access Institutional Repository and Information Exchange. For more information, please contact michael.biondo@sdstate.edu.

LITHIUM-ION BATTERY AND BEYOND: OXYGEN VACANCY CREATION IN
TUNGSTEN TRIOXIDE AND SURFACE MODIFICATION OF LITHIUM METAL

BY

RAJESH PATHAK

A dissertation submitted in partial fulfillment of the requirements for the

Doctor of Philosophy

Major in Electrical Engineering

South Dakota State University

2020

DISSERTATION ACCEPTANCE PAGE

Rajesh Pathak

This dissertation is approved as a creditable and independent investigation by a candidate for the doctoral degree and is acceptable for meeting the dissertation requirements for this degree. Acceptance of this does not imply that the conclusions reached by the candidate are necessarily the conclusions of the major department.

Yue Zhou
Advisor

Date

Siddharth Suryanarayanan
Department Head

Date

Nicole Lounsbery, PhD
Director, Graduate School

Date

ACKNOWLEDGMENTS

First of all, I would like to thank my advisors Yue Zhou and Qiquan Qiao for their constant inspiration and encouragement during my Ph.D. career. Their dedication to research has profoundly influenced me in many aspects. I would not have achieved as much without their guidance. The whole research has been supported by NSF MRI (1428992), NASA EPSCoR (NNX15AM83A), SDBoR Competitive Grant Program, SDBoR R&D Program, and EDA University Center Program (ED18DEN3030025).

I would like to thank Associate Prof. Parashu Kharel and Assistant Prof. Rachel Willand Charnley for agreeing to serve on my Dissertation Committee and giving me their valuable time and feedback for my Ph.D. work.

It is also my great pleasure to work with many of the wonderful people in the group. Among many others, I would like to thank Ke Chen, Ashim Gurung, Khan Mamun Reza, Behzad Bahrami, Abiral Baniya, Nabin Ghimire, Jyotshna Pokharel, Buddhi Sagar Lamsal, Wei He, Md Tawabur Rahaman, and Ahmed Ali El-Magrous for their generous help. I have also spent a lot of memorable time working in the lab and hanging out with them.

I would like to thank my parents Min Raj Pathak, Bhagrathi Pathak, Bhawana Pathak, and Shiv Raj Pathak for their love and support, despite being thousands of miles away. The special thanks go to my wife Jaya Krishna Yakha for her tremendous support, love, and encouragement.

TABLE OF CONTENTS

ABBREVIATIONS	viii
LIST OF FIGURES	x
LIST OF TABLES.....	xv
ABSTRACT.....	xvi
CHAPTER 1: INTRODUCTION	1
1.1 Background	1
1.2 Introduction to Lithium-ion batteries and beyond	3
1.3 Literature review	6
1.3.1 Lithium-ion battery.....	6
1.3.2 Beyond Lithium-ion battery	8
1.3.2.1 Nano/microstructured Li host	8
1.3.2.2 Solid-state electrolyte.....	11
1.3.2.3 Solid-electrolyte interphase	13
1.3.2.3.1 <i>In-situ</i> formation of SEI	14
1.3.2.3.2 <i>Ex-Situ</i> formation of SEI	17
1.4 Motivation.....	24
1.5 Objective	24
1.6 Organization of the Dissertation	25
CHAPTER 2: THEORY	27

2.1	Components and working principle of Li-ion batteries	27
2.2	Important parameters for evaluating battery performance.....	28
2.2.1	Specific capacity	28
2.2.2	Coulombic efficiency and Cycle life	29
2.2.3	Voltage.....	29
2.2.4	Energy density	29
2.2.5	Power density.....	30
2.3	Material characterizations.....	30
2.3.1	X-ray diffraction Spectrum (XRD).....	30
2.3.2	Field emission scanning electron microscopy (FESEM).....	30
2.3.3	Energy dispersive spectroscopy (EDS).....	31
2.3.4	Braunauer Emmett and Teller measurement.....	31
2.3.5	X-ray photoelectron spectroscopy	32
2.3.6	Raman Spectroscopy.....	33
2.3.7	Fourier transform infrared spectroscopy.....	34
2.4	Electrochemical characterizations	34
2.4.1	Cyclic voltammetry	34
2.4.2	Electrochemical impedance spectroscopy	35
2.4.3	Symmetrical cell test	35
2.4.4	Half-cell or Full cell test.....	36

CHAPTER 3: EXPERIMENTAL PROCEDURES.....	37
3.1 Materials and preparation	37
3.1.1 Anode electrode fabrication for LIBs.....	37
3.2 Development of solid-electrolyte-interphase.....	38
3.2.1 Physical deposition.....	38
3.2.2 Chemical deposition	40
3.2.2.1 Materials and preparations.....	40
3.2.2.2 Cathode electrode fabrications for LMBs.....	41
3.3 Material characterizations.....	42
3.3.1 X-ray diffractometer	42
3.3.2 Field emission/-scanning electron microscopy and energy dispersive spectroscopy.....	43
3.3.3 Atomic force microscopy	44
3.3.4 Raman spectroscopy.....	45
3.3.5 UV-visible spectrum spectroscopy.....	46
3.3.6 X-ray photoelectron spectroscopy	46
3.3.7 Brunauer Emmett and Teller	47
3.4 Electrochemical characterizations	47
3.4.1 Cyclic voltammetry and electrochemical impedance spectroscopy	47
3.4.2 Symmetrical cell and full cell test	48

CHAPTER 4: RESULTS AND ANALYSIS	50
4.1 Self-recovery of capacity in the WO ₃ anode material	50
4.1.1 Structural characterization.....	50
4.1.2 Electrochemical characterizations	52
4.2. Development of <i>ex-situ</i> ASEI by a physical deposition method	57
4.2.1 Material characterizations.....	58
4.2.2 Electrochemical characterizations	64
4.3 Development of <i>ex-situ</i> ASEI by a physical deposition method	76
4.3.1 Material characterization	76
4.3.2 Electrochemical characterization.....	81
CHAPTER 5: SUMMARY AND CONCLUSIONS	91
5.1 Summary	91
5.2 Conclusions.....	93
5.3 Future Work	96
References	98

ABBREVIATIONS

LIB	lithium ion battery
LMB	lithium metal battery
LMA	lithium metal anode
WO ₃	Tungsten trioxide
AFM	atomic force microscopy
FESEM	field emission scanning electron microscopy
CV	cyclic voltammetry
EIS	electrochemical impedance spectroscopy
XRD	X-ray diffraction
EDS	energy dispersive spectroscopy
3D	3-dimension
SEI	solid electrolyte interphase
R-F	radio frequency
DC	direct current
ALD	atomic layer deposition

PLD	pulsed laser deposition
CVD	chemical vapor deposition
XPS	x-ray photoelectron spectroscopy
LTO	lithium titanate
SnF ₂	tin fluoride
SiO ₂	silicon dioxide
PVDF	polyvinylidene fluoride
NMC	lithium nickel cobalt manganese oxide
NMP	N-Methyl-2-pyrrolidone
RMS	root mean square
SEI	solid electrolyte interphase
ASEI	artificial solid electrolyte interphase
R _{ct}	charge transfer resistance
CuCF	copper clad carbon foam

LIST OF FIGURES

Figure 1. 1: (a) Prediction of primary energy consumption by sources across the globe up to 2050 and (b) Comparison of the energy consumption by percentage among the energy sources between the years 2018 and 2050.	2
Figure 1. 2: (a) Bar diagram showing the specific energy and energy densities (blue) and the specific energy (purple) , (b) Cell-level specific capacity based on the cell's parameter and component , (c) Different issues associated with Li metal anode and (d) possible solution to the challenges associated with Li metal anode.	5
Figure 1. 3: (a-c) Nucleation overpotential and (d-f) corresponding SEM images after a plating capacity of 4 mAh cm^{-2}	11
Figure 1. 4: (a-d) Schematic demonstration of Li-ion battery using liquid electrolyte and solid-state electrolyte , (e) Key challenges in solid-state battery, and (f-k) Radar plots showing the performance of different solid-state electrolyte.	13
Figure 1. 5: (a) SEI formation due to the direct contact of the Li electrode and electrolyte during charge/discharge cycles, (b) schematic illustration of SEI properties in an ideal SEI and (c-e) the schematic of SEI mechanism in the Peled model, Mosaic model, and Coulombic interaction model, respectively.	17
Figure 1. 6: Schematic illustrations of <i>ex-situ</i> artificial SEI on top of Li metal anode by (a) physical deposition and (b) chemical deposition process.	19
Figure 2. 1: Schematic illustration of the working mechanism in Li-ion battery.	28

Figure 3. 1: Schematic demonstration of Li deposition behavior: a) on bare Li anode, and b) on graphite-SiO ₂ bilayer sputtered Li metal anode.	40
Figure 3. 2: Schematic illustrations of Li dendrites' growth on (a) bare Li and (b) smooth Li deposition on artificial SEI protected Li.	42
Figure 3. 3: Picture showing the X-ray diffractometer located in the Lab at SDSU.	43
Figure 3. 4: Picture of a Hitachi S-3400N SEM EM and b Hitachi S-4700N FESEM located in the cleanroom at SDSU.....	44
Figure 3. 5: Picture of AFM located in DEH 053 at SDSU.....	45
Figure 3. 6: Experimental setup for the Horiba Raman system in the Lab at SDSU.....	46
Figure 3. 7 The picture of VERSASTAT and EC-Lab device for measuring CV and EIS.....	48
Figure 3. 8 Picture showing the Neware battery analyzer used for galvanostatic charge and discharge.	49
Figure 4. 1: (a) XRD patterns, (b) Raman spectra and (c-d) AFM surface topography for P-WO ₃ , and R-WO ₃ , and (e,f) shows the high-resolution AFM of (c-d).....	51
Figure 4. 2: Electrochemical battery cycling performance at (a) constant rate, (b) different rates, (c,d) corresponding CE and (e,f) corresponding voltage profile.....	54
Figure 4. 3: (a,c) CV measurement b,d voltage versus specific capacity, (e) Tauc plot, and (f) Nyquist plot of P-WO ₃ and R-WO ₃	56
Figure 4. 4: (a) Electrochemical cycling performance of R-WO ₃ , (b) corresponding voltage profile, (c,d) SEM images of the R-WO ₃ electrode before and after observing self-recovery,	

and (e) XRD of Kapton tape, the R-WO₃ electrode before cycling, and after 17th discharge.

..... 57

Figure 4. 5: (a) Raman spectroscopy of graphite sputtered on Li, (c-d) XPS analysis of graphite and SiO₂ sputtered on Li and (e,f) Contact angle measurement of bare Li and graphite-SiO₂ Li using electrolyte solvent..... 59

Figure 4. 6: SEM images of (a) bare Li and (b) graphite-SiO₂ Li, corresponding AFM images of (c) bare Li and (d) graphite-SiO₂ Li, (e,f) corresponding Young's modulus measurement of bare Li and graphite-SiO₂ Li, SEM image of (g, h) bare Li and (i, j) graphite-SiO₂ Li after 1st plating and 100th plating and (k) XRD of the graphite-SiO₂ Li.

..... 61

Figure 4. 7: SEM images of (a,c) bare Li (b,d) graphite SiO₂ Li after 100th plating /stripping cycles and (e) high-resolution SEM image of bare Li showing the scratches and dents in bare Li. 62

Figure 4. 8: (a,b) XPS analysis on the graphite-SiO₂ electrode before and after the 50th plating and 50th stripping cycle and (c) CV measurement of graphite-SiO₂ Li electrode for 5 cycles..... 64

Figure 4. 9: Symmetrical cell test with different thicknesses of (a) SiO₂ and (b) graphite.

..... 65

Figure 4. 10: (a) Air and (b) liquid electrolyte stability of a bare Li and graphite-SiO₂ Li.

..... 66

Figure 4. 11: (a,b) Nyquist plot a,b as a function of days, (c) Nyquist after 10 cycles of plating/stripping cycles, (d,e) plating/stripping cycle and corresponding voltage hysteresis

at a current density of 0.5 mA cm^{-2} and (f,g) plating /stripping cycle and corresponding voltage hysteresis at a current density of 1 mA cm^{-2}	70
Figure 4. 12: Symmetrical cell plating/stripping performance at various current densities and capacities.	71
Figure 4. 13: Symmetrical cell plating/stripping performance at various current density to achieve a capacity of 1 mAh cm^{-2}	72
Figure 4. 14: Electrochemical battery cycling performance using bare Li and graphite-SiO ₂ Li paired with NMC and LTO cathodes.	73
Figure 4. 15: Rate capability test of NMC cathode paired with bare Li and graphite-SiO ₂ Li and (b,c) Corresponding charge/discharge voltage curve at a different rate.....	74
Figure 4. 16: (a) Rate capability test of LTO cathode paired with bare Li and graphite-SiO ₂ Li and (b,c) corresponding discharge/charge voltage curve at a different rate.....	75
Figure 4. 17: XRD and XPS analysis of pristine Li and after drop cast of SnF ₂	77
Figure 4. 18: (a-d) Photographic digital images, e-h surface topography SEM images, and (i-l) cross-sectional SEM images of bare Li and surface topography SEM images after 1 st plating of Li in bare Li and SnF ₂ pretreated Li with different concentrations.....	78
Figure 4. 19: (a,b) AFM measurement of bare Li and AFH-25 and (c,d) corresponding Young's modulus measurement.....	79
Figure 4. 20: (a,b) Contact angle measurement of bare Li and AFH-25 Li with electrolyte solvent and (c) LSV measurement of bare Li and AFH-Li electrode.....	80

Figure 4. 21: (a) Symmetrical cell test of bare Li, 1, 3, and 5 wt% of SnF ₂ treated Li, and (b-d) Nyquist plot of symmetrical cells at fresh condition, after 10 th cycle and after 50 th cycle of plating/stripping.	82
Figure 4. 22: (a,b) Equivalent circuit for fitting the Nyquist plot and Nyquist plot of the symmetrical cell as a function of hours for (c) bare Li and (d) AFH-25 Li.	83
Figure 4. 23: SEM iamges of (a-c) bare Li and (d-f) AFH-25 Li after 1 st , 10 th and 100 th plating.	84
Figure 4. 24: (a,b) Symmetrical cell test of bare Li and AFH-25: Inset shows the first five plating/stripping cycles, and (c,d) corresponding voltage hysteresis.	85
Figure 4. 25: Symmetrical cell tests at various current densities and capacities.	86
Figure 4. 26: (a) Symmetrical cell test at various current densities from 0.5 to 5 mA cm ⁻² to achieve a constant capacity of 1 mAh cm ⁻² and (b) The zoomed plating /stripping in the beginning hours.....	87
Figure 4. 27: CV measurement of (a) bare Li and (b) AFH-25 symmetrical cells.	88
Figure 4. 28: (a,b) Cross-sectional SEM images and corresponding elemental mapping after 100 cycles of plating/stripping in bare Li and AFH-25 Li symmetrical cell.	89
Figure 4. 29: (a-c) Full cell battery performance at a constant rate and corresponding voltage profiles and (d-f) Full cell battery performance at a different rate and corresponding voltage profiles.....	90

LIST OF TABLES

Table 1. 1 Summary of the artificial SEI engineered by a surface coating method.	20
Table 1. 2 Summary of the artificial SEI engineered by surface chemistry method.	22
Table 4. 1 Weight percentage of oxygen (O) and tungsten (W) in P-WO ₃ and R-WO ₃	52
Table 4. 2 Rate capability test of P-WO ₃ and R-WO ₃	54
Table 4. 3 Table showing the average Young's modulus and RMS roughness.	60
Table 4. 4 Impedance results of the symmetrical cell using bare Li and graphite-SiO ₂ Li.	69
Table 4. 5 Charge/discharge capacity of the full cell at different rates using NMC cathode.	75
Table 4. 6 Charge/discharge capacity of the full cell at different rates using LTO cathode.	76

ABSTRACT

LITHIUM-ION BATTERY AND BEYOND: OXYGEN VACANCY CREATION IN
TUNGSTEN TRIOXIDE AND SURFACE MODIFICATION OF LITHIUM METAL

RAJESH PATHAK

2020

The graphite-based anode material has a low theoretical specific capacity of 371 mAh g^{-1} . The transitional metal oxides (TMOs) are considered a better choice owing to their relatively higher specific capacity. Among TMOs, tungsten trioxide (WO_3) is considered promising due to a higher specific capacity of 693 mAh g^{-1} , low cost, mechanically stable, and eco-friendly. It has been a challenge to utilize the TMOs as anode materials as they suffer from poor electronic conductivity and large electrode volume expansion during discharge/charge cycles. In our first project, we demonstrate a unique self-recovery of capacity in reduced WO_3 by the incorporation of urea followed by annealing at 500°C under the N_2 environment. The reduced WO_3 exhibited a unique cycling phenomenon, where the capacity was significantly self-recovered after an initial sharp decrease. This can be attributed to the activation of oxygen vacancy sites or defects, making the WO_3 electrode more electrochemically active with cycling. In our second and third projects, we modify the surface of lithium metal to utilize them as anode because LIBs are approaching their theoretical energy density limit. Lithium metal anodes are expected to drive practical applications that require high energy-density storage. However, the direct use of metallic lithium causes safety concerns, low rate capabilities, and poor cycling performances due to unstable solid electrolyte interphase (SEI) and undesired lithium dendrite growth. To address these issues, in our second project, radio frequency (R-F) sputtered graphite- SiO_2

ultrathin bilayer on a Li metal chips was demonstrated, for the first time, as an effective solid-electrolyte interface (SEI) layer. In the third project, we developed a facile, cost-effective, and one-step approach to generate an artificial lithium metal/electrolyte interphase by treating lithium anode with an electrolyte containing tin fluoride. The development of artificial SEI on top of lithium metal anode led to a dendrite free uniform Li deposition to achieve a stable voltage profile and outstanding long hours plating/stripping compared to the bare Li. The generated SEI not only ensures fast lithium-ion diffusion and suppression of lithium dendrite growth but also brings a synergistic effect of storing lithium via a reversible silicon-lithium or tin-lithium alloy formation and lithium plating.

Keywords: Lithium-ion battery, tungsten trioxide, lithium metal battery, physical deposition, chemical deposition, stable solid electrolyte interphase, dendrite-free Li deposition.

CHAPTER 1: INTRODUCTION

1.1 Background

Energy is very essential to sustain daily life activities, which includes various consumer applications such as tablets, and laptops to industrial applications such as long-drive electric vehicles and large-scale energy storage micro-grids. To meet the ever-increasing energy demand, fossil fuels such as oil, kerosene, and petroleum are being widely exploited. The excessive use of fossil fuel leads to global warming and the exhaustion of limited fossil fuels. The replacement of fossil fuels with renewable energy sources in reducing global CO₂ emission is critical. The International Energy Agency (IEA) pronounced that the production of CO₂ from the transportation and power generation area needs to be reduced by 21% and 42%, respectively, by 2050 to relish a sustainable future [1, 2]. This is to say that the extensive use of diesel or petrol-based vehicles are to be replaced by electric-based vehicles. Thus, it is very essential to utilize abundant renewable energy sources which include wind, hydropower, and solar. The low cost and ecofriendly renewable sources are considered as promising energy sources. The widespread renewable sources provide the opportunity for energy production, but we are not able to utilize them instantly and it is challenging to store them for the future. Extensive research is going on to harvest renewable energy sources and it is believed that renewable energy consumption will increase from 15% in 2018 to 28% by 2050 [3]. Figure 1.1(a) shows the prediction of primary energy consumption by sources across the globe up to 2050. Figure 1.1(b) shows the comparison of the energy consumption by percentage among the energy sources between the years 2018 and 2050.

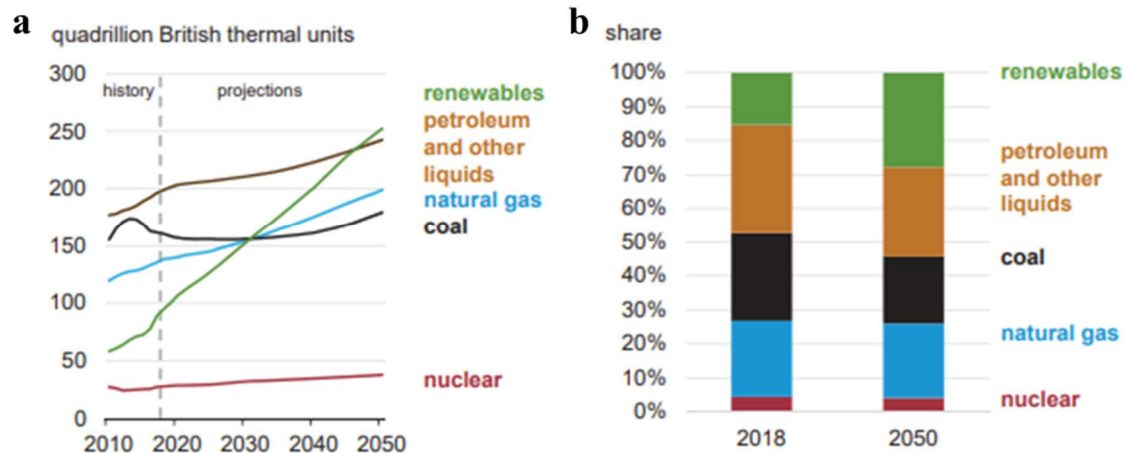


Figure 1. 1: (a) Prediction of primary energy consumption by sources across the globe up to 2050 and (b) Comparison of the energy consumption by percentage among the energy sources between the years 2018 and 2050 [3].

However, it is not possible to harness renewable energy whenever we need them because they are constrained on the location and weather. For example, we cannot harvest solar energy at night, cloudy time, or in the winter season. Similarly, wind and hydropower are not available everywhere on earth. For an uninterrupted supply of energy, an energy storage device is required which can store the harvested renewable energy and supply in the form of electrical energy. There is continuous increasing market demand for an electric energy storage device in transportation, grid storage, and residential power-backup applications. To bring the existence of electric vehicles in large scale and grid storage of harvested renewable energy, the development of high-energy-density energy and power density storage devices are crucial [4-7]. Among various energy storage devices, lithium-ion batteries (LIBs) are considered promising energy storage devices due to their high specific energy density (lighter weight) and high volumetric energy density (smaller size).

1.2 Introduction to Lithium-ion batteries and beyond

During the 1980s, the conventional rechargeable batteries such as lead-acid, nickel-cadmium, and nickel-metal hydride were on the stage of development. These energy storage devices were not efficient to meet the growing demands of recharging portable electronics such as video cameras and notebook computers. The alternative energy storage technology with higher capacity, smaller size, and lesser weight was needed. Substantial efforts were done to convert the metallic lithium battery into a secondary battery. However, the lithium precipitation forming lithium-dendrites on the negative electrode during charging, infinite lithium volume expansion issues, and the highly reactive nature of lithium hinder its further practical application. Whittingham et al. demonstrated the first rechargeable LIB using lithium metal as anode and TiS_2 as a cathode at Exxon Corporation in the USA [8]. Goodenough and the worker reported the use of LiCoO_2 as cathode material in 1979. Yazami and Touzain demonstrated the intercalation/deintercalation of lithium into graphite in 1982. In 1986, Yoshino et al. designed a non-aqueous secondary LIB using LiCoO_2 as a cathode and carbonaceous material as an anode [9]. The tireless effort for the development in the rechargeable Li-ion battery results in the commercialization of LIB by SONY in 1991. Three chemists Goodenough, Yoshino, and Whittingham were awarded the Nobel Prize in Chemistry-2019 for their great contribution to the development of LIB technology [10].

The current state-of-art LIBs are reaching their theoretical energy density of $\sim 350 \text{ Wh kg}^{-1}$ at the cell level. This amount of energy density is not sufficient to drive the long-range electric vehicles and other high energy density requiring applications such as microgrid. Thus, it is imperative to research the alternative to Li-ion battery technology. The

replacement of conventional graphite-based anode material with lithium metal anode is considered as a promising strategy to obtain a high energy density of 500 Wh kg⁻¹ or higher. Lithium metal anode (LMA) based batteries are considered high energy density batteries owing to the high theoretical specific capacity (3860 mAh g⁻¹), the most negative electrochemical potential (-3.04 V vs the standard hydrogen electrode), and low mass density (0.534 g cm⁻³) of Li. The lithium metal batteries (LMBs) paired with aggressive cathodes with a high voltage such as lithium nickel manganese oxide (LiNMO) or high capacity such as Lithium-sulfur/air (Li-S/air) can fulfill the immediate demand of today's industrialized world. Figure 1.2(a) shows the bar chart showing the practical specific energy (pink) and energy densities (blue) of gasoline, rechargeable Li-ion, and various LMBs such as Li-Lithium manganese oxide (LMO), Li-S, and Li-air batteries [11]. Although the Li-S and Li-air (O₂) battery demonstrated high energy density, the battery design and operating system are very complex in this energy technology. Such energy storage technologies are still considered in the infancy period. Similarly, Figure 1.2(b) shows the calculated cell-level specific energy as a function of cell component and parameter [12]. The specific energy density not only depends on the type of anode but also the type of cathode, amount of lithium & electrolyte, and the mass loading of the cathodes. For practical high energy density batteries, lean lithium, lean electrolyte, and high mass loading cathode are considered promising.

Although the LMA is considered as a promising anode material for next-generation Li-ion batteries, it has numerous issues which hinder its further practical applications. As shown in Figure 1.2(c), LMA is highly reactive that leads to the side reaction and consumption of both Li and electrolyte. This leads to low Coulombic efficiency (CE) and quick capacity

fading. Besides, the infinite volume expansion issues of Li metal lead to the pulverization of the electrode and formation of unstable solid electrolyte interphase (SEI). Moreover, the uncontrolled Li deposition leads to Li dendrite growth which can consume excess electrolyte and also can pierce the separator challenging the safety concern of the battery. The formation/deformation of SEI and detrimental Li dendrite growth hinders the practical use of Li metal as an anode in beyond Li-ion batteries.

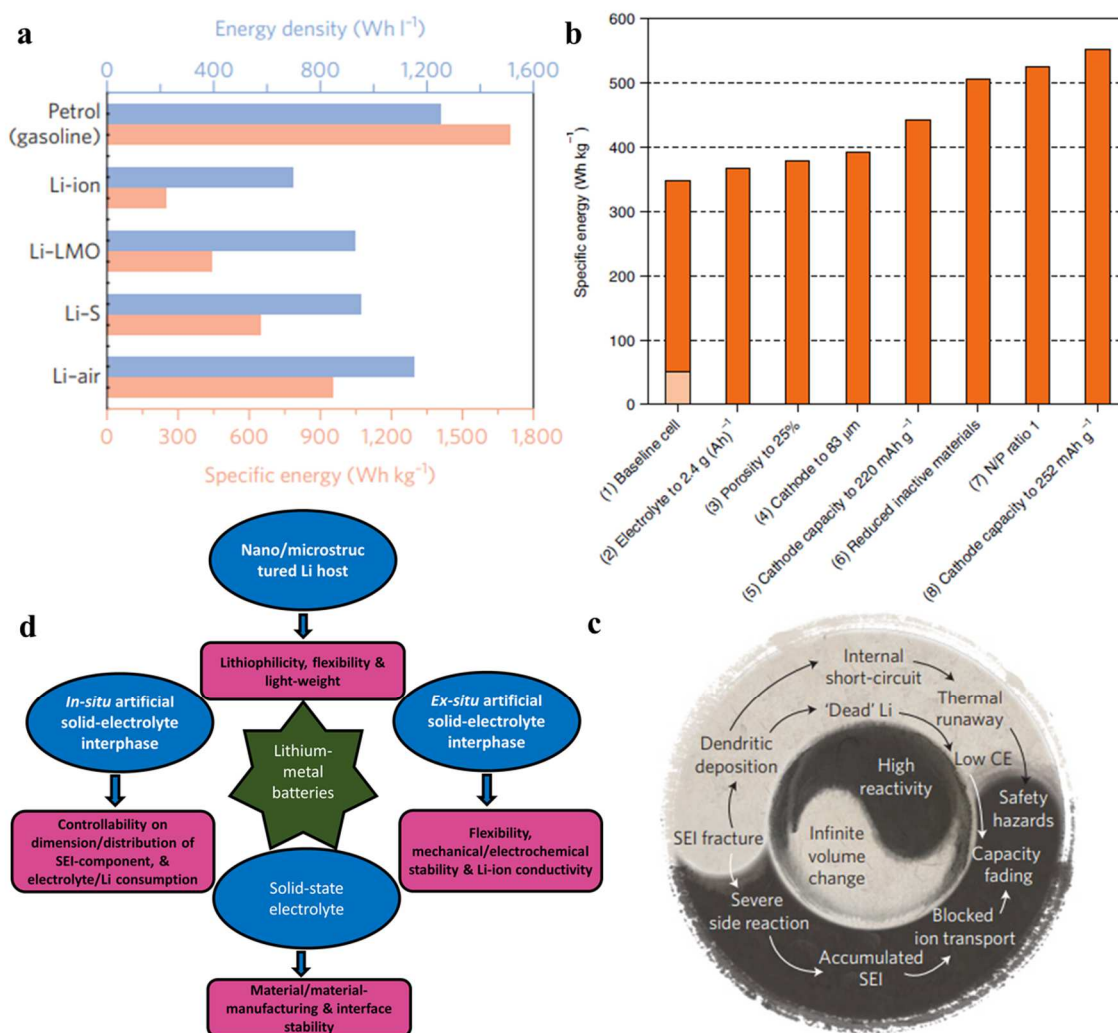


Figure 1. 2: (a) Bar diagram showing the specific energy and energy densities (blue) and the specific energy (purple) [11], (b) Cell-level specific capacity based on the cell's

parameter and component [12], (c) Different issues associated with Li metal anode [11] and (d) possible solution to the challenges associated with Li metal anode.

Substantial efforts have been made by a larger and growing number of researchers to address the inherent issues related to the LMA to achieve the potential application of LMBs as shown in Figure 1.2(d). For guiding the uniform Li deposition and improved cycling performance, the common approaches are: (1) the development of lithiophilic and conductive three dimensional (3D) micro/nanostructured framework to guide the uniform Li deposition and accommodate the volume expansion; (2) the engineering of an artificial protective layer on top of Li by *ex-situ/in-situ* can greatly inhibit the side reactions; (3) the development of solid-state electrolyte, and (4) other strategies such as modification of separator, and defining the battery testing conditions.

1.3 Literature review

1.3.1 Lithium-ion battery

Lithium-ion battery (LIB) technology is considered as one of the most promising energy storage devices owing to its high gravimetric and volumetric energy density. The capacity storage mechanism in LIBs mainly includes three mechanisms such as intercalation (graphite), alloying (silicon), and conversion (WO_3). Thanks to the low cost and high stability of the graphite as an anode (with theoretical specific capacity 372 mAh g^{-1}) [13]. Although silicon has the highest theoretical specific capacities of 4200 mAh g^{-1} and 990 mAh g^{-1} respectively, it suffers from large volume expansion of $\sim 400 \%$ during charge/discharge cycles which is detrimental for battery performance [14, 15].

Numerous transitional metal oxides (TMOs) such as Fe_3O_4 [16], SnO_2 [17], MoO_3 [18], NiO [19], and Co_3O_4 [20] have been widely studied as anode materials in LIBs. Despite

the attractive features, TMOs suffer mainly from the poor electronic conductivity and large electrode deterioration resulting from volume expansion of the electrode during charge/discharge cycles [21-23]. Besides, the formation of unstable solid-electrolyte interphase (SEI) and irreversible capacity leads to the consumption of electrolyte, leading to low coulombic efficiency (CE) and quick capacity fading [17, 24]. The formation of insulating Li_2O increases the cell's impedances and highly irreversible capacity.

Among various TMOs, WO_3 has attracted great attention as a potential anode in LIBs owing to its high theoretical capacity (693 mAh g^{-1}), environmentally friendliness, and low cost. Besides, the high melting point and strong mechanical stability of WO_3 provides better safety [25, 26]. The different preparation and modification on WO_3 anode material have been reported such as porous single-crystalline nanoplates [27, 28], nanostructured thin films [29], core-shell [30], both Chrysanthemum-like and cookie-like [24, 31], composite using graphene [21], micro flowers and nanowires [28], nanoparticles [32] and hexagonal ultrathin nano-ribbons [33]. Scientists are still struggling to achieve a high practical specific capacity with long-term stable cycling performance.

The use of urea and/or N_2 doping has been investigated in anode or cathode electrodes as the source of carbon increasing the catalytic activity of the active materials. Such pretreatment has introduced secondary particles with smaller particle sizes increasing the surface area, and porosity in the materials, resulting in improved battery performance. In our study, the improved catalytic performance was obtained by using urea which produces ammonia gas while annealing at 500°C , and also annealing was done under N_2 . There has never been a report on the incorporation of both urea and nitrogen treatment for WO_3 . The

synergetic effect of urea and N₂ doping helps to create excess oxygen vacancies, increasing the defect sites, and catalytic activity in the electrode material.

1.3.2 Beyond Lithium-ion battery

Lithium-ion batteries (LIBs) are established as the leading energy storage device all over the world. The ever increasing demand for high energy density batteries urges the coupling of ultimate metallic Li anode, and high capacity and/or voltage cathode. However, the use of Li metal anode challenges the safety concern and stable battery performance due to its hyperactive nature and infinite volume expansion issues. It is highly recommended to develop the three-dimensional (3D) Li host, utilize the solid-state electrolyte (SSE), or develop the artificial solid interphase (SEI) for addressing the aforementioned issues of Li metal anode.

1.3.2.1 Nano/microstructured Li host

The development of three-dimensional (3D) nano/microstructured metal-based or carbon-based Li hosts has proven to be a successful technique to accommodate the dendrite-free Li deposition [34]. The uniform distribution of the electric field leads to the Li-ion flux distribution. Besides, the high surface area of the interconnected porous framework provides sufficient space to constrain the Li dendrite growth with much high areal capacity deposition, and significantly lowers the current density. In contrast, the planar current collectors have rough and uneven surfaces creating a non-uniform electric field. The large protuberance or cracks act as a hotspot for the non-uniform Li-ion flux distribution, resulting in inhomogeneous Li deposition. The most commonly used current collectors are metal or carbon-based porous frameworks which show a poor affinity towards Li metal. The poor Li-wettability of the porous framework cannot uniformly

guide the initial Li deposition, leading to large nucleation overpotential, and subsequent large voltage hysteresis during the higher plating/stripping cycles. Various approaches to using lithophilic coating or decorations on the porous framework have been reported to guide the uniform Li deposition. For example, the use of metal oxide-based, metal nitride-based lithophilic materials, heterogeneous doping, and the functional group-containing compounds have significantly improved the Li deposition behavior. Some metal (nitrides or oxides) based lithophilic material can guide the uniform Li deposition through the conversion or alloying reaction. However, the formation of Li_2O during the conversion of alloying reaction is considered detrimental for achieving high CE. The metal-based Li host/current collector has higher mass density, high processing cost, and complex processing techniques compared to the carbon-based Li host/current collector[34]. Free-standing carbon-based materials with lithophilic decorations are considered suitable for making Li/C composite anode. The mainly used techniques for making Li/C composites are (1) Li electrodeposition, (2) molten Li infusion, and (3) mechanical roll pressing. The Li electrodeposition is not only tedious and time-consuming but also suffer from non-uniform Li deposition in the Li/C composite anode. The molten Li infusion into the free-standing porous carbon with lithophilic doping/decorations is considered a better approach than the Li electrodeposition as it does not involve disassembling the battery, cleaning the electrode before assembling the full cell. Moreover, the uniform Li deposition is expected while infusing the molten Li into the porous lithophilic carbon structure. However, the risk and use of high temperatures for melting the Li is always challenging. The simple technique for making Li/C composite is the mechanical and roll press of Li into the porous structure. Moreover, the Li/C composite can be further

modified by the formation of in-situ/ex-situ based SEI, which significantly improves the electrochemical battery performance. In our previous work, we reported the copper-coated carbon foam, where the melamine-formaldehyde foam was pyrolyzed to obtain the carbon foam (CF) followed by electroplating of Cu on CF to obtain copper clad carbon foam (CuCF). Figures 1.3 (a-c) show the nucleation overpotential of Li plating at 0.5 mA cm^{-2} to reach a capacity of 4 mAh cm^{-2} on planar Cu, CF, and CuCF current collector. It can be observed that CuCF shows the least nucleation overpotential. This can be attributed to various factors such as high electronic conductivity, high porous structure, and lithiophilic nature of CuCF. Figures 1.3(d-f) show SEM images of the corresponding current collector after plating 4 mAh cm^{-2} capacity. The CuCF current collector or Li host shows the uniform and dendrite-free Li deposition compared to planar Cu and CF.

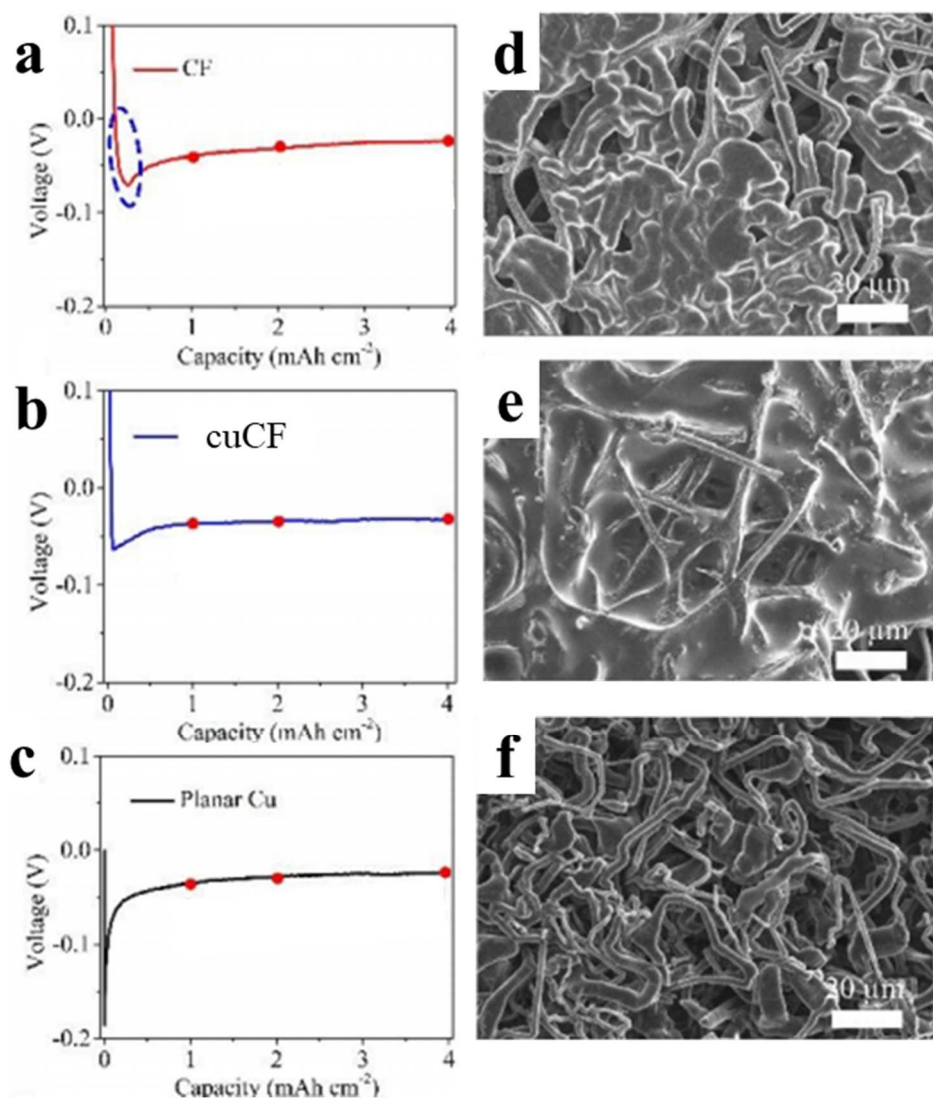


Figure 1. 3: (a-c) Nucleation overpotential and (d-f) corresponding SEM images after a plating capacity of 4 mAh cm⁻² [35].

1.3.2.2 Solid-state electrolyte

The replacement of flammable liquid electrolyte with solid-state electrolyte can substantially improve the safety, energy density, the lifespan, and enable the use of alkali metal anodes such as Na and Li [36]. The use of SSE which also functions as a separator suppresses the growth of Li dendrites addresses the issues of the shuttle effect of polysulfides in Li-S battery and degradation of electrodes in the Li-O₂ battery

technologies. Figures 1.4(a-d) show the schematic illustration of the Li-ion battery using flammable liquid electrolyte and lithium metal batteries using SSE. The use of SSE not only increases the gravimetric energy density but also increases the volumetric energy density. Despite many potential benefits of SSE, significant issues need to be addressed for its commercialization. The design of an ideal SSE should consider ionic conductivity, electro/chemical, and mechanical stability, ecofriendly and low cost. Figure 1.4(e) shows the various key factors that need to be investigated and considered while employing SSE in the battery. This includes the ideal property of SSE, state of art characterization tools, scalable and large production, and the recyclability of the battery materials. To date, different types of SSEs such as oxides, sulfides, Li-rich antiperovskites, thin-films, and polymers have been developed and investigated. As shown in radar plots in Figures 1.4(f-k), each kind of SSE has various advantages and limitations. Thus, scientists are trying to optimize or modify by material selection, material synthesis process to achieve higher performance, higher safety, and lower cost of SSE. The oxide-type (NASICON, LISICON, garnet, antiperovskite, and thin-film LiPON) SSEs are expensive for large scale production. The higher ionic conductive sulfide-based SSE, due to the polarizable nature of sulfur anion, has been explored as an alternative to the oxide-type SSEs (LiPON, garnets, LISICON, LTAP, etc.). But still, the sulfide-based SSE has chemical instabilities ($\text{Li}_7\text{P}_3\text{S}_{11}$) and contains an expensive germanium element ($\text{Li}_{10}\text{GeP}_2\text{S}_{12}$). Scientists are continuously working to improve the functionalities of SSE such as (1) superionic conductivity, (2) large bandgap to hinder electric conduction, (3) compatible with lithium metal anode, (4) excellent thermodynamic & electrochemical stability, and (5) low cost, lightweight and eco-friendly [36].

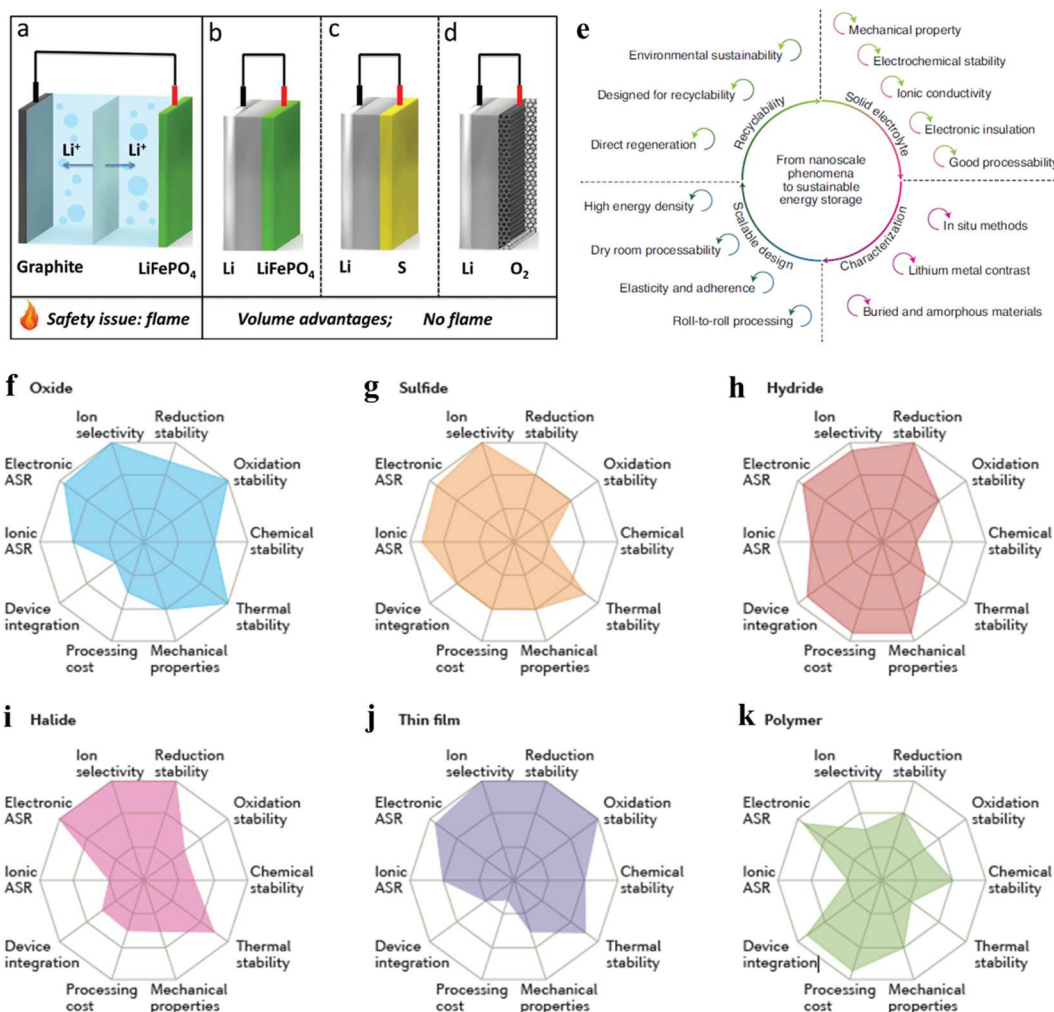


Figure 1. 4: (a-d) Schematic demonstration of Li-ion battery using liquid electrolyte and solid-state electrolyte [37], (e) Key challenges in solid-state battery[38], and (f-k) Radar plots showing the performance of different solid-state electrolyte [39].

1.3.2.3 Solid-electrolyte interphase

The development of an interface on top of lithium metal protects the lithium metal and inhibits the consumption of electrolyte. The development of such artificial solid electrolyte interphase (SEI) between solid lithium metal and liquid electrolyte greatly improves the electrochemical performance. The SEI can be developed in two ways, the in-situ

formation of SEI during battery operation and *ex-situ* formation of SEI before battery operation.

1.3.2.3.1 *In-situ* formation of SEI

In general, the most commercial LIBs and next-generation LMBs use a non-aqueous liquid electrolyte. The commonly used solvents for the electrolytes are ester-based and ether-based. The common Li salts for the electrolyte are bis(trifluoromethanesulfonyl)imide (LiTFSI), lithium hexafluorophosphate (LiPF₆), lithium bis(fluorosulfonyl)imide (LiFSI), and so on. The organic solvent usually gets reduced below 1.0 V (vs Li⁺/Li). The ether-based electrolyte system has shown the highest CE, lowest overpotential, and low reactivity with Li metal, but they have limited oxidative stability. In contrast, the carbonate-based electrolyte is suitable for higher voltage batteries, but they have poor compatibility with LMA. During the initial cycle, there is an immediate reaction between the hyperactive LMA and the electrolyte which results in the deposition of insoluble discharge products on the Li metal surface, known as SEI as shown in the schematic Figure 1.5(a). The formation of SEI originates from the non-faradic adsorption/desorption and the faradic electrochemical reaction process. An ideal SEI should possess several desired properties such as (1) high ionic conductivity (σ) to allow efficient Li-ion diffusion, (2) high mechanical strength to suppress the Li dendrite growth and chemical stability to inhibit side reactions, (3) reversibility to store Li by chemical-reaction/plating mechanism, (4) low electronic conductivity to prevent the flow of electron or inhibit the growth of Li, and (5) flexibility to accommodate the Li expansion during plating/stripping cycles as illustrated in Figure 1.5(b).

There are some different opinions regarding the SEI formation process and its mechanism. Figure 1.5c shows the schematic of the Peled model. This model discusses the primary surface reaction mechanism where the components of electrolyte get reduced [40]. The Li-ion migration through the polycrystalline materials containing SEI takes place by mobile point defects, which are called vacancy. Figure 1.5(d) shows the schematic for the Mosaic model. This model discusses that the insoluble multiphase reaction products during electrolyte reduction get deposited on the surface of negatively charged anode materials. Li-ion transport is possible through the mosaic surface[41]. The boundary between the interface of mosaic multiphase products allows for Li-ion migration. Thus, it is essential to consider the contribution of the grain boundaries into account. Figure 1.5(e) shows the schematic for coulombic interaction mechanism model. The positively charged and partially positively charged Li-ions aligned as head and foot, respectively[42]. The greater adhesion stimulated by the ion-pairs layer or unique double electric layer facilitates the stability of the SEI. Later, Thevenin and Muller suggested several other modified models such as the SEI model, compact stratified layer model, solid polymer layer model, and polymer electrolyte layer model also offer an intuitive understanding of the electrochemistry in the SEI [43, 44].

In the practical battery operation, the LMA is thermodynamically unstable (Gibbs energy -8.670 kJ/mol) in organic solvents/electrolytes, which leads to the *in-situ* decomposition of electrolyte and Li, forming an SEI layer. This SEI layer exhibits low Li-ion conductivity, moderate modulus, poor chemical stability, and does not fully passivate the LMA. In addition, the SEI layer cannot accommodate the large volume change of Li during plating/stripping cycles. The physical adhesion of *in-situ* formed SEI onto the

LMA is inadequate. Moreover, insufficient electrolyte affinity and low Li-ion conductivity lead to sluggish Li-ion transport. The repeated breakage and repair of the SEI layer consumes both Li and electrolyte, leading to the electrolyte dry-out and severe Li corrosion. Furthermore, the uncontrolled growth of sharp needle/whisker-shaped Li dendrites can pierce the separator concerning the safety issues. Thus, to improve the quality of *in-situ* based SEI, the use of additives and fillers in the electrolyte [45, 46], optimized concentration[47], dual salts[48], dual solvent [49], etc. have been proposed. However, the reduction of electrolyte components consumes superfluous amounts of electrolyte and Li while forming the SEI passivation during cycling [50]. Besides, the decomposition of Li and electrolyte components may not have deliberate control over the dimension and distribution of SEI-component, thickness, and spatial resistance. Scientists are still struggling to improve the contact between the Li electrode and the SEI layer to prevent the wear-off of the layers and lower the interfacial impedances. SEI without control of their composition, distribution, and thickness could detach from the bulk Li.

Recently, the engineering of *ex-situ* artificial SEI with the use of physical deposition or chemical deposition to modify the Li metal surface before the battery operation has attracted great attention in LMBs. *Ex-situ* derived SEIs are expected to solve the fragility and compositional uncontrollability of *in-situ* SEI. The uniform Li-ion flux provided by the uniformly coated *ex-situ* SEI and controllable interfacial resistance improved the quality of SEI. The *ex-situ* coating of polymer, carbon-based layer and an inorganic layer are the common selection to protect the LMA. Despite significant success and ease fabrication, there are still challenges such as low-Li ionic conductivity, low flexibility,

insufficient mechanical/chemical stability low adhesion, and peeling-off of the *ex-situ* based ASEI during cycling that need to be addressed.

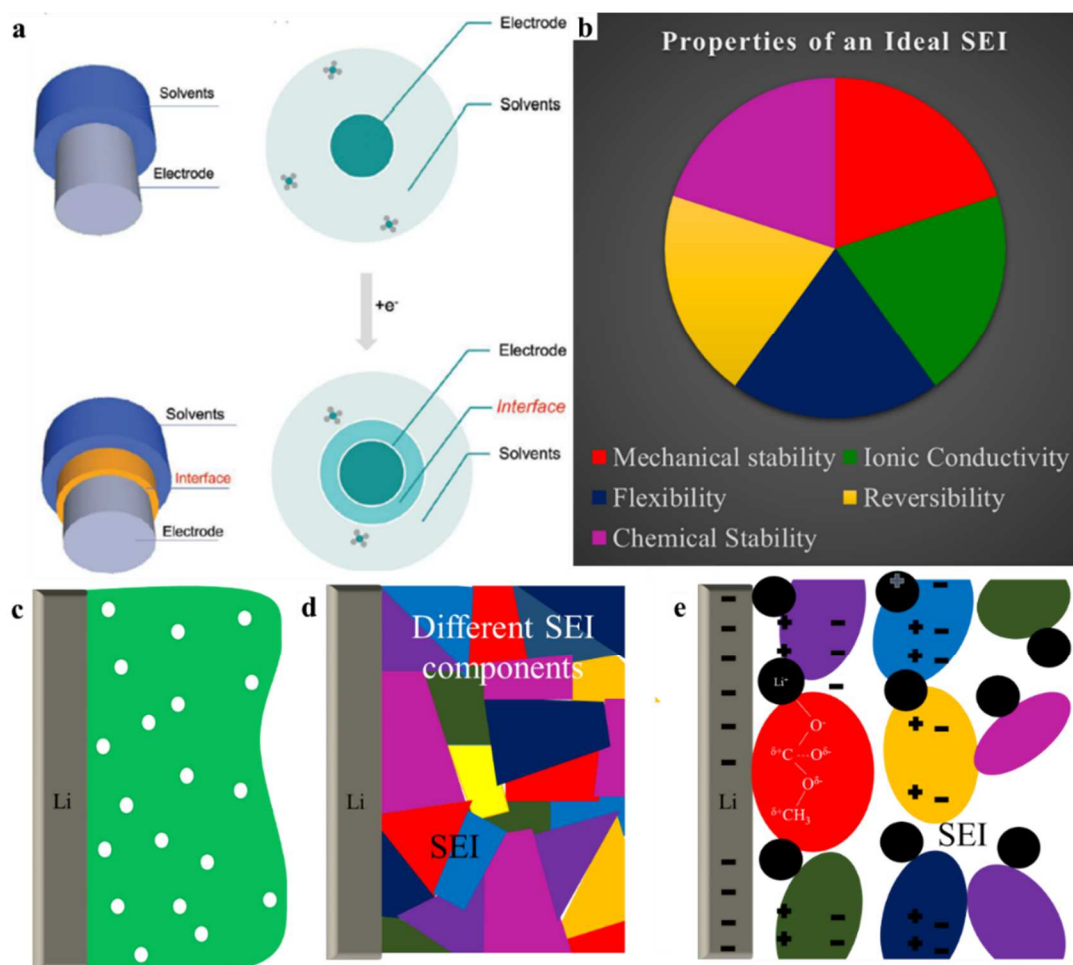


Figure 1. 5: (a) SEI formation due to the direct contact of the Li electrode and electrolyte during charge/discharge cycles [51], (b) schematic illustration of SEI properties in an ideal SEI and (c-e) the schematic of SEI mechanism in the Peled model, Mosaic model, and Coulombic interaction model, respectively [52].

1.3.2.3.2 *Ex-Situ* formation of SEI

The rough, crack surface, and non-uniform electronic conductivity distribution on lithium metal anode (LMA) lead to the non-uniform Li plating/stripping. The rough surface and cracks act as a hotspot or Li-ion accumulation center for initial Li nucleation. The growth

of Li dendrites in such hot spots gets amplified with the higher Li plating cycles. The *ex-situ* based ASEI via physical deposition or chemical deposition onto the LMA before battery operation is proven to smooth the LMA surface and uniformly distribute the Li-ion flux. The development of ASEI can be categorized into two types (1) The physical deposition technique, where the SEI-material is coated on the surface, and (2) chemical deposition, where the SEI-material undergoes a chemical reaction with LMA, forming new product as ASEI. Figure 1.6(a) shows the Li plating/stripping mechanism in modified Li by the physical deposition method (where the bilayer of graphite and SiO_2 was sputtered by the R-F sputtering technique). Figure 1.6(b) shows the Li plating/stripping mechanism in modified Li by the chemical deposition method (where the Li was pretreated with SnF_2 containing electrolyte by drop cast method to form LiF, Sn, and Li-Sn alloy as SEI components). Most of the previous studies are focused only on a single aspect of the SEI requirement such as high mechanical strength, high Li-ion conductivity, improving the interface stability or uniformity of ASEI. But, it is always challenging to choose the materials for SEI development and optimize all the parameters during SEI deposition which contributed to the stable and longer battery performance. The optimized thickness, high Li- ionic conductivity, high mechanical and chemical stability, and strong anchorage affinity towards the LMA is required for the design of an efficient ASEI. Besides, the selection of SEI-material with high flexibility, and reversibility which significantly improve battery performance will be discussed in this section.

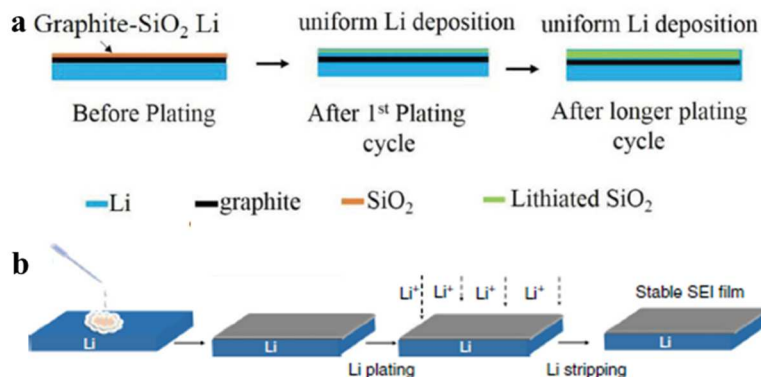


Figure 1. 6: Schematic illustrations of *ex-situ* artificial SEI on top of Li metal anode by (a) physical deposition [53] and (b) chemical deposition process [54].

1.3.2.3.2.1 Physical Deposition

The engineering of ASEI on the surface of LMA by the surface coating but without any surface chemical reaction is the physical deposition. Table 1.1 summarizes the materials & methods used for the ASEI development. The various methods of physical deposition include ultra-high vacuum deposition such as Radio-frequency (R-F) magnetron sputtering, Direct-Current (DC) sputtering, thermal evaporation, atomic layer deposition (ALD), pulsed laser deposition (PLD), chemical vapor deposition (CVD), and other solution-based processes such as drop cast, spin coat, and doctor blade.

Previous studies showed that various ceramics such as SiO₂, TiO₂, SnO₂, and Al₂O₃ are very promising interfacial layers to buffer the volumetric expansion of the anode [55-58]. Such ceramic layers can conduct Li⁺ and block electron transport [59]. Lithiated multiwall carbon nanotubes and multilayered graphene with high mechanical rigidity have been reported as a controlled Li diffusion interface [60, 61]. Besides, glass fibers, silica sandwiched between two separators, and SiO₂@PMMA nanosphere modified Cu electrode has also been studied [62-64]. These artificial layers improve wettability

towards electrolyte, reduce the concentration of Li ions, and react with growing Li to suppress the dendrites. Organic/inorganic dual layers were considered a better choice for stable SEI to suppress the volume expansion of Li anode [65, 66]. However, it is noted that those artificial layers without control on their composition and thickness could be worn away from Li anodes after continuous cycling due to the insufficient thickness and weak elasticity [11, 67]. Various mechanically stable but thick and unregulated protective layers were also reported [11, 68, 69]. However, these layers are required to be efficiently Li-ion diffusible and can control the flow of Li ions, which suppresses Li dendrite growth. Moreover, physical cracking in the interface layers can greatly induce inhomogeneous Li deposition leading to corrosion of Li, detrimental side reaction, and harsh Li dendrite growth [68-70]. Consequently, it is desired to have an effective interfacial layer that needs to address all these issues. Besides surface coating, the separate interfacial layer between the LMA and liquid electrolyte can also be used as an ASEI for protecting the LMA. Some of the interfacial layers include a monolayer of nanostructured and interconnected amorphous hollow carbon nanospheres [71], carbon paper interlayer [72], 3D conductive stainless steel fibrous metal felt [73], glass fiber cloth [62]. These interlayers are roll-pressed or solid-transfer on the surface of LMA.

Table 1. 1 Summary of the artificial SEI engineered by a surface coating method.

Material	Physical deposition method	Ref.
graphite/SiO ₂ , Li ₃ PO ₄ , carbon, Cu ₃ N, Al ₂ O ₃ , MoS ₂	R-F/-magnetron sputtering	[53, 74-78]
Al ₂ O ₃	ALD	[64, 79]
Double layer nanodiamond	MPCVD	[80]

Al ₂ O ₃ +PVDF-HFP, Cu ₃ N+SBR, ETPTA+DADMA-TFSI, perfluorinated ionomer	Doctor blade/drop cast/- UV irradiation/sol-gel	[81-86]
Hollow carbon nanosphere	mechanical press	[71, 87]
Li _{6.4} La ₃ Zr _{1.4} Ta _{0.6} O ₁₂ (LLZTO)	Heat-treatment	[88]
trifluoroethanol-modified Eggshell membrane (TESM)	interfacial layer	[89]
Metal chloride perovskite film	Spin coat-pressing	[90]

1.3.2.3.2.2 Chemical Deposition

The design of ASEI which can provide strong anchorage affinity with LMA facilitates the ultra-dense deposition of Li and fully shield the Li metal from the electrolyte is highly recommended. For engineering, the ASEI by the chemical deposition method, the surface chemical reaction treatment of LMA can be carried out between the LMA and the various organic/inorganic material dissolved in solution, and various gases. The chemical reaction between LMA and the solution can be done by immersing the Li into the solution or drop-cast, spin coat, doctor blade of the solution on Li metal. Similarly, the exposure of Li to direct gas flow or production of gases from solid chemical has been reported to allow the chemical reaction between those gases and the hyperactive Li metal. The complete reaction is allowed to happen with sufficient time, temperature, or any other required conditions, and then the SEI generated on Li is dried. Thus the composition and thickness of the ASEI depend upon the selection of the reactant-type, concentration, time, pressure, temperature, and other necessary parameters. Table 1.2 summarizes the method

used to generate different kinds of SEI components by different chemical deposition method.

Improving the modulus properties and ionic conductivity of the interphase by various strategies have been reported [80, 91]. The poor Li contact between these interfacial layers and bulk Li could lead to an increase in both interfacial and overall cell resistance. The low wettability of interphase towards non-aqueous electrolyte also leads to sluggish Li-ion transport. Differing from surface engineering of the artificial interphase layer, the use of various electrolyte additives [92, 93] provides an alternative pathway, where a more intimate contact could be ensured.

Table 1. 2 Summary of the artificial SEI engineered by surface chemistry method.

SEI components	Chemical deposition method	Ref.
Li-O-Si linkage	solution-based treatment	[94]
Li ₃ PO ₄	solution-based treatment	[69]
organic/inorganic	solution-based treatment	[95]
Li & metal alloy/Li-halides	solution-based treatment	[54, 96-98]
Ge, GeO _x , Li ₂ CO ₃ , LiOH, & LiCl,	solution-based treatment	[99]
MIEC LLTO	solution-based treatment	[100]
[LiNBH] _n chains	solution-based treatment	[101]
Li ₂ S/Li ₂ Se	gas-based treatment	[102, 103]

LiF layer	gas-based treatment	[104]
LiF coating	gas-based treatment	[105]
LiF thin film	gas-based treatment	[106]
Li ₃ N	gas-based treatment	[107]

Recently, fluorinating SEI with LiF as a key component has been widely adopted to improve the cycling performance of Li metal anode based on two hypotheses: (1) LiF is an excellent electronic insulator whose wide gap effectively prevents electron tunneling [108]; (2) When interfacing with other ingredients at nano-scale, LiF could provide high ionic conductivity, low diffusing energy, and high surface energy, which not only allows sufficiently fast Li-ion kinetics but more importantly promotes the electrodeposition of Li in a parallel rather than vertical manner [98, 109]. Consequently, LiF-based interphase ensures better surface morphology and serves as a robust barrier to Li dendrite growth [49, 98, 105, 109-113]. Besides LiF, lithium-based alloys have also been studied as protective interphase to suppress Li dendritic growth, because the Sn-Li alloy phase could reduce the Li-ion diffusion barrier, and lead to improved Li metal interphase stability [96, 114, 115]. Such alloy approaches include the *in-situ* formation of Sn-Li, Li₁₃-In₃, Li-Zn, Li₃-Bi, Li₃-As, Au-Li, Si-Li, etc [114, 116]. However, the development of an artificial SEI is still at its early stages. The mechanical and electrochemical instability of interphase leads to persistent deterioration. Low Li-ion conductivity, chemical instability, morphological inhomogeneity, and the subsequent uneven growth of natural SEI remain to be unresolved. In particular, there has never been synergy established between inert but protective LiF, the electrochemically active Sn and Sn-Li alloy on the SEI.

1.4 Motivation

The material modification of WO_3 -TMO as anode for improving the Li-ion battery performance and development of *ex-situ* SEI with sufficient Li-ion conductivity, high adhesion, or anchorage affinity with Li metal surface, high mechanical and chemical stability for reviving the Li metal anode.

1.5 Objective

The objective of this work is to reduce the WO_3 -TMO and develop the *ex-situ* based (physical or chemical deposition) solid electrolyte interphase to stabilize the Li metal anode for achieving outstanding electrochemical battery performance. The following tasks were performed to achieve the goal.

1. A novel technique to reduce WO_3 by incorporating urea into WO_3 followed by annealing at a high temperature of 500 °C under nitrogen.
2. A novel technique to develop the *ex-situ* artificial SEI by
 - a. R-F sputtering an ultrathin film of the graphite- SiO_2 bilayer on Li metal (physical deposition method).
 - b. Drop-casting SnF_2 containing electrolyte on Li metal surface to create an artificial SEI composed of LiF, Sn, and Sn-Li alloy (chemical deposition method).
3. Optimize the experimental condition for developing the *ex-situ* artificial SEI including the thickness deposition and/or the concentration of the SnF_2 .
4. Perform the structural and morphological characterization using X-ray diffraction, Raman spectroscopy, and field emission scanning electron microscopy/ energy dispersive spectroscopy (FESEM/EDS).

5. Perform the electrochemical characterization using cyclic voltammetry (CV), electrochemical impedance spectroscopy (EIS), symmetrical cell test, and full cell test.

1.6 Organization of the Dissertation

Chapter 1 describes the importance of energy sources and energy storage devices. A variety of techniques to improve the battery performance of TMOs anode material for Li-ion battery application. A comprehensive review of the strategies to address the issue of Li metal anode. The advantages and limitations of the various efforts that have been done to solve the issues of Li dendrite growth and unstable SEI in Lithium metal batteries were presented. Further, the details on the SEI engineering process and the electrochemical performance of previously reported *ex-situ* based physical and chemical deposition techniques have been discussed. Finally, the motivation, objective and organization of the work have been presented.

Chapter 2 discusses the details of the lithium-ion battery and beyond with its working principle. Besides, the important parameters that are required to evaluate the battery performance are listed and described briefly. Moreover, the variety of material and electrochemical characterization tools are briefly described.

Chapter 3 discusses details of experimental procedures for the modification of commercial WO_3 , development of *ex-situ* artificial SEI by physical and chemical deposition techniques. Besides, it discusses the materials and electrochemical characterizations carried out to study the properties of WO_3 anode material and artificial SEI based on the stability and battery cycling performance.

Chapter 4 includes the results and discussions of the structural and electrochemical characterization of WO_3 anode materials and the developed *ex-situ* artificial SEI. The electrochemical characterization and optimization of the experimental conditions are discussed. All the material's property and electrochemical test results are analyzed.

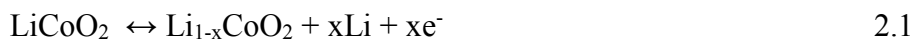
Chapter 5 is a summary of all three works (self-recovery of capacity using reduced WO_3 anode material, development of artificial SEI by physical and chemical deposition techniques) with specific conclusions and future work.

CHAPTER 2: THEORY

2.1 Components and working principle of Li-ion batteries

Each battery consists of a positive and negative electrode divided by a separator soaked in with an electrolyte solution containing dissociated Li salts. The negative and positive battery electrodes are composite structures made up of a mixture of active material particles, a polymeric binder, and a conductive additive. The porous electrode wets the surface with electrolyte for Li-ion transport and the conductive additive transports electron. Metallic current collector such as Cu and Al are used to make good electrical contact between the electrodes. The porous separator which is an electrically insulating but ionically conducting layer physically separates the two electrodes from short-circuit. When the battery is charging, the cathode gives up its lithium ions to the anode. The battery stores energy during this charging process. When the battery is discharging, the lithium ions from the anode move back across the electrolyte to the cathode, producing the energy that powers the battery. In both cases, electrons flow in the opposite direction to the ions around the external circuit. The reaction occurs in each electrode during the charge/discharge process. The driving force that causes a reaction is the difference in the chemical potential of Li between the two electrodes. The reaction mechanisms are shown in the equations below:

At cathode,



At anode,



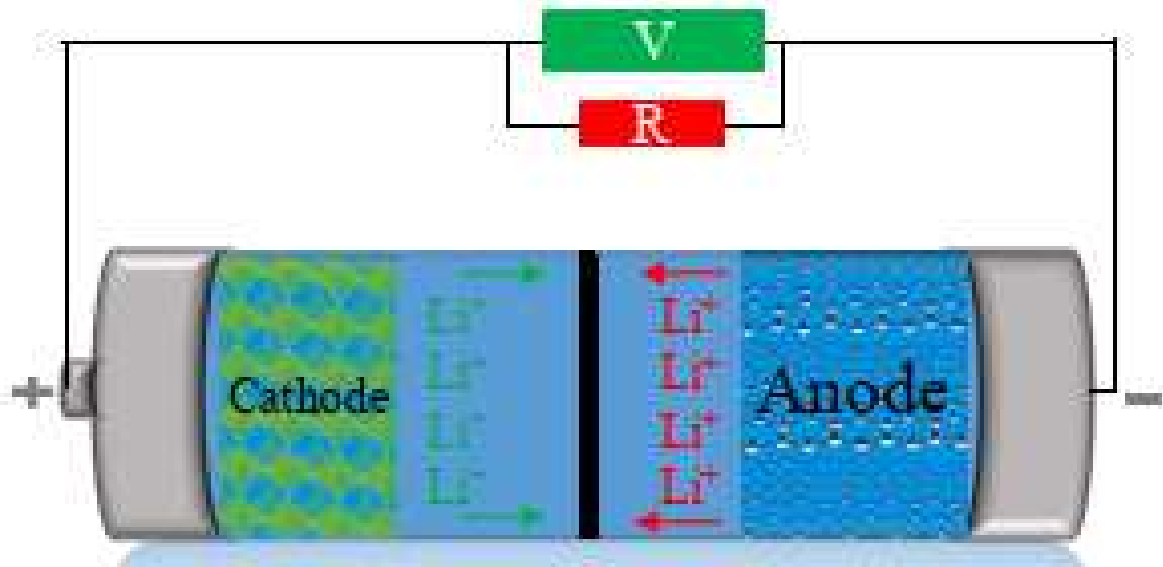


Figure 2. 1: Schematic illustration of the working mechanism in Li-ion battery.

2.2 Important parameters for evaluating battery performance

Before going into the details of the Li-ion batteries and beyond, it is beneficial to first explain some of the commonly used terms in this work. Particularly, for the investigation, evaluation, and comparison of the battery cycling performance of the electrode materials, it is important to understand the specific capacity, coulombic efficiency (CE), cycle life, voltage, energy density, and power density.

2.2.1 Specific capacity

The charge stored by applying certain current (I) for a particular time (t) is the capacity (Q). The amount of charge that can be stored per unit mass of the electrode materials is called a specific capacity (SC).

$$Q = I \cdot t \quad 2.3$$

$$SC = (F \cdot z) / (M \cdot 3.6) \quad 2.4$$

Where, F is the Faraday's constant, z is the amount of charge transfer per mole, M is the molar mass of the active material.

2.2.2 Coulombic efficiency and Cycle life

Coulombic efficiency (CE) is defined as the ratio of the discharge capacity to the charge capacity. It indicates how much capacity is lost in the cycle. If the CE is 100%, that means the capacity is reversible. The loss of CE or CE less than 100 % can be attributed to the side reactions between the anode/cathode and the electrolyte. This is one of the important parameters which determines the battery capacity with cycle number. A 0.1% CE loss leads to a 10% capacity loss over 100 cycles.

2.2.3 Voltage

The potential difference or difference in chemical potential between the anode and cathode electrode gives the voltage of the battery. The reference voltage value used in Li-battery literature is the electrochemical potential of Li^+/Li .

The chemical potential of Li in electrode is defined as

$$\mu_{\text{Li}} = \mu_{\text{Li}}^{\circ} + RT \ln a_{\text{Li}} \quad 2.5$$

$$\text{Voltage of the cell (V)} = -\Delta G/nF \quad 2.6$$

Where, μ_{Li}° = chemical potential of the Li in its standard state, R = universal gas constant, T = absolute temperature and a_{Li} = activity of Li. Similarly, ΔG = Gibbs free energy of the reaction, n = no. of moles of electrons consumed in the electrochemical reaction.

2.2.4 Energy density

The integration of the voltage range and the specific capacity is called the specific energy or gravimetric energy density (Wh kg^{-1}).

$$\text{Energy density} = \int V \cdot dSC \quad 2.7$$

If a battery has a high energy density, then it implies that it can store a large amount of energy in a small amount of mass.

2.2.5 Power density

The power density is calculated by multiplying the current density applied for charge/discharge by the voltage of the cell. If the battery has high power density, then it can deliver a large amount of energy in a short time based on its mass.

2.3 Material characterizations

2.3.1 X-ray diffraction Spectrum (XRD)

X-ray diffraction (XRD) spectra are used to examine the structural property of the material. When X-rays are incident on the crystallographic plane of the materials, it gets diffracted according to the arrangement of atoms. The incident X-rays are diffracted back which undergoes constructive interference to produce increased intensity based on the spacing between atomic layers. X-ray source, sample holder, goniometer, and detector are the main components of X-ray diffractometer. Bragg's law explains the interference pattern scattered by the crystals as given below.

$$2d\sin\theta = n\lambda \quad 2.8$$

Where $2d\sin\theta$ is the path difference between the scattered ray and incident ray, d is the interplanar spacing between the crystal planes, n is an integer and λ is the wavelength of X-ray.

2.3.2 Field emission scanning electron microscopy (FESEM)

FESEM is a microscope that works with the emission of electrons liberated by a field emission source and accelerated by a high electric field gradient. Inside the high vacuum

column, the primary electrons are focused and deflected by electronic lenses to produce a narrow scan beam. The surface to be imaged is scanned by the beam of electrons in a zig-zag pattern. These narrow beams bombard the surface of the sample, resulting in secondary electrons. The detector collects the secondary electrons and displays the electronic signal, which is amplified and transformed into a video scan-image.

2.3.3 Energy dispersive spectroscopy (EDS)

Energy dispersive spectroscopy (EDS) or (EDX) is a chemical microanalysis tool used in combination with SEM or FESEM. The elemental composition of the sample can be recorded with the help of EDS. When the sample is bombarded with the electron beam, the electrons are ejected out from the atoms of the sample. The created vacancies are filled by electrons from a higher state. To balance the energy difference between the ejected electrons and bombarded electrons, x-rays are emitted. These x-rays carry the properties of the elements in the sample. The atomic% or wt% of the elements can be calculated in the specific area. Besides, the elements present in the sample can be mapped into different colors.

2.3.4 Braunauer Emmett and Teller measurement

Braunauer Emmett Teller (BET) measurement provides the information on the physical adsorption of gas molecules on the solid surface and helps to calculate the specific surface area (SSA) of the solid materials, usually in $\text{m}^2 \text{g}^{-1}$ unit. The specific surface area can also be expressed in terms of area per unit volume ($\text{m}^2 \text{cm}^{-3}$), which can be calculated by multiplying the BET SSA with the density of the sample. Thus, the inert gases (such as nitrogen, krypton, and argon) which do not react with the solid materials are used to quantify the SSA. BET theory is based on or can be derived from the Langmuir theory,

which assumes the adsorption of the monolayer to multilayer. The samples are degassed before BET measurement to remove the physical impurities from the surface of the solid materials. This can be done at elevated temperatures in conjunction with a high vacuum or continuous flow of argon gas. The BET analysis is carried out in the linear region of the BET plot and efficiently evaluated with the help of Rouquerol transform. BET analysis can be carried out based on the single point and multi-point BET.

2.3.5 X-ray photoelectron spectroscopy

X-ray photoelectron spectroscopy (XPS) is considered as an indispensable tool which can provide the chemical composition and quantitative information in any bulky materials, thin-film, or interphase. The average depth analysis that XPS can do is ~ 5 nm. In XPS, a sample is excited with mono-energetic Al $K\alpha$ x-rays which causes the emission of photoelectrons. The electron energy analyzer measures the energy of the emitted photoelectrons. The intensity and binding energy (BE) of the emitted photoelectron peak provide the detailed chemical state, elemental, and quantitative information of the sample. The shift in the binding energy of a core electron of an element signifies the change in the chemical bonding of that element. Besides, XPS provides information on the atomic composition, chemical state, electronic structure, and band structure. The information from the *ex-situ* or *in-situ* XPS analysis of the battery materials or components before charging/discharging, after charging, and after charging/discharging can be collected. From such information, we can identify, quantify, and reflect the chemical distribution of elements. Besides, the shift in the binding energy of a core electron indicates the occurrence of lithiation/delithiation reaction responsible for storing charges. The information on the reversibility of the reaction can be obtained based on the recovery of the shifted peak. The

information on the electrochemistry of the battery components such as anode or cathode help to understand the shortcomings involved, which eventually help to improve the specific capacity and energy density. Moreover, understanding the mechanism of SEI is very complicated without XPS.

2.3.6 Raman Spectroscopy

Raman spectroscopy is a non-destructive chemical analysis characterization tool which is useful to obtain the vibrational, rotational, and other low-frequency modes of the systems. The interaction of light and the chemical bond within the material or system provides detailed information on the chemical structure, polymorph, crystallinity, molecular interaction, and phase of the system. Raman spectroscopy is a light scattering tool, where the molecules of the sample scatter the incident light from a laser light source with high intensity. The wavelength of the scattered beams which are different from those of the incident beam is called Raman scatter or inelastic scatter and provides the information of the material/system. Although X-rays can be used, in general, monochromatic light from a laser in the visible, near-infrared, or ultraviolet range is used. The different peaks at different Raman shift wavelength position and with different intensity corresponds to a particular molecular bond vibration such as C-C, C=C, C-H, and N-O. Raman spectroscopy can be both qualitative and quantitative. Raman spectroscopy can also be used for microscopic materials with a spatial resolution in the range of 0.5- 1 μm . Raman can measure different samples such as solids, powders gels, slurries, and gases.

2.3.7 Fourier transform infrared spectroscopy

Fourier transform infrared is the selected characterization technique for infrared spectroscopy. When the infrared radiation is allowed to fall on the sample, some of the radiations are absorbed by the samples and some of them are transmitted or emitted. The FTIR spectrometer collects high spectral resolution data over a broad range. The absorption of the infrared radiation by the sample at a certain wavelength is measured by FTIR, which is the characteristics of the molecular structure in a sample. During the absorption, the infrared radiation excites the molecules of the sample to a higher vibrational state. The difference between the energy at rest and after excitation will be absorbed by the particular molecule in a sample. In general, the intensity versus wavenumber is plotted for the results from FTIR. The reciprocal of wavelength is called wavenumber (cm^{-1}). The intensity represents the percentage of light transmitted or absorbed at each wavelength or wavenumber.

2.4 Electrochemical characterizations

2.4.1 Cyclic voltammetry

Cyclic voltammetry (CV) measurements are carried out using potentiostat which can source as both current and voltage. The potential of the working electrode is ramped linearly with time at a certain scanning rate. CV has been widely adopted to investigate the redox behavior of electrochemical reactions, such as the identification of chemical species, chemical reaction rates, and electron transfer properties. The potential between the working electrode and the counter electrode is ramped linearly from a negative to a positive potential (forward scan) and vice versa (reverse scan) with the help of potentiostat. The

scanning can be done multiple or single time where the resulting current versus voltage between the working and counter electrode is plotted.

2.4.2 Electrochemical impedance spectroscopy

Electrochemical impedance spectroscopy (EIS) is an important characterization tool for understanding electrochemical reactions and charge transfer dynamics. The response of the electrochemical by the application of electric potential is recorded. EIS has been widely used in many applications such as energy storage devices, photovoltaic devices, and other electrochemical devices. The alternating current (AC) voltage is applied across the electrodes and the function of frequency is noted to understand the internal non-linear electrochemical dynamics. EIS results can be interpreted as a Nyquist plot. In the Nyquist plot, the Z-real axis corresponds to the ohmic/ series resistance (R_s) which is the bulk resistance. The semicircle in the lower frequency range determines charge transfer resistance (R_{ct}) between the two interfaces, and the constant phase element (CPE) represents the electric double layer capacitance between the interfaces [117, 118]. The inclined line in the lower frequency region is called Warburg impedance (W) which represents the diffusion of charge. The Randles equivalent circuit can be used to fit the EIS results.

2.4.3 Symmetrical cell test

The electrochemical test using the same material as the positive and negative electrode (for example, the symmetrical cell with Li/Li as electrodes on both sides) is called a symmetrical cell test. The symmetrical cell can be done to understand the electrochemical Li plating/stripping cycles. To understand the Li plating mechanism, the identical Li electrode can be used on both sides of the cell. The plating/stripping can be done at various

current densities to achieve various capacities to understand the Li deposition behavior and long-term voltage versus time profile. Although the cell has zero voltage Vs Li^+/Li and is not useful for practical applications, it provides a lot of information about the reactions between the electrode materials and electrolyte, comparison between the control symmetrical cell, and any modifications are done on any components of the cell.

2.4.4 Half-cell or Full cell test

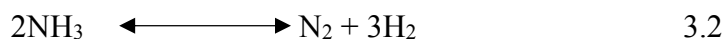
The cell with a different positive and negative electrode, showing the voltage difference is called half-cell or full cell. The cell which uses anode other than lithium (such as graphite and tungsten trioxide) and any cathodes such as lithium cobalt oxide (LCO) and lithium nickel manganese oxide (NMC) are regarded as full cell and the cell with lithium as anode and any other electrode materials are called half-cell. The term half-cell is also called a full cell in lithium metal batteries.

CHAPTER 3: EXPERIMENTAL PROCEDURES

3.1 Materials and preparation

For project 1, where the self-recovery of capacity was observed by reducing WO₃ anode material for LIBs, the slurry was made by mixing 1g tungsten(VI) trioxide WO₃ (typically 99.9% pure), 1ml alpha-terpineol (Sigma-Aldrich), and 0.1g Urea 99% (Acros Organics) using a mortar and pestle. The slurry was annealed inside a tube-furnace under nitrogen flow at 500°C for 2 h. As a result, pristine WO₃ is designated as P-WO₃ was reduced to obtain reduced WO₃ (R-WO₃).

At Urea decomposes to ammonia at temperature ~ 180 °C, the urea was decomposed to ammonia, which was further decomposed to N₂ gas and reactive H₂ at higher temperatures (> 400 °C). Thus, P-WO₃ was reduced to R-WO₃ due to the available N₂ gas and reactive H₂, creating oxygen vacancies as follows [119-124].



3.1.1 Anode electrode fabrication for LIBs

Active materials, P-WO₃ and R-WO₃ powders were individually mixed with conductive super-P carbon black and binder polyvinylidene fluoride (PVDF) at a weight ratio of 8:1:1, respectively. N-Methyl-2-pyrrolidone (NMP) was used as a solvent to form two slurries using a magnetic stirrer, and the mortar & pestle. The doctor blading method was applied to obtain film out of each slurry by coating each slurry on a copper foil current collector separately. The coated electrodes were then dried overnight in a vacuum oven at 100°C to remove the solvent and other impurities. The dried electrodes were cut into circular disks

with a diameter of 12.7 mm using an electrode cutter and were used as the working anode electrode. For each electrode, P- WO_3 and R- WO_3 , the average mass loading of the electrode was $\sim 2.5 \text{ mg cm}^{-2}$ and the average areal mass loading of active material WO_3 was $\sim 2.0 \text{ mg cm}^{-2}$.

3.2 Development of solid-electrolyte-interphase

The development of SEI was done by *ex-situ* physical and chemical deposition methods as described below.

3.2.1 Physical deposition

3.2.1.1 Materials and Preparations

For project 2, the Li-metal chips with diameter size 15.6 mm and thickness 450 μm were purchased from MTI corp, USA. The sputtering targets, graphite, and silicon dioxide (SiO_2) with a diameter size 2.0-inch were purchased from Kurt J. Lesker. Before radio-frequency (R-F) sputtering or battery assembling, the surface of as obtained Li chips were cleaned. The sharp razor blades were used to polish the surface until the shiny Li surface was obtained. This helps to remove the oxide layer and other impurities from the surface of Li metal. The closed container was used to transfer the Li samples from the Ar-glove box to the sputtering system, SEM, or XPS system to avoid exposure to air and moisture. The Li metal anode chips were protected using Kapton tape while doing XRD measurement. In the R-F sputtering system (Torr combination), the distance between Li chip samples on the top side and target on the bottom side was $\sim 15 \text{ cm}$. The thickness deposition rate was $\sim 0.1 \text{ \AA/sec}$ using Ar as a carrier gas at a constant flow of 20 sccm. Figure 3.1(a,b) shows a schematic illustration of the Li deposition behavior on bare Li and graphite- SiO_2 bilayer modified Li metal anode, respectively. The different thicknesses of

an individual thin film of graphite and SiO₂ ranging from 10 – 30 nm were deposited to optimize the thickness and then again the bilayer, graphite (bottom layer), and SiO₂ (top layer), were sputtered on Li, which was designated as graphite-SiO₂ Li. The bilayer thin film deposited Li chips were cut into 13mm circular discs to use as anode material.

3.2.1.2 Cathode electrode fabrication for LMBs

Lithium titanate (LTO) as an active material powder, super-P carbon black as a conductive additive, and polyvinylidene fluoride (PVDF) as a binder were mixed at a weight ratio of 8:1:1 using NMP as a solvent. The slurry was obtained using a magnetic stirrer and mortar and pestle. The slurry was coated on a copper foil current collector by doctor blading and then dried overnight (~12 h) in a vacuum oven at 100°C. The dried samples were cut into circular disks with a diameter of 12 mm and used as the working electrode. The average total areal mass loading of the electrode was ~2.5 mg cm⁻² and the average areal mass loading of active material LTO was ~2.0 mg cm⁻². The cathode electrode, lithium nickel cobalt manganese oxide (LiNi_{1/3}Co_{1/3}Mn_{1/3}O₂) or (NMC111) was used as received from the US Army Research Lab. The areal mass loading of the cathode electrode was 11.88 mg cm⁻² and the areal mass of active material (NMC11) was 9.98 mg cm⁻². The electrodes were cut into circular disks with a diameter of 12 mm.

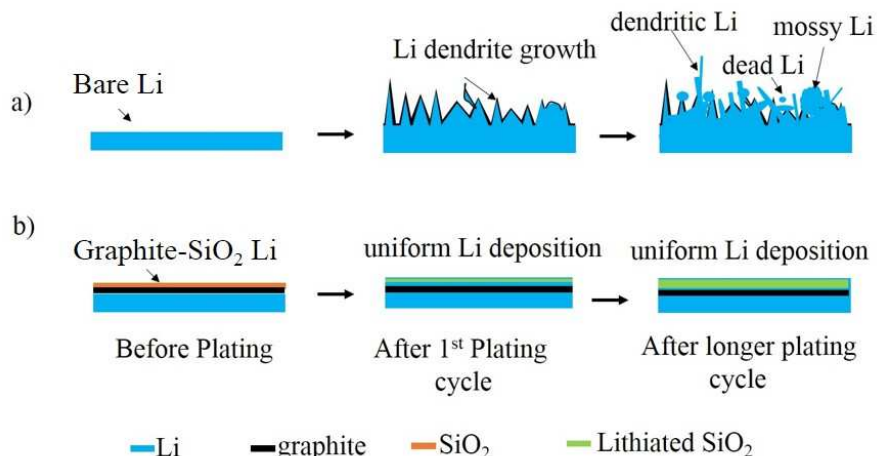


Figure 3. 1: Schematic demonstration of Li deposition behavior: a) on bare Li anode, and b) on graphite-SiO₂ bilayer sputtered Li metal anode [53].

3.2.2 Chemical deposition

3.2.2.1 Materials and preparations

For project 3, the Li-metal chips with diameter size 15.6 mm and thickness 250 μm were purchased from Xiamen Tmax, China. Tin (II) fluoride was purchased from Acros Organics, USA. Before the chemical pretreatment of Li metal anode, the surface of as obtained Li chips were cleaned. The sharp razor blades were used to polish the surface until the shiny Li surface was obtained. This helps to remove the oxide layer and other impurities from the surface of Li metal. The closed container was used to transfer the Li samples from the Ar-glove box to FESEM, or XPS system to avoid exposure to air and moisture. The Li metal anode chips were protected using Kapton tape while doing XRD measurement. The different wt% (1, 3, 5 wt%) of SnF₂ partially dissolved in 1M LiPF₆ in a mixture solvent of ethylene carbonate (EC)/diethylcarbonate (DEC) (1:1 v/v) was ultrasonicated before drop-casting on the Li metal surface. The amount of electrolyte-containing different concentrations of SnF₂ used for drop casting was 30 μL . The surface of Li metal

immediately changed from the silver shiny color to dark gray after drop-casting SnF_2 containing electrolyte. A replacement reaction between Li metal and SnF_2 occurs which allows the formation of LiF, Sn, and Li-Sn alloy [111, 114].



The Li metal chips with drop cast (SnF_2 +electrolyte) electrolyte were allowed to dry inside the Ar-glove box for ~ 48 hrs at 60 °C. The surface of Li chips becomes whitish color after 48 hrs and the electrodes were continuously rinsed 2-3 times with dimethyl carbonate (DMC) solvent to remove any undissolved residues. The bare Li and the Li treated with SnF_2 chips were cut into a circular disc with a diameter size of 12 mm.

3.2.2.2 Cathode electrode fabrications for LMBs

The cathode electrode, lithium nickel cobalt manganese oxide ($\text{LiNi}_{1/3}\text{Co}_{1/3}\text{Mn}_{1/3}\text{O}_2$) or (NMC111) was used as received from the US Army Research Lab. The areal mass loading of the cathode electrode was 11.88 mg cm^{-2} and the areal mass of active material (NMC11) was 9.98 mg cm^{-2} . The electrodes were cut into circular disks with a diameter of 12 mm. Figure 3.2(a) shows the schematic illustration of dendritic Li growth and formation of mossy and dead Li after plating/stripping cycles using bare Li anode. Figure 3.2(b) shows the schematic illustration of the fabrication process of Li pretreatment using the drop cast method. It also shows the modified Li with *ex-situ* developed fluorinated hybrid solid-electrolyte-interphase results in dendrite-free, smooth, and uniform Li deposition.

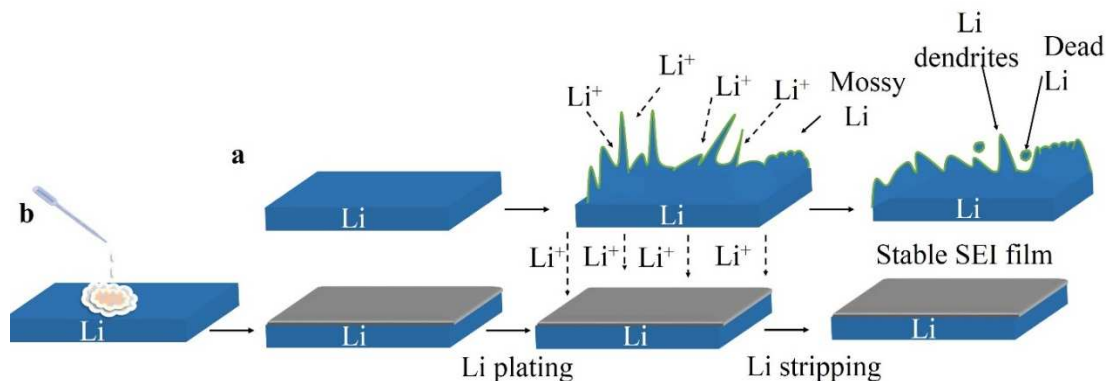


Figure 3. 2: Schematic illustrations of Li dendrites' growth on (a) bare Li and (b) smooth Li deposition on artificial SEI protected Li [54].

3.3 Material characterizations

3.3.1 X-ray diffractometer

The crystal structure and crystallite size measurements of P-WO₃ and R-WO₃ samples were conducted on a Rigaku SmartLab X-ray diffractometer (XRD) with Cu-K α radiation ($\lambda=1.54178$ Angstrom). The XRD of bare Li metal, ultrathin bilayer modified and SnF₂ pretreated Li metal was conducted using the same XRD instrument, encapsulating the samples with Kapton tape during XRD measurement to avoid moisture contamination. The samples were scanned in the suitable 2-theta degree range depending upon the samples. The X-ray is generated when the applied tube voltage and current reached 40 kV and 44 mA. Figure 3.3 shows the picture of available XRD set up in the Lab at SDSU.



Figure 3. 3: Picture showing the X-ray diffractometer located in the Lab at SDSU.

3.3.2 Field emission/-scanning electron microscopy and energy dispersive spectroscopy

Scanning electron microscopy (SEM) and energy-dispersive X-ray spectroscopy (EDS) characterization were carried out using a Hitachi S-4300 N SEM. SEM images, EDS, and elemental mapping were performed using Hitachi S-3400N SEM and Hitachi S-4700N FESEM. The surface topography and the cross-sectional SEM images were measured. The sensitive samples such as Li and modified Li were taken from the glove box to the SEM chamber in a closed vial. While using Hitachi S-4300 N SEM, the semiconducting samples were gold-sputtered with the help of CRC-sputtering. The various accelerating voltage was applied to scan the high resolution and low-resolution SEM images depending upon the type of samples. The Aztec software (Oxford Instruments) was used to record the elemental

mapping and EDS spectrum. The atomic/weight percentage and the elemental distribution can be investigated using SEM. Figure 3.4 shows the picture of Hitachi S-3400N SEM and Hitachi S-4700N FESEM available in the cleanroom of SDSU.

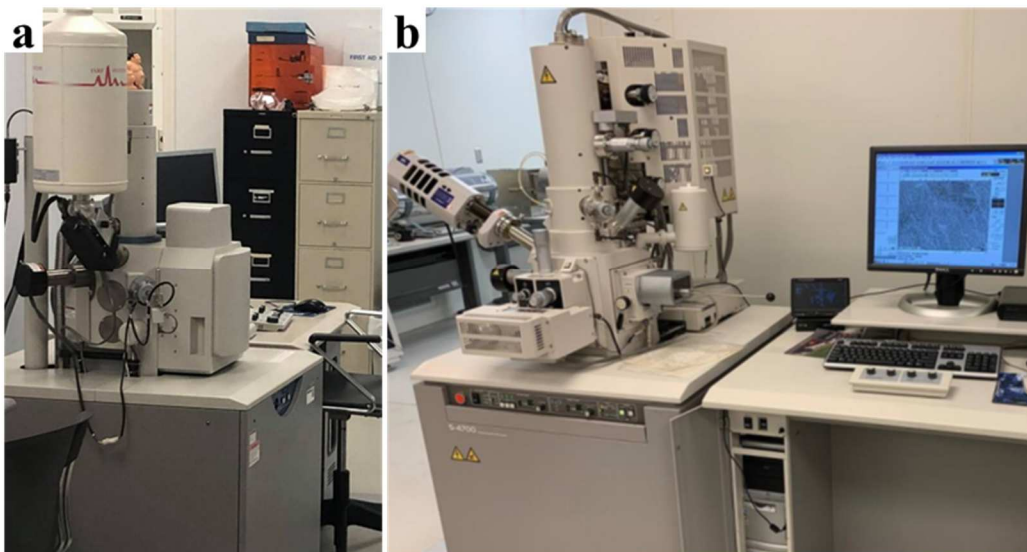


Figure 3. 4: Picture of a Hitachi S-3400N SEM EM and b Hitachi S-4700N FESEM located in the cleanroom at SDSU.

3.3.3 Atomic force microscopy

The topography of thin films was measured using an Agilent SPM 5500 atomic force microscope (AFM) equipped with MAC III controller using a tip with a resonance frequency of 75 kHz as shown in Figure 3.5. The average particle size was measured. To investigate the surface morphology and Young's modulus measurement of bare Li and SnF₂ treated Li was carried out using atomic force microscopy (AFM) equipped with the MAC III controller using RTESPA-525 tip with a resonant frequency of 75 kHz through quantitative nano-mechanical (QNM) mode.

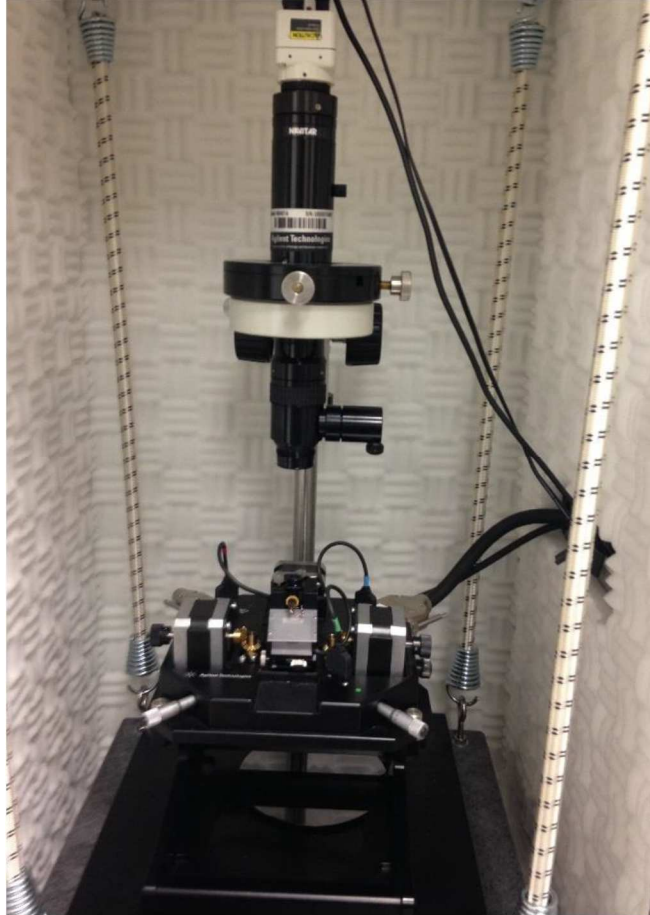


Figure 3. 5: Picture of AFM located in DEH 053 at SDSU.

3.3.4 Raman spectroscopy

Raman spectroscopy was carried out using the Horiba Raman system with a 532 nm laser. The characteristic peaks (D-band and G-band) of the graphite and the ratio of their intensities were studied. Figure 3.6 shows the experimental setup for the Horiba Raman system in the Lab at South Dakota State University (SDSU).



Figure 3. 6: Experimental setup for the Horiba Raman system in the Lab at SDSU.

3.3.5 UV-visible spectrum spectroscopy

The absorption characterization was performed using Agilent 8453 UV-vis spectrophotometer. For this, 0.1g of each P-WO₃ and R-WO₃ powder were dissolved separately in an aqueous solution of nitric acid with a 1:1 volume ratio. Tauc's plots were obtained using Tauc's equation $\alpha h\nu = A(h\nu - E_g)^n$, where A is constant, $h\nu$ is photon energy, E_g is bandgap, α is absorption coefficient and n (1/2 for WO₃) is the exponent coefficient which denotes the nature of electron transition from the valence to the conduction band.

3.3.6 X-ray photoelectron spectroscopy

X-ray Photoelectron Spectrum (XPS) was performed on the Thermo Scientific X-ray Photoelectron Spectrometer with Al Ka radiation. X-ray Photoelectron Spectrum (XPS) was performed on the Thermo Scientific X-ray Photoelectron Spectrometer with Al Ka radiation. The XPS experiment was performed in part in the Nebraska Nanoscale Facility: National Nanotechnology Coordinated Infrastructure and the Nebraska Center for Materials and Nanoscience, which are supported by the National Science Foundation under Award ECCS: 1542182, and the Nebraska Research Initiative.

3.3.7 Brunauer Emmett and Teller

Isotherm adsorption analysis with N_2 was carried out using an ASAP 2020 Micropore Analyzer at 77 K (liquid nitrogen bath). Brunauer-Emmett-Teller (BET) equation was used to calculate the specific surface areas. The BET experiment was performed in the department of agricultural and biosystems engineering at SDSU.

3.4 Electrochemical characterizations

The coin type CR-2032 Li-ion cell was fabricated using lithium metal as the counter and reference electrode and WO_3 , LTO, and NMC as the working electrode inside an argon-filled glove box (moisture and O_2 level <1 ppm). Celgard 2500 with a film thickness of 25 μm was used as a separator. For the first project, the liquid electrolyte consisting of 1M $LiPF_6$ dissolved in a mixed solvent of ethylene carbonate (EC), dimethyl carbonate (DMC), and diethyl carbonate (DEC) in the volume ratio of 4:2:4. The amount of electrolyte used was 100 μL during each cell fabrication. For the second & third project, the liquid electrolyte consisting of 1M $LiPF_6$ dissolved in a mixed solvent of ethylene carbonate (EC) and diethyl carbonate (DEC) in the volume ratio of 1:1. The amount of electrolyte used was 60 μL during each cell fabrication.

Symmetrical cell test and full cell test measurements of the coin cells done using the LAND CT2001A system.

3.4.1 Cyclic voltammetry and electrochemical impedance spectroscopy

Cyclic voltammetry (CV) was performed by an electrochemical workstation (Ametek VERSASTAT3-200 and EC Lab potentiostat). The CV measurement was carried out in different potential ranges for multiple cycles in the range 0.1 to 3 V and in a single cycle from -0.2 V to 0.2 V for linear sweep voltammetry. The electrochemical impedance

spectroscopy (EIS) measurement was carried out using the same electrochemical workstation with a 10mV amplitude AC signal, where the frequency range used was from 100 kHz to 0.1 Hz. Figure 3.7 shows the available set up for measuring CV and EIS in our Lab.

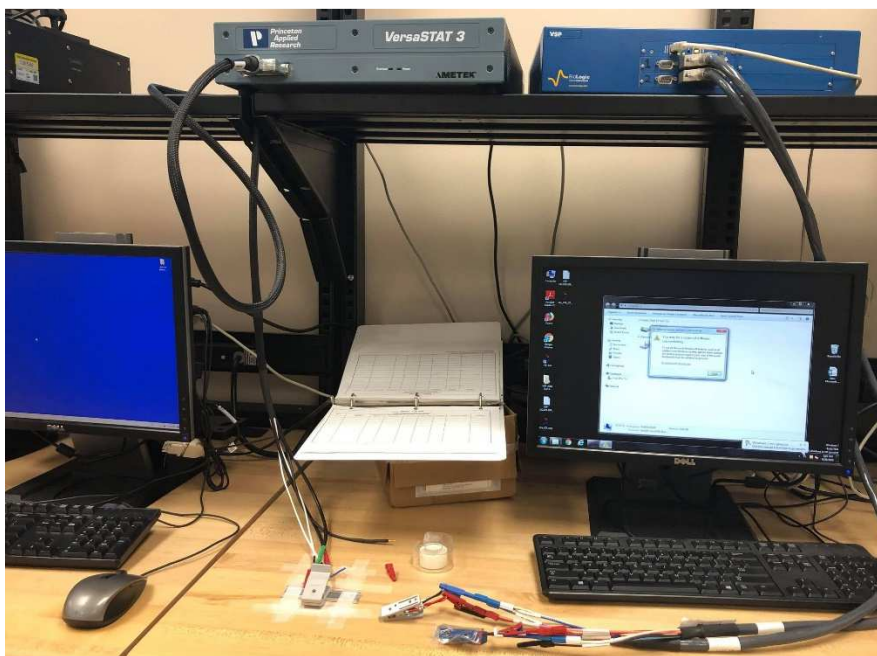


Figure 3. 7 The picture of VERSASTAT and EC-Lab device for measuring CV and EIS.

3.4.2 Symmetrical cell and full cell test

Galvanostatic charge-discharge measurements of the coin cells were carried out using the LAND CT2001A system and Neware battery analyzer. Figure 3.8 shows the digital photograph of Neware battery analyzer located in DEH 32 at SDSU. The symmetrical cell test was carried out using different current density up to 5 mA cm^{-2} to achieve a different capacity such as 1 mAh cm^{-2} to 3 mAh cm^{-2}). LTO and NMC were cycled between 1V to 3 V, and 2.7 V to 4.2 V at 0.1 C for the first 5 cycles and 1C for the following cycles,

respectively. For rate performance, cells were cycled at 0.1 C, 0.2 C, 1C, 3 C, 5 C, and again back to 0.1 C.



Figure 3. 8 Picture showing the Neware battery analyzer used for galvanostatic charge and discharge.

CHAPTER 4: RESULTS AND ANALYSIS

4.1 Self-recovery of capacity in the WO₃ anode material

Although the transitional metal oxides are considered promising anode materials, they suffer from poor electronic conductivity and volume expansion issues. In this first project, we tried to modify the commercially available tungsten trioxide (WO₃) by incorporating urea and annealing at a high temperature of 500 ° C under the N₂ environment. This technique created the defects and oxygen vacancies in the WO₃ anode material, improving the electronic property. As a result improved electrochemical battery cycling performance was achieved.

4.1.1 Structural characterization

Figures 4.1 (a,b) shows the XRD patterns and Raman spectra, respectively, for P-WO₃ and R-WO₃. In XRD, it can be observed that the sharp crystalline peaks of P-WO₃ become broader in R-WO₃ suggesting the transformation to amorphous, indicating the creation of oxygen vacancies [125-128]. The peaks observed at 2 θ of $\sim 26^\circ$, 28° , 36° , 41.8° , 44° , 46° , 63° , 71° , and 77° , respectively in P-WO₃ are disappeared in R-WO₃. Besides, new peaks are observed at 2 $\theta \sim 41^\circ$, $\sim 54^\circ$, and $\sim 58^\circ$ in R-WO₃, indicating the successful reduction of P-WO₃ reports [21, 128, 129].

In Raman spectra, it can be observed that the main peaks at $\sim 264\text{ cm}^{-1}$, $\sim 324\text{ cm}^{-1}$, $\sim 710\text{ cm}^{-1}$, and $\sim 801\text{ cm}^{-1}$ in P-WO₃ become broader in R-WO₃ which indicates the transformation to the amorphous phase, due to the creation of oxygen vacancies[124, 128]. Figures 4.1(c,d) shows the AFM topography of P-WO₃ and R-WO₃. Figures 4.1(e,f) shows the high-resolution AFM corresponding to Figures 4.1(c,d). It can be observed that the particles of R-WO₃ are comparatively smaller than that of P-WO₃. The decrease in particle

size decreases the time of Li-ion transport [130]. To further calculate the specific surface area (SSA), BET measurement was carried out. BET measurement calculates the SSA of P-WO₃ and R-WO₃ to be 4.59 m² g⁻¹ and 47.59 m² g⁻¹, respectively. The increase in surface area wets the larger surface of the electrode with electrolyte, providing quick and excess Li-ion transport.

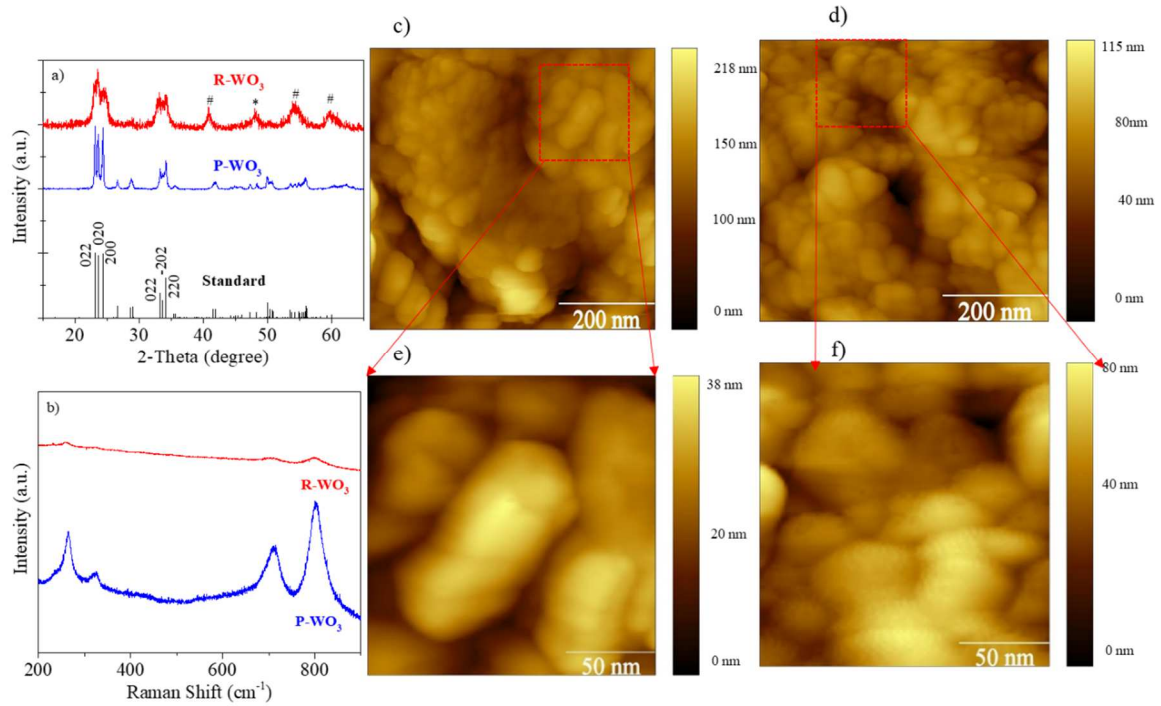


Figure 4. 1: (a) XRD patterns, (b) Raman spectra and (c-d) AFM surface topography for P-WO₃ and R-WO₃, and (e,f) shows the high-resolution AFM of (c-d).

The Scherrer equation: $\tau = K\lambda/\beta \cos\theta$, where θ is the usual Bragg angle, λ is the radiation wavelength, β is peak width and K is a constant at 0.9, was used to measure the average crystallite size of P-WO₃ and R-WO₃. The average crystallite size of R-WO₃ is smaller compared to that of P-WO₃. This can be attributed to the annealing in the inert environment and the creation of oxygen vacancies [131]. The smaller particle increases the charge transport mechanism by shortening the diffusion path lengths [131-134]. Table 4.1 shows

the results of the EDS analysis. It can be observed that the weight percentage of Oxygen (O) decreased from 69.79 % to 67.93% indicating the successful reduction or creation of oxygen vacancy in R-WO₃.

Table 4. 1 Weight percentage of oxygen (O) and tungsten (W) in P-WO₃ and R-WO₃.

	Element	Line	Intensity (c/s)	Conc. (wt%)
P-WO ₃	O	K α	69.78	21.739
	W	L α	18.91	78.261
R-WO ₃	O	K α	67.93	19.718
	W	L α	21.23	80.282

4.1.2 Electrochemical characterizations

Figure 4.2 shows the electrochemical battery cycling performance. At a constant rate of 100 mA g⁻¹ as shown in Figure 4.2(a), R-WO₃ delivered a higher first discharge capacity of 959.15 mAh g⁻¹ versus 670.16 mAh g⁻¹ for P-WO₃. There was continuous capacity fading in P-WO₃ which reaches to 236.5 mAh g⁻¹ at the 100th cycle. In contrast, R-WO₃ showed unusual behavior of capacity recovery after a few cycling with repetition. The self-recovery was observed at various cycles (at 15th, 36th, and 45th cycle), and the discharge/charge capacity remain steady to ~558.68 mAh g⁻¹/550.23 mAh g⁻¹ at 100th cycle. Such a phenomenon of self-recovery in R-WO₃ can be attributed to the formation of defects or active sites due to the creation of oxygen vacancies which activates with higher cycling. Figure 4.2(b) shows the rate capability test starting from a current density of 35 mA g⁻¹ to 280 mA g⁻¹ and again back to 35 mA g⁻¹. R-WO₃ showed higher capacity at each current density compared to P-WO₃. The discharge/charge specific capacity at different current densities are summarized in Table 4.2. For, R-WO₃, the capacity retention at the 22nd cycle compared to the 2nd cycle was 94.22%. In contrast, P-WO₃, the specific charge capacity

retention at the 22nd cycle compared to the 2nd cycle was 87.96%. The higher capacity retention and higher capacity at higher current density can be attributed to the chemical stability and higher electronic conductivity, higher specific surface area of the electrode materials. Similarly, P-WO₃ and R-WO₃ showed the first CE of 60.25% and 66.62%, respectively as shown in Figure 4.2(c,d) and remain as high as 99.5% at higher cycles. Figures 4.2(e,f) shows the voltage versus specific capacity profile for P-WO₃ and R-WO₃, respectively. It can be observed that R-WO₃ shows a higher sloping profile than the P-WO₃, indicating excess Li-ion storage.

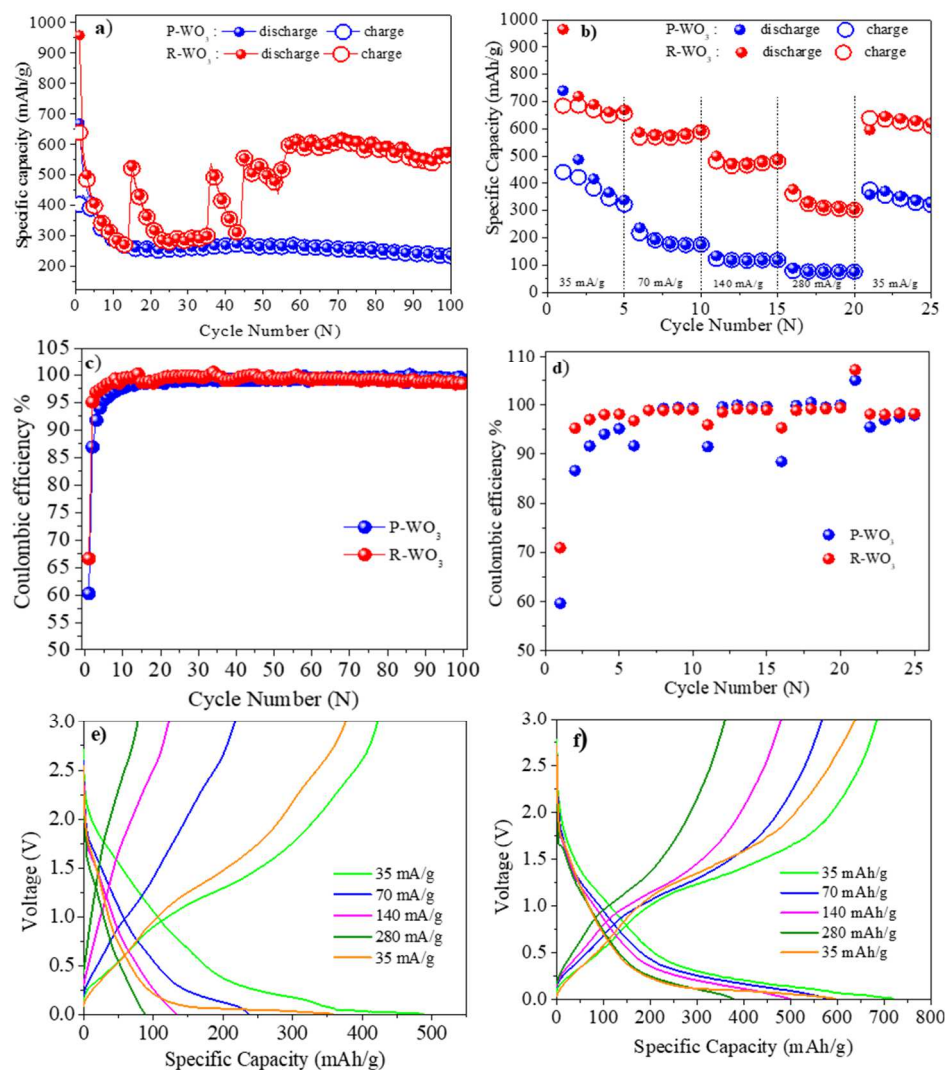


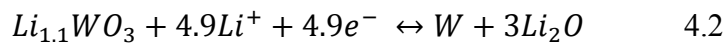
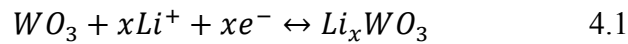
Figure 4. 2: Electrochemical battery cycling performance at (a) constant rate, (b) different rates, (c,d) corresponding CE and (e,f) corresponding voltage profile.

Table 4. 2 Rate capability test of P-WO₃ and R-WO₃.

Cycle number	Current density (mA/g)	Discharge/charge capacity (mAh/g)	
		P-WO ₃	R-WO ₃
1 st	35	739.6/441.1	964.9/684.6
2 nd	35	487.2/422.2	719.2/685.3
6 th	70	237.0/217.4	586.7/568.0
11 st	140	133.7/122.4	500.3/480.1
16 th	280	88.3/87.1	378.2/360.7
22 nd	35	354.7/371.4	633.7/645.7

Figure 4.4(a,b) shows the CV measurement and voltage-specific capacity profile of P-WO₃. Figure 4.4(c,d) shows the CV measurement and voltage-specific capacity profile of R-WO₃. During lithiation, the appearance of the voltage peak at 2.3 V, 0.59 V, and 0.01 indicates the reaction between the Li and WO₃. The peak at 2.3 V represents lithiation of WO₃ to Li_xWO₃ and the peak at 0.59 V represents the conversion of Li_xWO₃. The voltage peak at 0.01 indicates the conversion of W⁺ to W⁰ and/or Li plating^[135, 136]. Similarly, during delithiation, the voltage peak at 1.2 V represents the oxidation of W to Li_xWO₃, and the voltage peak at 2.0 V indicates the formation of WO₃ [135]. The CV measurement is in good agreement with the voltage profile. The R-WO₃ shows the sharp peaks even at higher cycles but P-WO₃ shows the flat shape of the CV curve. This indicates that R-WO₃ is electrochemically active and stable indicating the sufficient charge storage mechanism. In contrast, P-WO₃ shows the disappearance of peaks and voltage plateau with higher cycles, indicating the surface storage only. Figure 4.4(e) shows Tauc's plot of both P-WO₃ and R-WO₃. The bandgap of R-WO₃ (~2.32 eV) is lower than P-WO₃ (~2.85 eV), indicating higher electronic conductivity in R-WO₃. The Nyquist plot in Figure 4.4(f) that the charge transfer resistance (R_{ct}) of R-WO₃ is greatly reduced to 135.1 Ω which was 1195.0 Ω for P-WO₃. The significant decrement in R_{ct} and increment of electronic conductivity of R-WO₃ improves the charge transport mechanism. As a result, the improved battery cycling performance was achieved in R-WO₃ compared to P-WO₃.

The reaction mechanism during lithiation/delithiation in WO₃ anode material is as follows.



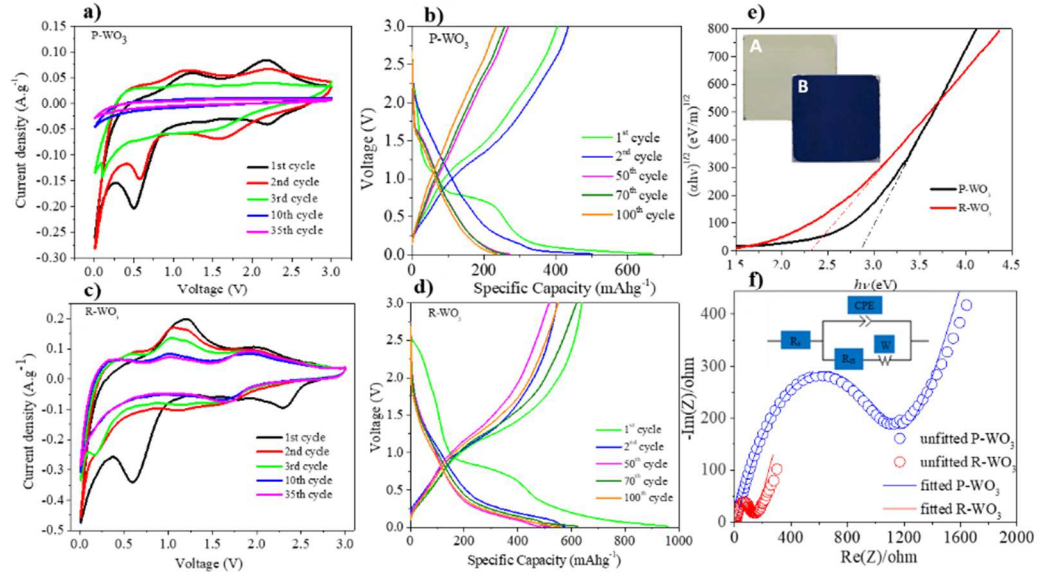


Figure 4. 3: (a,c) CV measurement b,d voltage versus specific capacity, (e) Tauc plot, and (f) Nyquist plot of P-WO₃ and R-WO₃.

To further understand the self-recovery mechanism cells were disassembled to carry out SEM and XRD analysis. Figure 4.4(a) shows the electrochemical cycling performance up to the 1st self-recovery discharge. Figure 4.4(b) shows the corresponding voltage versus specific capacity for the first self-recovery cycle. Figure 4.4(c,d) shows the surface topography SEM image of the R-WO₃ electrode before cycling and after cycling at which the self-recovery was obtained. The SEM images as shown in Figure 4.4(d) show that the surface has dense morphology which can be due to the Li plating. To confirm the existence of Li on the surface of the R-WO₃ electrode, XRD was carried out. From the XRD, we can see the presence of Li peak, implying the plating of Li. A similar observation was reported in graphite-based anode material where the Li storage was due to the Li plating and Li-intercalation mechanism [137].

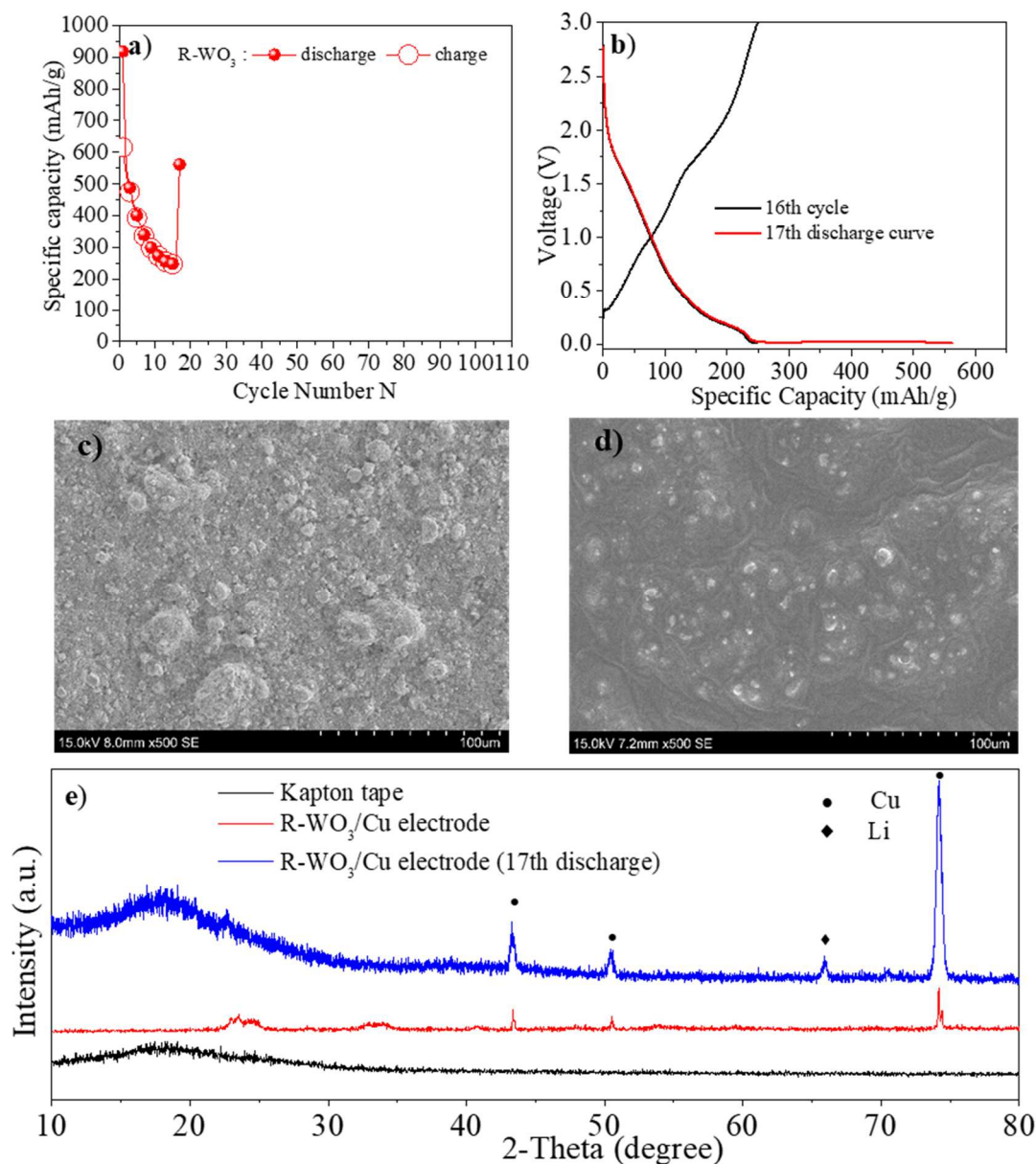


Figure 4. 4: (a) Electrochemical cycling performance of R-WO₃, (b) corresponding voltage profile, (c,d) SEM images of the R-WO₃ electrode before and after observing self-recovery, and (e) XRD of Kapton tape, the R-WO₃ electrode before cycling, and after 17th discharge.

4.2. Development of *ex-situ* ASEI by a physical deposition method

In this second project, the development of *ex-situ* artificial SEI was developed by R-F sputtering techniques. The ultrathin bilayer of graphite and SiO₂ was deposited on the Li

metal surface. Different thickness of graphite and SiO₂ was deposited separately and optimized to be 20 nm for each. For the bilayer, initially, the graphite was deposited on top of Li metal followed by the deposition of SiO₂.

4.2.1 Material characterizations

Figure 4.4(a) shows the Raman spectroscopy with characteristics D and G peaks at $\sim 1350\text{ cm}^{-1}$ and $\sim 1572\text{ cm}^{-1}$. The I_D/I_G ratio of ~ 0.51 indicates an excess amount of graphite in the sputtered film. The presence of a 2D peak $\sim 2696\text{ cm}^{-1}$ indicates the defects associated with the graphite. To explore the chemical composition on the surface of graphite-SiO₂ Li, XPS measurement was carried out. The presence of C 1s spectra with the binding energy (BE) at $\sim 284.5\text{ eV}$ can be assigned to Sp^2 hybridized C-C bond as shown in Figure 4.4(b), indicating the presence of graphite. The BE at $\sim 103.3\text{ eV}$ Figure 4.4(c) and $\sim 532.71\text{ eV}$ (Figure 4.4d) indicates the Si 2p and O 1s core level, indicating the successful deposition of SiO₂.

To investigate the electrolyte wettability of the electrode, contact angle measurement was performed. The bare Li electrode shows a contact angle of $\sim 43^\circ$ Figure 4.4(e) and graphite-SiO₂ Li shows almost zero as shown in Figure 4.4(f) contact angle with the electrolyte. This indicates that graphite-SiO₂ has a higher affinity towards electrolyte, implying faster Li-ion transport. As a result, improved battery performance was obtained.

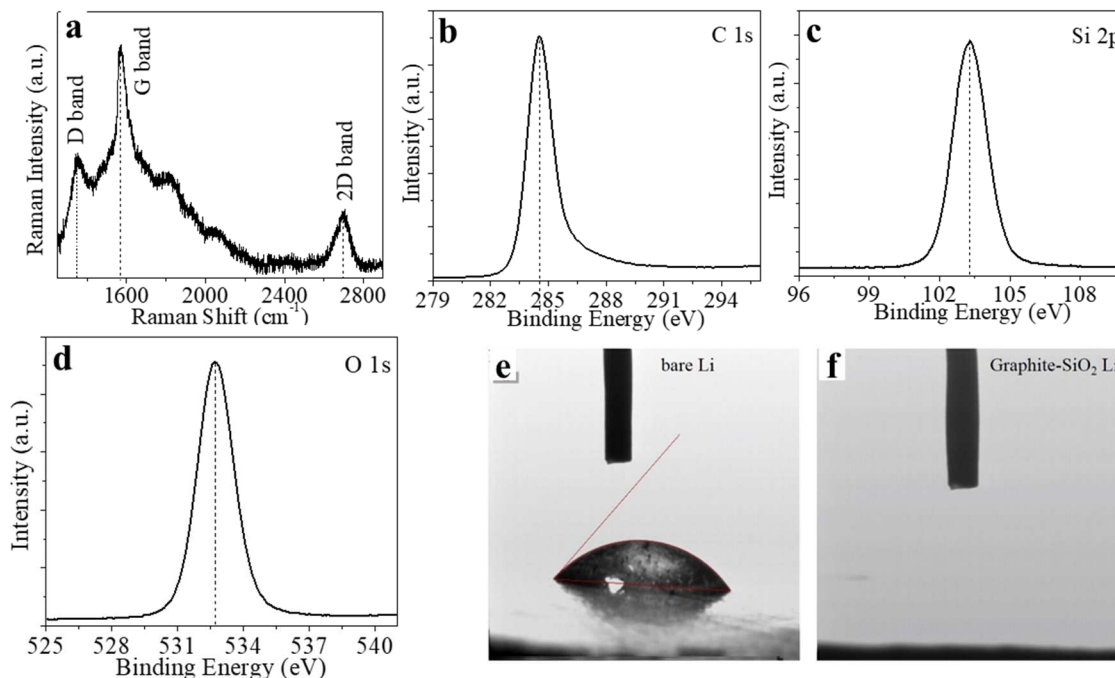


Figure 4. 5: (a) Raman spectroscopy of graphite sputtered on Li, (c-d) XPS analysis of graphite and SiO₂ sputtered on Li and (e,f) Contact angle measurement of bare Li and graphite-SiO₂ Li using electrolyte solvent.

Figure 4.6(a,b) shows the SEM images of bare Li and graphite-SiO₂ deposited Li. The surface roughness and Young's modulus of the Li metal electrode were measured using AFM. The bare Li shows higher roughness of 520.1 nm compared to graphite-SiO₂ Li ((324.5 nm). The higher roughness of the electrode surface can create protuberance which acts as a hotspot. These hotpots generate non-uniform Li-ion flux during plating/stripping cycles, favoring the Li dendrite growth. Besides the graphite-SiO₂ Li shows an average Young's modulus of 10.7 GPa and bare Li shows the average Young's modulus of 0.23 GPa. The root means square (RMS) roughness and Young's modulus results are summarized in Table 4.3. Higher Young's of artificial SEI provides mechanical strength to suppress the Li dendrite growth. As a result, we can observe that the bare Li after 1st

plating shows the formation of sharp needle-shaped Li dendrites Figure 4.6(g). After 100th plating cycles, the surface of bare Li has mossy-like morphology and formation of inactive dead lithium as shown in Figure 4.6(h). In contrast, graphite-SiO₂ Li has uniform Li deposition after 1st plating and 100th plating cycles as shown in Figure 4.5(i,j).

Table 4. 3 Table showing the average Young's modulus and RMS roughness.

	Average Young's modulus	RMS roughness
bare Li	0.23GPa	520.1nm
Graphite-SiO ₂ Li	10.7GPa	324.5nm

The deposited SiO₂ film was not detected from XRD due to its amorphous nature as confirmed from XRD as shown in Figure 4.6(k). Only the XRD peaks for Li and Kapton tape were observed. The amorphous nature of SiO₂ is favorable for lithiation/delithiation. In general, bulk SiO₂ does not react with Li.

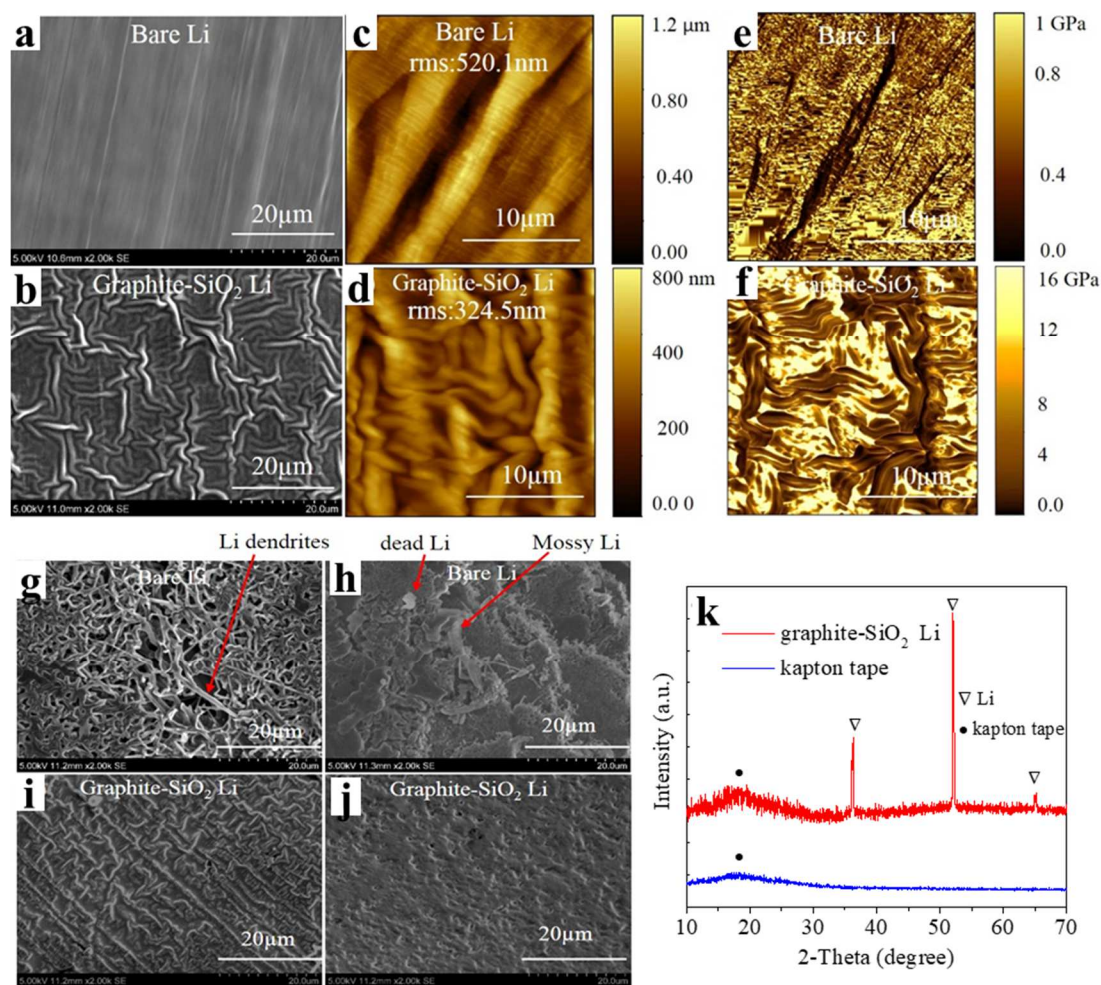


Figure 4. 6: SEM images of (a) bare Li and (b) graphite-SiO₂ Li, corresponding AFM images of (c) bare Li and (d) graphite-SiO₂ Li, (e,f) corresponding Young's modulus measurement of bare Li and graphite-SiO₂ Li, SEM image of (g, h) bare Li and (i, j) graphite-SiO₂ Li after 1st plating and 100th plating and (k) XRD of the graphite-SiO₂ Li.

Figure 4.7(a,b) shows the cross-sectional SEM images of the bare Li and graphite-SiO₂ Li after 100th plating/stripping cycles. Figure 4.7(c,d) shows the corresponding high-resolution SEM images. The bare Li shows the formation of dendritic Li with a higher thickness of Li deposition. The higher thickness indicates the irreversible Li deposition which increases the impedance of the battery as the plating/stripping cycle increases,

resulting in battery failure. The higher surface area of Li dendrite consumes both Li and liquid electrolyte resulting in low CE. In contrast, graphite-SiO₂ Li has a very thin layer and dendrite-free Li deposition. This implies the reversible Li plating/stripping without the formation of dead Li. The scratches and dents in the bare Li (Figure 4.7e) generate a non-uniform electric field leading to the formation of non-uniform Li-ion flux.

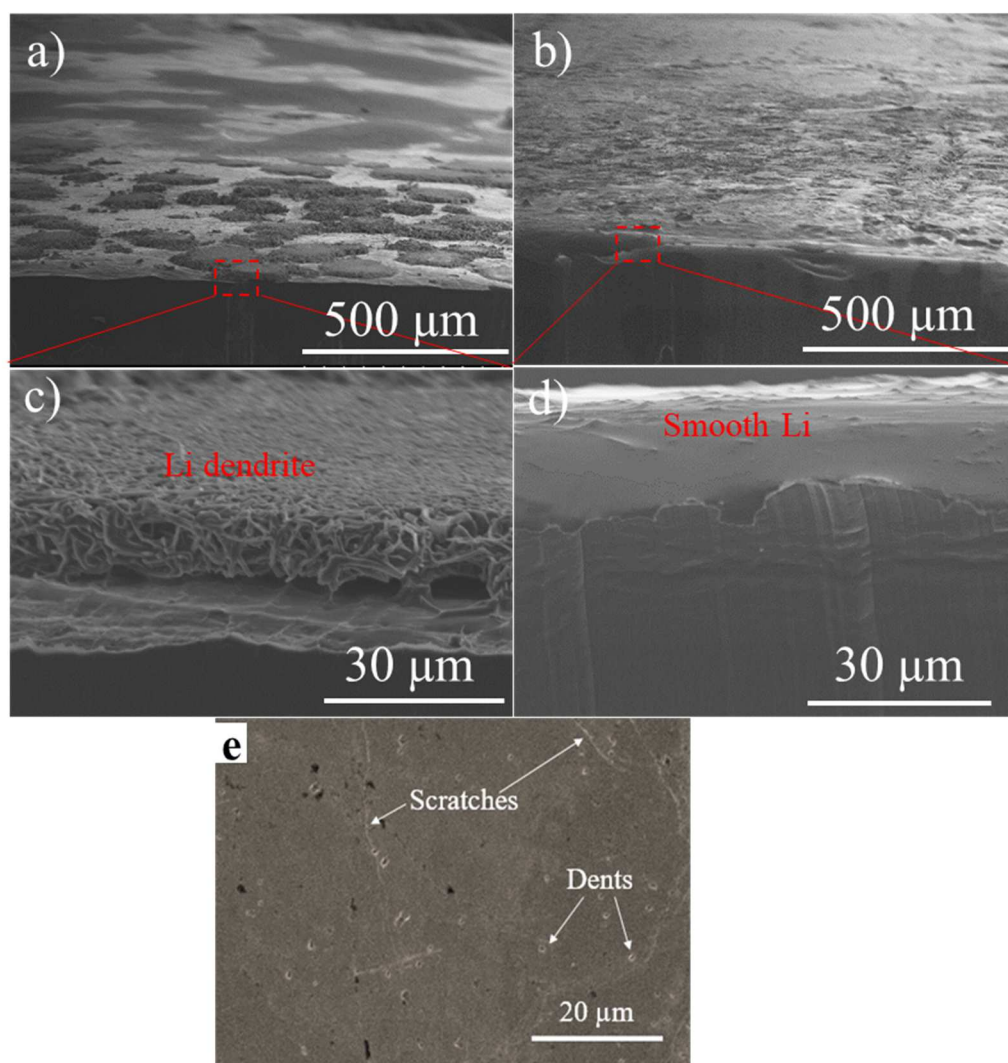


Figure 4. 7: SEM images of (a,c) bare Li (b,d) graphite SiO₂ Li after 100th plating /stripping cycles and (e) high-resolution SEM image of bare Li showing the scratches and dents in bare Li.

XPS analysis was carried out on the graphite-SiO₂ Li electrode before and after the 50th plating and 50th stripping cycles to understand the composition on the surface of Li. The observed Si 2p and O 1s spectra of SiO₂ shifts after 50th plating and after 50th stripping cycles. The peak centers of Si 2p and O 1s at a binding energy of 103.3 eV and 532.71 eV, respectively, indicate the deposition of SiO₂ [138, 139]. After 50th plating as shown in Figure 4.8(a), the peak centers of both Si 2p and O 1s shift to ~102.7 eV and 531.6 eV, respectively, which can be attributed to the formation of Li₂Si₂O₅ [138-140]. At 50th stripping as shown in Figure 4.8(b), the peak centers of both Si 2p and O 1s again shift back towards the original BE. The higher peak centers of both Si 2p and O 1s binding energy ~103.1 eV and ~ 532.5 eV, respectively, indicates the delithiation of Li₂Si₂O₅ and complex irreversibility of Li₄SiO₄. This phenomenon indicates the appearance of electrochemical lithiation/delithiation of amorphous SiO₂. Figure 4.8(c) shows the CV measurement of bare Li and graphite SiO₂ deposited Li symmetrical cell. The straight line indicates the storage of Li by the plating/stripping mechanism in the bare Li symmetrical cell. In graphite/SiO₂ Li the redox peaks can be observed. This is the indication of electrochemically active thin-film SiO₂. In addition to the Li plating/stripping mechanism, the lithiation/delithiation is another mechanism that can store Li in the graphite SiO₂ Li electrode. As a result, excess Li can be stored and higher capacity at higher current density rates can be expected.

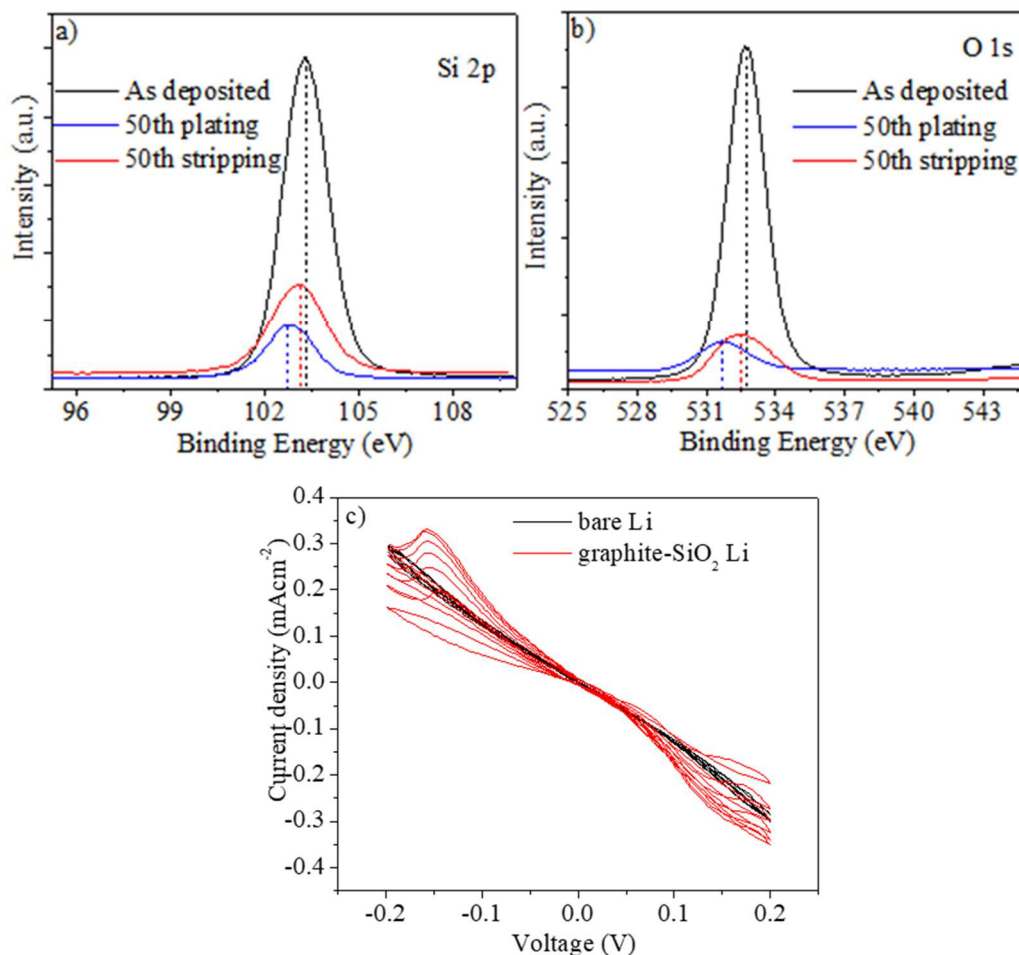


Figure 4. 8: (a,b) XPS analysis on the graphite-SiO₂ electrode before and after the 50th plating and 50th stripping cycle and (c) CV measurement of graphite-SiO₂ Li electrode for 5 cycles.

4.2.2 Electrochemical characterizations

The symmetrical cell test was carried out to optimize the thickness of graphite and SiO₂ deposited on the surface of Li. Figure 4.9 shows that 20 nm graphite shows the best plating/stripping cycles with longer plating/stripping hours and lower voltage hysteresis compared to 10 nm and 30 nm graphite. The lower thickness of the graphite may not fully cover the surface of Li. As a result, there will be direct contact between the liquid

electrolyte and bare Li. This results in the consumption of both liquid electrolyte and lithium. Thus, the electrolyte dry-out occurs in the cell, resulting in poor CE and capacity fading. In comparison, the higher thickness (30 nm) of graphite may retard the Li-ion transport which increases the impedance of the battery. Similarly, the thickness of SiO_2 was also optimized to 20 nm, assuming it will fully protect the lithium metal anode. The symmetrical cell test with 30 nm SiO_2 deposited on Li is shown in Figure 4.9b.

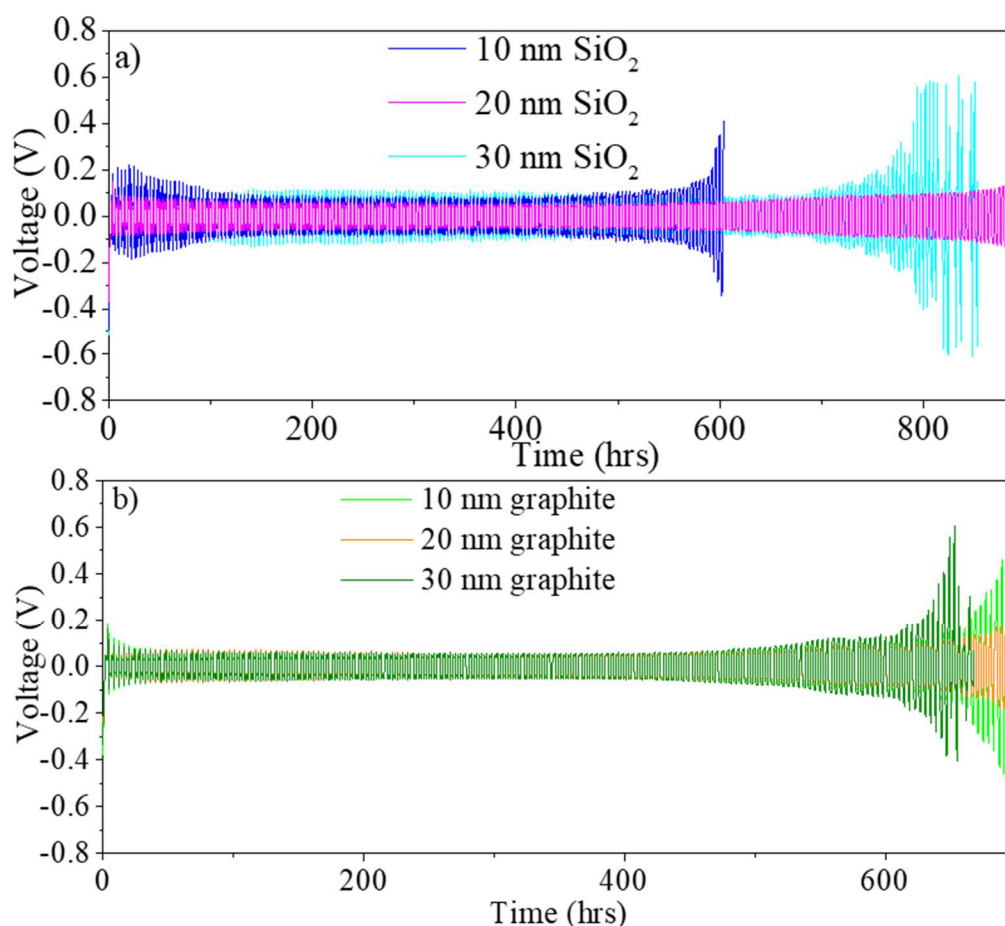


Figure 4. 9: Symmetrical cell test with different thicknesses of (a) SiO_2 and (b) graphite.

The stability test of bare Li and graphite- SiO_2 Li was carried out in the air and the carbonate-based electrolyte. The bare Li and the graphite- SiO_2 Li electrodes were kept outside the Ar-glove box in the air with 51% humidity at 66 °F. The bare Li electrode

quickly changes to black and is completely dark in 1 hour, covering the surface of the Li metal anode (Figure 4.10a). The chemical reaction between the hyperactive lithium metal and the air or moisture can form chemical compounds such as lithium hydroxides (LiOH), lithium nitrides (Li₃N), lithium carbonates (Li₂CO₃), and lithium oxides (Li₂O/Li₂O₂). In contrast, the graphite-SiO₂ protected Li metal gradually changes the color, and even after 1 hr it was not fully black implying the effectiveness of bilayer in inhibiting the side reactions of hyperactive lithium metal and air/moisture. Further, the stability test was carried out by immersing the bare Li and graphite-SiO₂ Li on the carbonate-based electrolyte for 4 days using the same amount of electrolyte (3 ml) for both cases (Figure 4.10b). The surface of bare Li changes from shiny silver color to mixed different colors with an extra layer, which can be attributed to the side reaction and consumption of both Li and liquid electrolyte. However, the graphite-SiO₂ Li still looks the same to its original color, implying the hyperactive lithium metal is well protected. As a result, higher CE and stable electrochemical cycling performance can be expected with graphite-SiO₂ modified lithium metal anode.

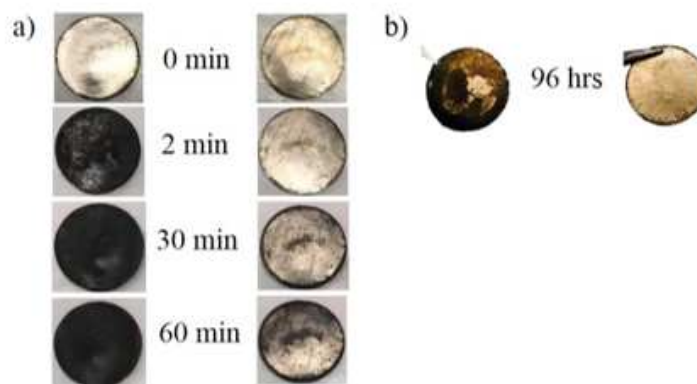


Figure 4. 10: (a) Air and (b) liquid electrolyte stability of a bare Li and graphite-SiO₂ Li.

Figure 4.11(a,b) shows the Nyquist plot of both bare Li and graphite-SiO₂ Li symmetrical cells as a function of days. The Z-real axis in the Nyquist plot represents the series resistance, which is the bulk resistance of all the components (such as electrolyte, separator, and spacer) of the battery [141]. The graphite-SiO₂ Li symmetrical cell shows two semi-circles, where the first semicircle in the high-frequency region represents the interfacial resistance of SEI and the second semicircle in the lower frequency region represents the charge transfer resistance between the SEI (graphite/SiO₂) and the liquid electrolyte [69, 83, 110, 142-144]. The bare Li symmetrical cell shows a single semicircle as it has no artificial SEI. The *in-situ* formed SEI by the side reaction between the bare Li and the liquid electrolyte is too thin and does not fully cover the surface of bare Li [143]. Initially, the bare Li and graphite-SiO₂ Li symmetrical cells show a charge transfer resistance R_{ct} of $\sim 588 \Omega$ and 124Ω , respectively. In the bare Li symmetrical cell, the R_{ct} increases quickly to 1313Ω continuously after 20 days and does not show any steady-state [110]. In contrast, R_{ct} of the graphite-SiO₂ Li symmetrical cell slowly increased and comes to a steady-state after 15 days. This implies that there is a continuous side reaction between the bare Li and the electrolyte but the graphite and SiO₂ bilayer effectively inhibits the side reaction between the Li metal and liquid electrolyte. The stabilized SEI and higher electrolyte affinity of SiO₂ enhance the Li-ion transport without any side reactions [145, 146]. In contrast, the bare Li reacts with electrolyte resulting in the formation of thick carbonate-rich unstable SEI and an insulating surface [110]. All the impedance results are summarized in Table 4.4. The lower charge transfer resistance was also achieved in the graphite-SiO₂ Li symmetrical cell as shown in Figure 4.11(c), compared to the bare Li, which can be attributed to the stabilized SEI and dendrite-free Li deposition.

To investigate the stability of the SEI and the morphology of Li deposition, the symmetrical cell test was carried out at different current density rates. Figure 4.11(d) shows the Li plating/stripping at 0.5 mA cm^{-2} to achieve a capacity of 1 mAh cm^{-2} and Figure 4.11(e) shows the corresponding voltage hysteresis with cycle number. The voltage hysteresis is defined as the average difference between the discharging potential and charging potential plateau [147]. It can be observed that the bare Li symmetrical cell dies earlier than the graphite-SiO₂ Li symmetrical cell. In bare Li, the unstabilized SEI and continuous side reactions lead to the electrolyte dry-out and increase in the cell's impedance. The large fluctuations in the plating/stripping voltage curve were also observed in the bare symmetrical cell. In contrast, the graphite-SiO₂ Li symmetrical cell shows longer plating/stripping hours with substantially reduced overpotential. The introduction of an artificial protective layer leads to the stable SEI and inhibition of the side reaction between the Li metal and liquid electrolyte. Figure 4.11(f,g) shows the Li plating/stripping voltage versus time profile and corresponding voltage hysteresis at a current density of 1 mA cm^{-2} to achieve a capacity of 1 mAh cm^{-2} . The longer plating/stripping hours with reduced overpotential or voltage hysteresis was achieved with graphite-SiO₂ Li symmetrical cell compared to the bare Li symmetrical cell. An improved symmetrical cell test was obtained for graphite-SiO₂ Li symmetrical cells while plating/stripping at various higher current density rates and capacities as shown in Figure 4.12 and Figure 4.13. The improved plating/stripping in graphite-SiO₂ Li can be attributed to the synergetic advantage of using graphite and SiO₂. Graphite provides high electronic conductivity to bridge the plated Li with bulk Li electrode and offers flexibility to buffer the volume expansion of Li. Besides,

SiO₂ has higher electrolyte wettability, sufficient Li-ion diffusion, poor electronic conductivity, and high Young's modulus.

Table 4. 4 Impedance results of the symmetrical cell using bare Li and graphite-SiO₂ Li.

	bare Li			graphite-SiO ₂ Li		
	R _s (Ω)	R _{int} (Ω)	R _{ct} (Ω)	R _s (Ω)	R _{int} (Ω)	R _{ct} (Ω)
Fresh	5.08	-	588.60	14.03	226.40	124.40
2days	6.66	-	764.20	9.99	267.90	252.70
5days	6.97	-	921.60	8.35	286.90	267.60
10days	8.59	-	1110.00	10.64	350.50	256.30
15days	9.26	-	1230.00	9.96	426.5	278.8
20days	11.66	-	1313.00	10.95	430.30	278.10

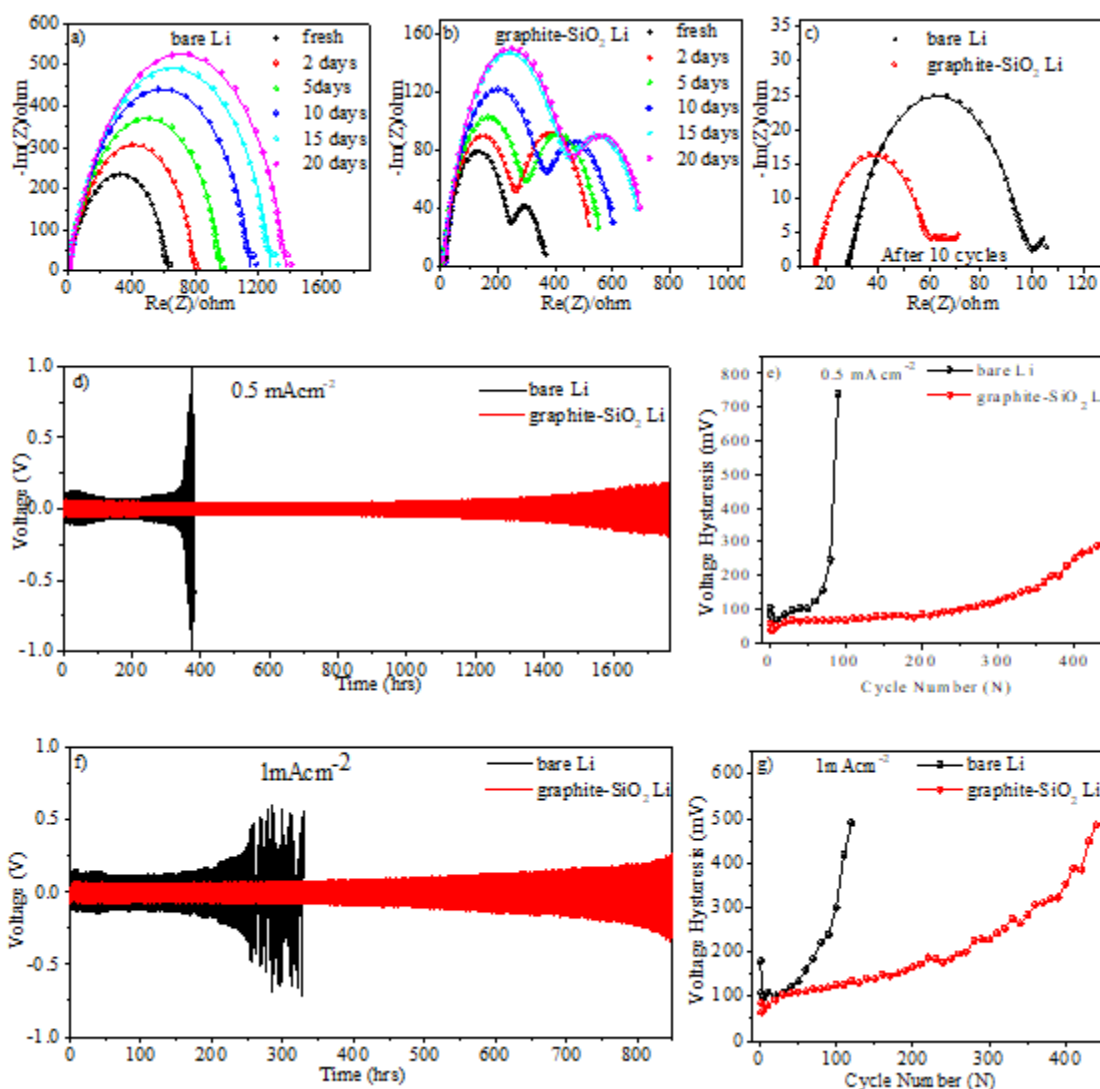


Figure 4. 11: (a,b) Nyquist plot a,b as a function of days, (c) Nyquist after 10 cycles of plating/stripping cycles, (d,e) plating/stripping cycle and corresponding voltage hysteresis at a current density of 0.5 mA cm⁻² and (f,g) plating /stripping cycle and corresponding voltage hysteresis at a current density of 1 mA cm⁻²

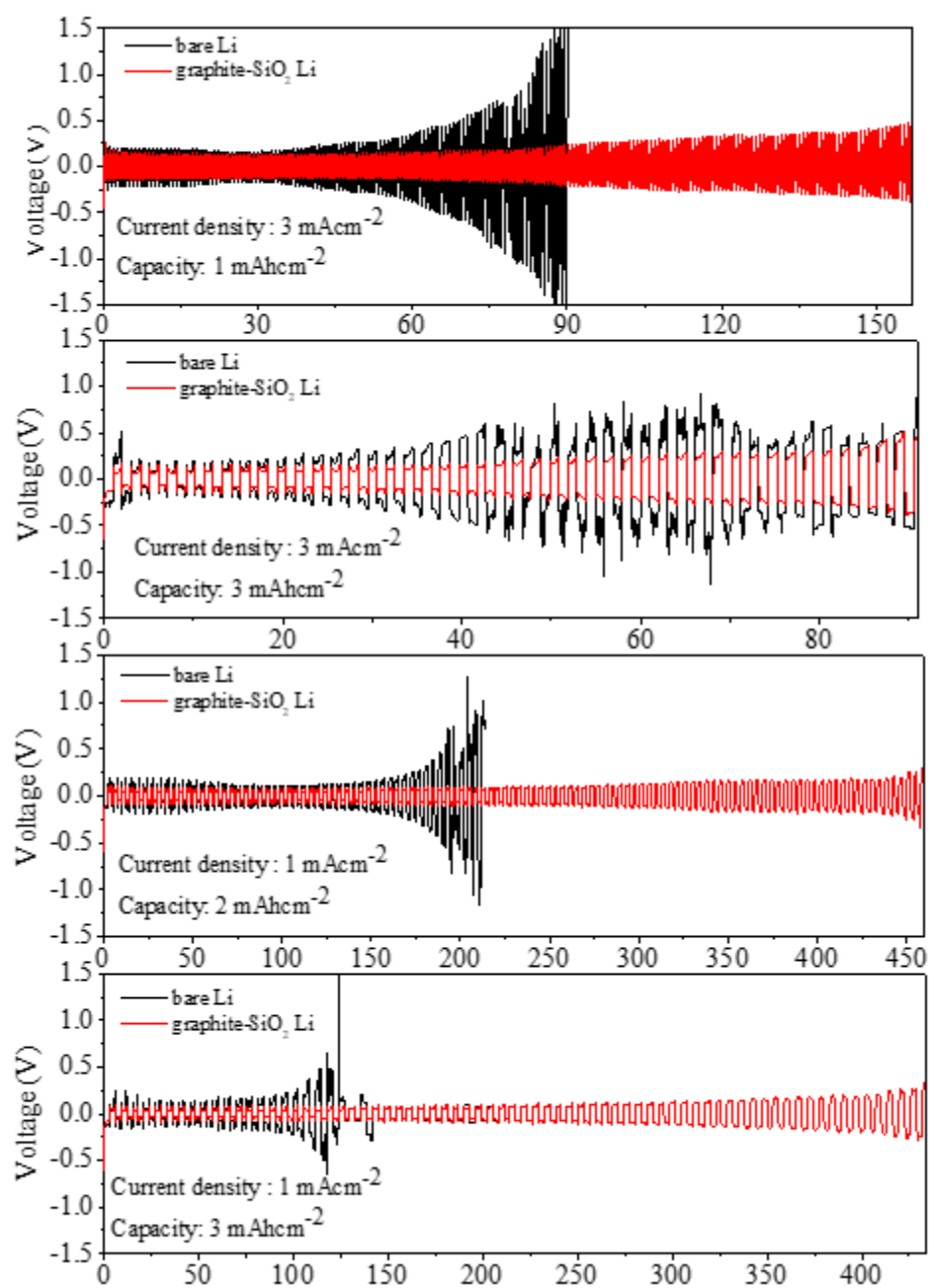


Figure 4. 12: Symmetrical cell plating/stripping performance at various current densities and capacities.

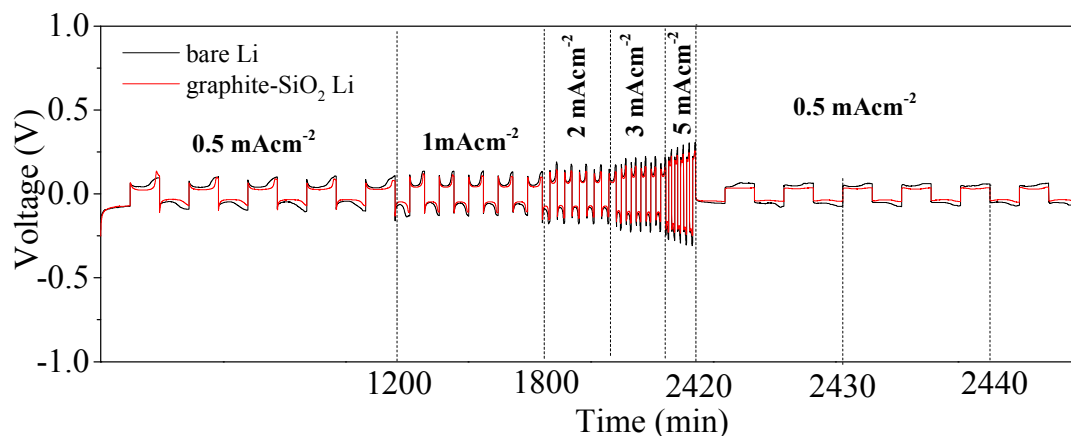


Figure 4. 13: Symmetrical cell plating/stripping performance at various current density to achieve a capacity of 1 mAh cm^{-2} .

To understand the practical applications of the graphite-SiO₂ modified Li anode, the full cell tests were carried out using lithium titanate (LTO) and lithium nickel cobalt manganese oxide cathode (NMC111) as cathodes. LTO is considered as a zero-strain stable and safe material for the battery electrode [148, 149]. The battery cycling was done at the current density rate of 0.1 C for the first five cycles and then at 1C for the rest cycles. The bare Li shows the first CE of 86.43% and graphite-SiO₂ Li shows a first CE of 84.34%. The lower CE for the bare Li can be assigned to the side reaction and formation of SEI. The lower CE for graphite-SiO₂ Li can be attributed to the impedance of artificial SEI and the formation of *in-situ* SEI both [142, 150]. With higher cycling, the CEs were stabilized more than 99%. Figure 4.14(a,b) shows the cycling performance of NMC and LTO cathodes, respectively using bare Li and graphite-SiO₂ Li anode. Figure 4.11(c,d) shows the corresponding voltage profile at a specific cycle number. The bare Li shows quick capacity

fading and large voltage overpotential when paired with LTO or NMC. In contrast, graphite-SiO₂ Li showed significant improvement in capacity and reduced overpotential. The bare Li when couple with NMC shows capacity retention of ~ 50% at the 150th cycle and when coupled with LTO shows capacity retention of ~ 80% at the 400th cycle. In contrast, graphite-SiO₂ Li anode paired with NMC shows capacity retention of ~ 74% at the 150th cycle and when coupled with LTO shows capacity retention of ~88% at the 400th cycle.

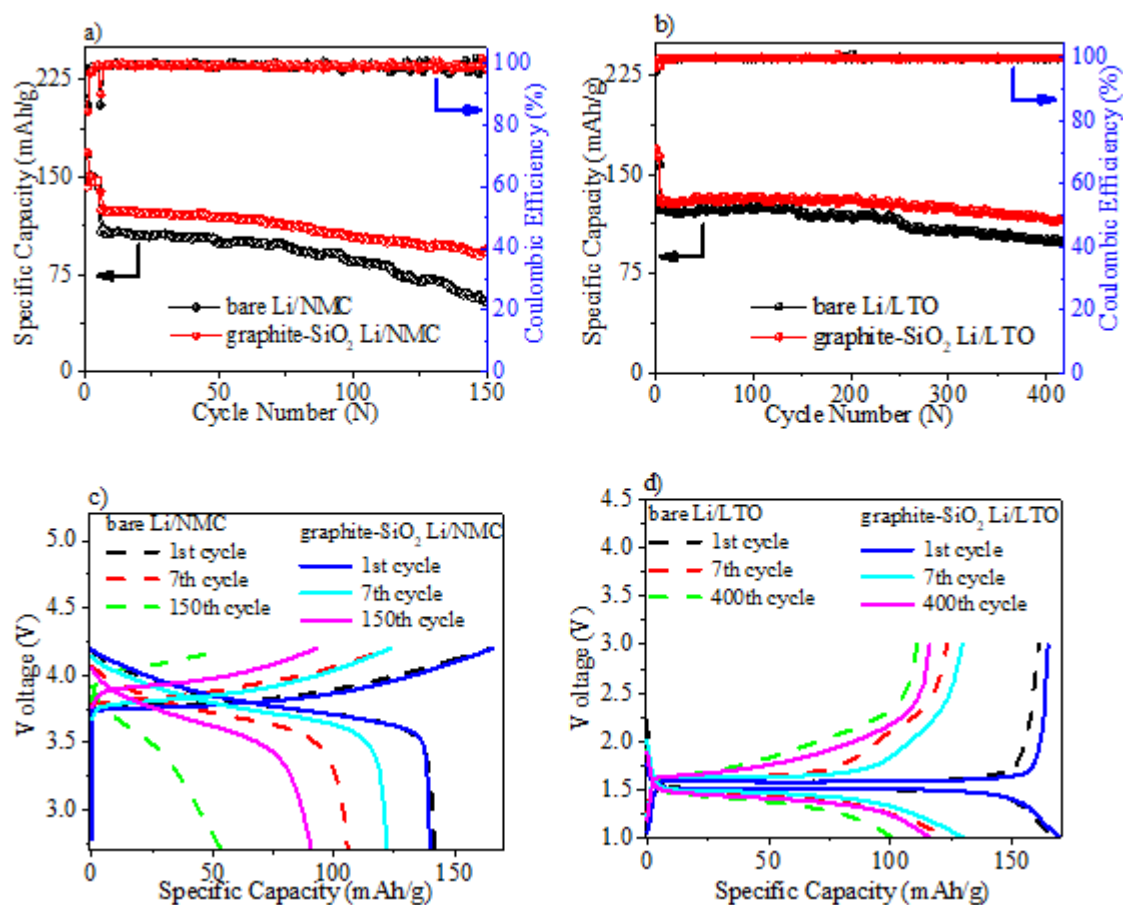


Figure 4. 14: Electrochemical battery cycling performance using bare Li and graphite-SiO₂ Li paired with NMC and LTO cathodes.

The rate capability test was also carried out starting from 0.1 C to 5C and back to 0.1 C using both NMC and LTO cathodes. The battery performance was compared using bare Li and graphite-SiO₂ Li anode. In both the cathodes, higher capacity at higher rates and the high rate capability was observed for graphite-SiO₂ modified Li compared to bare Li. Similarly, the significant reduction in the voltage hysteresis was obtained for graphite-SiO₂ Li anode at higher discharge/charge rates compared to bare Li anode. All the specific capacity values at a specific rate using NMC and LTO cathodes are summarized in Table 4.5 and Table 4.6, respectively.

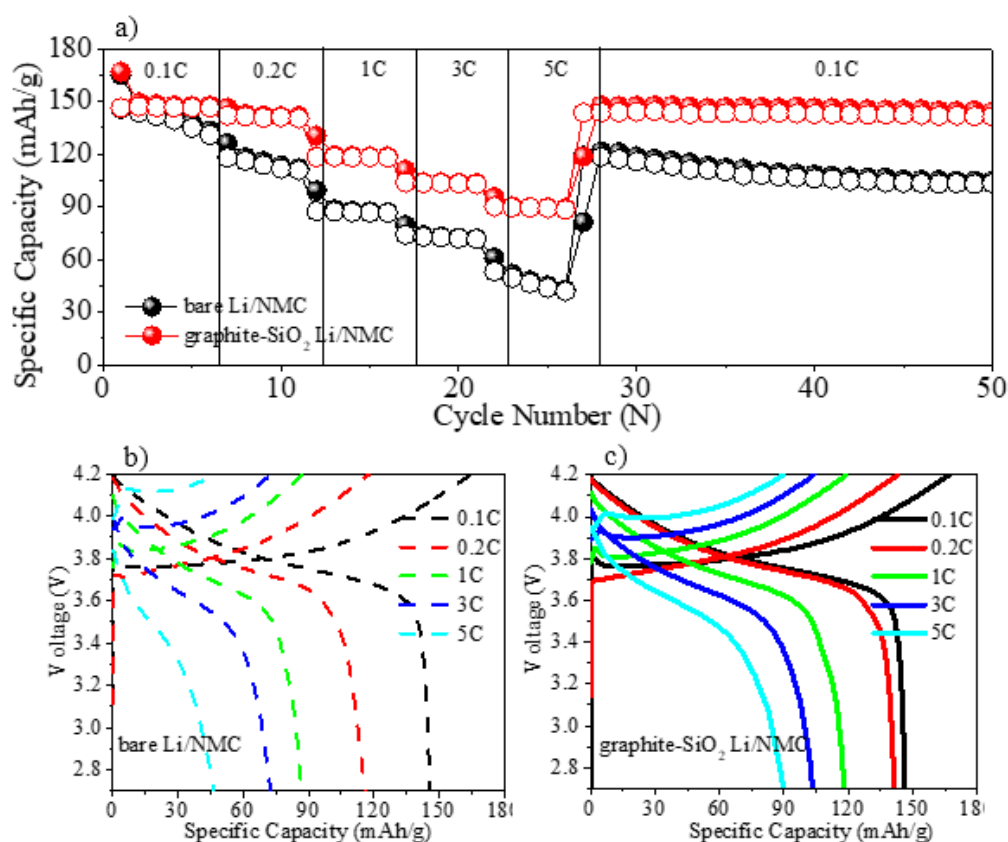


Figure 4. 15: Rate capability test of NMC cathode paired with bare Li and graphite-SiO₂ Li and (b,c) Corresponding charge/discharge voltage curve at a different rate.

Table 4. 5 Charge/discharge capacity of the full cell at different rates using NMC cathode.

Cycle Number	current rate	Charge/discharge capacity (mAh/g)	
		bare Li	Graphite-SiO ₂ Li
2nd	0.1C	146.68/143.58	149.33/147.05
8th	0.2C	118.14/116.11	142.67/141.34
13th	1C	88.46/87.13	119.37/118.38
18th	3C	73.73/72.81	103.87/103.51
23rd	5C	51.85/49.41	90.14/89.61
28th	0.1C	121.35/118.37	147.20/143.77

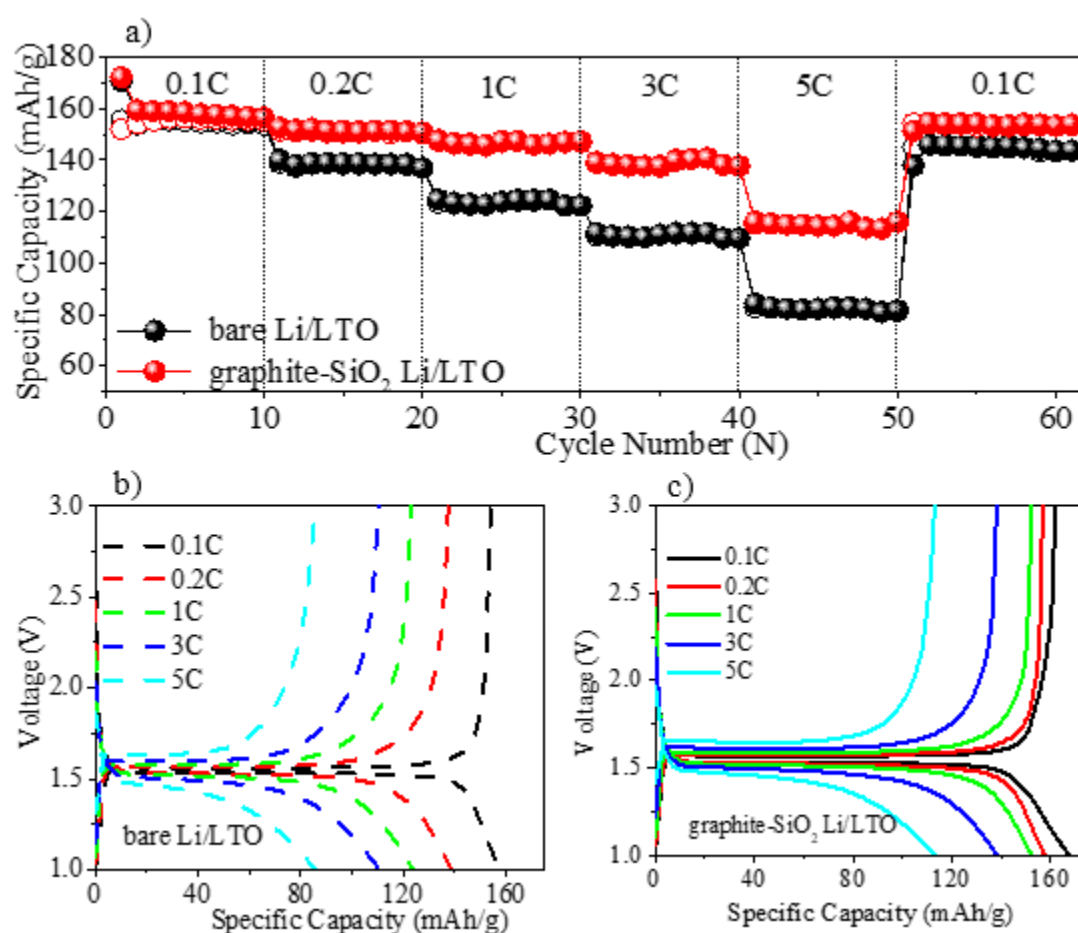


Figure 4. 16: (a) Rate capability test of LTO cathode paired with bare Li and graphite-SiO₂ Li and (b,c) corresponding discharge/charge voltage curve at a different rate

Table 4. 6 Charge/discharge capacity of the full cell at different rates using LTO cathode.

Cycle Number	current rate	Discharge/charge capacity (mAh/g)	
		bare Li	Graphite-SiO ₂ Li
2nd	0.1C	158.08/153.84	159.34/154.21
13th	0.2C	138.85/138.46	152.22/151.48
23th	1C	123.08/122.69	146.29/145.93
33th	3C	110.34/110.00	138.08/137.69
43th	5C	82.26/82.25	114.90/114.90
53th	0.1C	145.93/145.55	154.21/153.84

4.3 Development of *ex-situ* ASEI by a physical deposition method

In this third project, the drop cast method was applied to chemically pretreat the Li metal surface. Different concentration of SnF₂ containing electrolyte was drop cast on the surface of Li metal. Due to the replacement reaction, SnF₂ reacts with the Li metal surface forming electrochemically active Sn, lithium fluoride (LiF), and Li-Sn alloy as SEI components. The concentration of SnF₂ was optimized to be 3 wt% designated as artificially fluorinated hybrid SEI with thickness 25 μm (AFH-25).

4.3.1 Material characterization

Figure 4.17(a) shows the XRD of bare Li protected by Kapton tape. The XRD peaks at $\sim 36^\circ$, 52° , and 65° represent the pure lithium metal. The broad peak at $\sim 20^\circ$ is for the Kapton tape. Figure 4.17(b) shows the XRD of lithium metal after the drop-cast of different weight percentages (wt %) of SnF₂ containing electrolyte. The peaks at $\sim 31.1^\circ$, 32.4° , and 44.1° indicates the presence of Sn, the peaks at $\sim 23.4^\circ$, 27.5° , 40.5° indicates the presence of Li₅Sn₂, and the peaks at $\sim 38.7^\circ$, 44.9° , and 65.4° represents the presence of LiF [49, 114, 151]. XPS was also carried out to investigate the chemical composition of SEI. The presence of peaks at ~ 487.70 eV and ~ 496.01 eV corresponds to Sn. The peak at 55.78 eV for Li and peak at ~ 684.96 eV for F indicates the presence of LiF [98, 111].

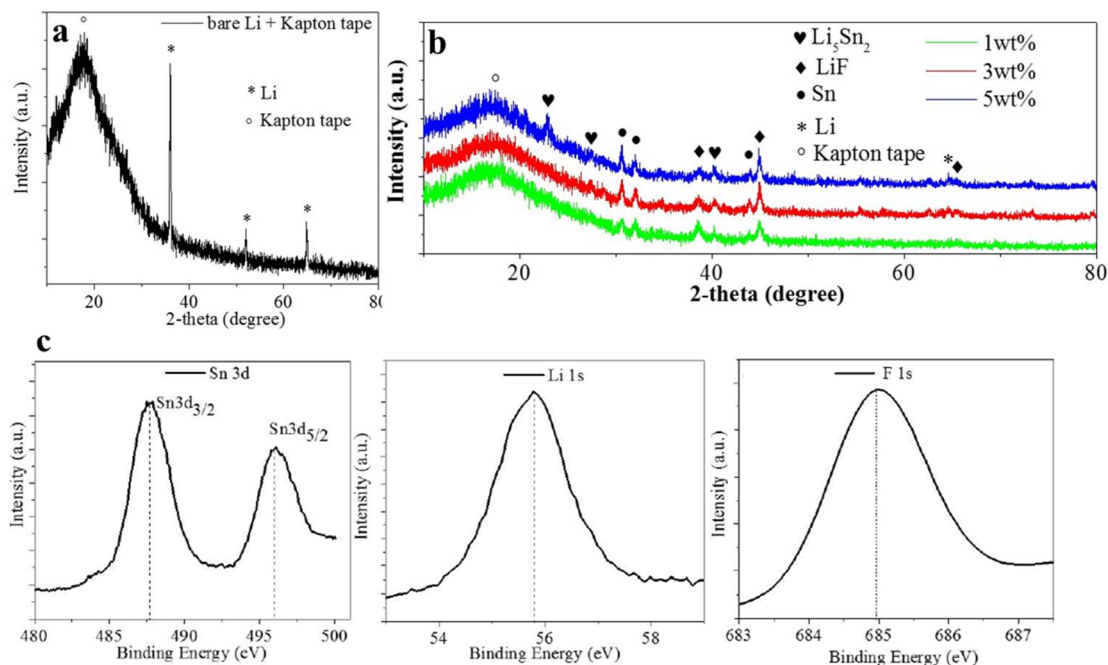


Figure 4. 17: XRD and XPS analysis of pristine Li and after drop cast of SnF_2 .

Figure 4.18a-d shows the photographic images of bare Li and treated with 1, 3, and 5 wt% of SnF_2 and Figure 4.18 e-h shows the corresponding SEM images. The bare Li has a rough surface, 1 wt% SnF_2 treated Li is not fully covered by the artificial SEI and has a lot of pinholes. The electrolyte can penetrate through this pinhole and reaches to the Li underneath the SEI. As a result side reaction occurs, consuming both lithium and electrolyte. Artificial SEI formed by the pretreatment of Li by 3wt% SnF_2 fully covered the lithium and the surface has smooth morphology. Although the lithium metal of Li is fully protected by the pretreatment of 5 wt% SnF_2 , the surface of SEI looks little rough. Figure 4.18i-l shows the cross-sectional SEM images of bare Li and SEI developed on the lithium metal anode. It can be observed that the thickness of SEI developed by pretreating lithium with 1, 3, and 5 wt% SnF_2 is 10, 25, and 55 μm , respectively. The lower thickness may not fully cover the surface of lithium and the higher thickness of SEI leads to sluggish

Li-ion transport. Figure 4.18(m-p) shows the SEM images of bare Li and 1, 3, 5 wt% SnF₂ treated Li after 1st plating at 0.5 mA cm⁻². The bare Li shows the dendritic Li growth which can be due to the inhomogeneous electric field generated by the surface of bare Li metal. In contrast, SnF₂ treated Li shows the uniform Li deposition, where the Li plating/stripping is governed by artificial SEI. The optimized concentration of 3 wt% SnF₂ shows the best Li deposition.

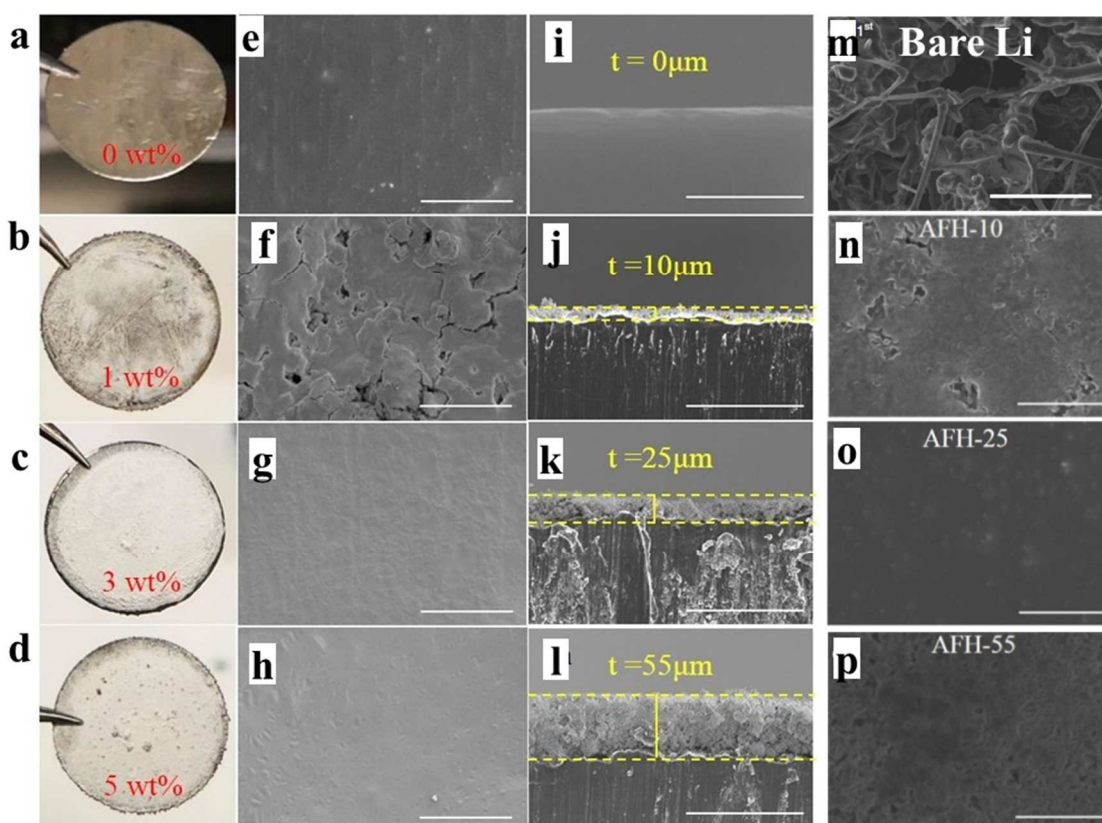


Figure 4. 18: (a-d) Photographic digital images, e-h surface topography SEM images, and (i-l) cross-sectional SEM images of bare Li and surface topography SEM images after 1st plating of Li in bare Li and SnF₂ pretreated Li with different concentrations.

Figure 4.19 shows the AFM measurement of bare Li and AFH-25 Li. The root means square (RMS) value of roughness was measured to be 360 nm for the bare Li and 48 nm

for AFH-25 Li as shown in Figure 4.19(a,b). This indicates that the artificial SEI generated on the Li metal has a smooth and uniform surface which facilitates uniform Li-ion flux. The rough surface on bare Li creates hot spots responsible for the accumulation of Li deposits [152]. Figure 4.19(c,d) shows Young's modulus measurement of bare Li and AFH-25 Li. The AFH-25 Li shows Young's modulus of 55.60 and the bare Li shows Young's modulus of 0.28 GPa. The higher Young's modulus of AFH-25 Li is sufficient enough to suppress the Li dendrite growth. The strong ionic bond between Li and fluorine to form LiF, the high mechanical stability of Sn and Li-Sn alloy contributes to the high Young's modulus of AFH-25.

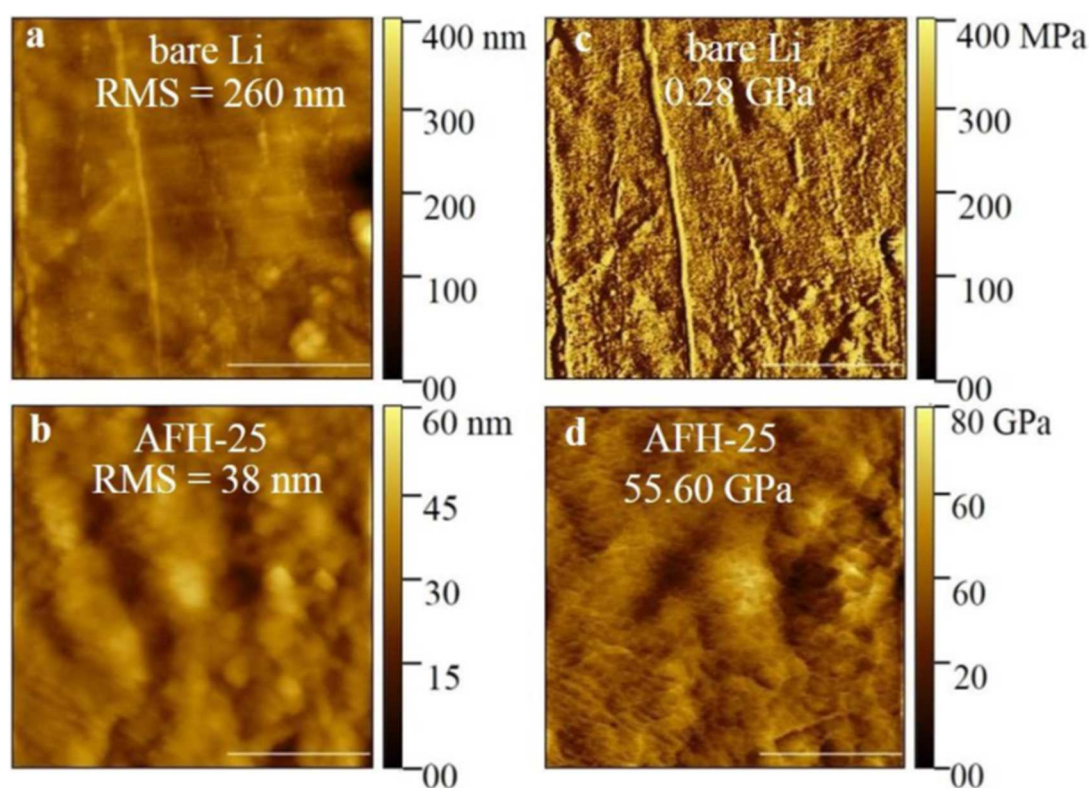


Figure 4. 19: (a,b) AFM measurement of bare Li and AFH-25 and (c,d) corresponding Young's modulus measurement.

To understand the electrodes affinity towards the electrolyte, contact angle measurement was measured. In Figure 4.20(a,b) the bare Li shows the contact angle of $\sim 38^\circ$ and the AFH-25 Li shows the contact angle of $\sim 1^\circ$, indicating the higher surface energy provided by the ASEI. The electrolyte wets all the surface of SEI to facilitate Li-ion transport. The linear sweep voltammetry (LSV) in Figure 4.20(c) shows that AFH-25 has a less steep (slope) than the bare Li indicating the poor electronic conductivity which minimized the flow of electrons and favors the Li deposition underneath the SEI.

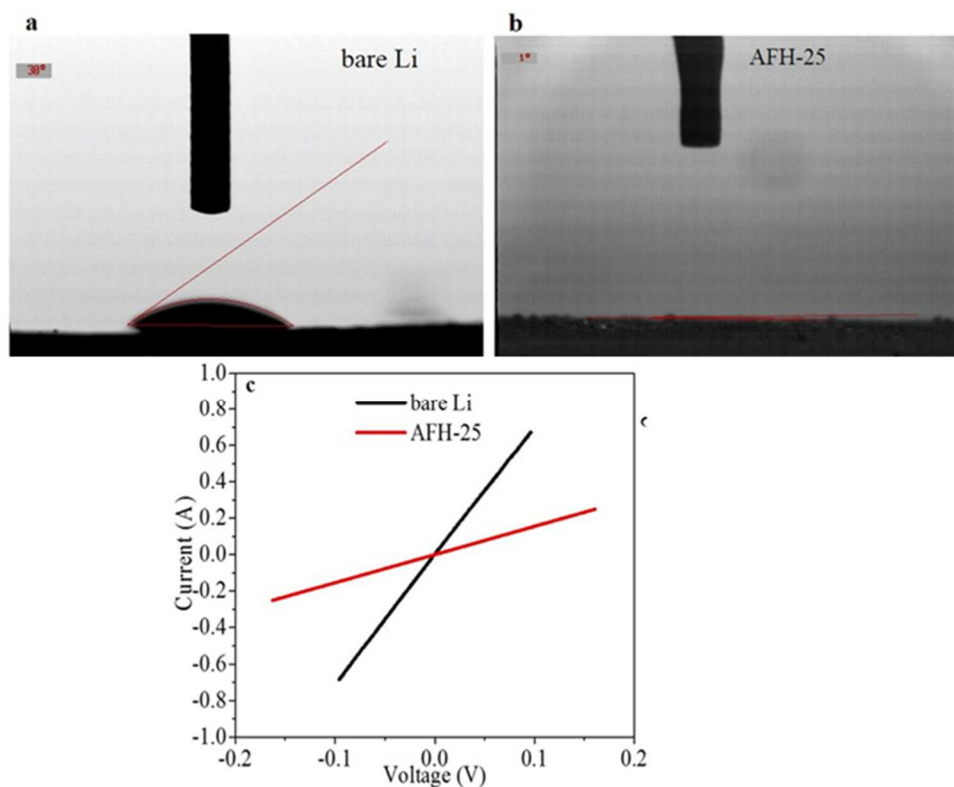


Figure 4. 20: (a,b) Contact angle measurement of bare Li and AFH-25 Li with electrolyte solvent and (c) LSV measurement of bare Li and AFH-Li electrode.

4.3.2 Electrochemical characterization

The symmetrical cell test was carried out to understand the stability of SEI and optimize the SnF_2 concentrations. Figure 4.21(a) shows the Li plating/stripping of bare Li and different wt% SnF_2 treated Li symmetrical. The bare Li symmetrical cell dies in less than 400 hours of plating/stripping with higher voltage hysteresis. In contrast, the SnF_2 treated Li shows better plating/stripping cycles. Among different wt% of SnF_2 , 3 wt% SnF_2 (AFH-25) shows the longest plating/stripping hours more 2300 hours with significantly reduced overpotential. The smooth surface and optimized thickness of 25 μm regulate the uniform Li deposition. The symmetrical cell test with a higher thickness of SEI dies earlier due to the increased impedance of the cell. The lower concentration of SnF_2 may not fully cover or protect the lithium metal.

Figure 4.21(b) shows the Nyquist plot of bare Li and different concentrations of SnF_2 treated Li symmetrical cell at fresh conditions. The bare Li symmetrical cell shows the highest charge transfer resistance of $\sim 400\ \Omega$ and the optimized AFH-25 Li shows the least charge transfer resistance of $\sim 50\ \Omega$. The SnF_2 treated Li shows a double semicircle indicating the extra layer of SEI. The first semicircle in the higher frequency region indicates the impedance of the SEI layer and the second semicircle in the lower frequency region indicates the charge transfer resistance. The bare Li shows a single semicircle as it does not have an additional layer. Figure 4.21(c) and Figure 4.21(d) show the Nyquist plot of bare Li and AFH-25 Li symmetrical cells after the 10th and 50th cycles of plating/stripping. In both cases, the AFH-25 shows lower charge transfer resistance compared to bare Li symmetrical cells, indicating the stable SEI of AFH-25. Figure 4.22

a, b shows the equivalent circuit for fitting the Nyquist plot with two semicircles and one semicircle, respectively.

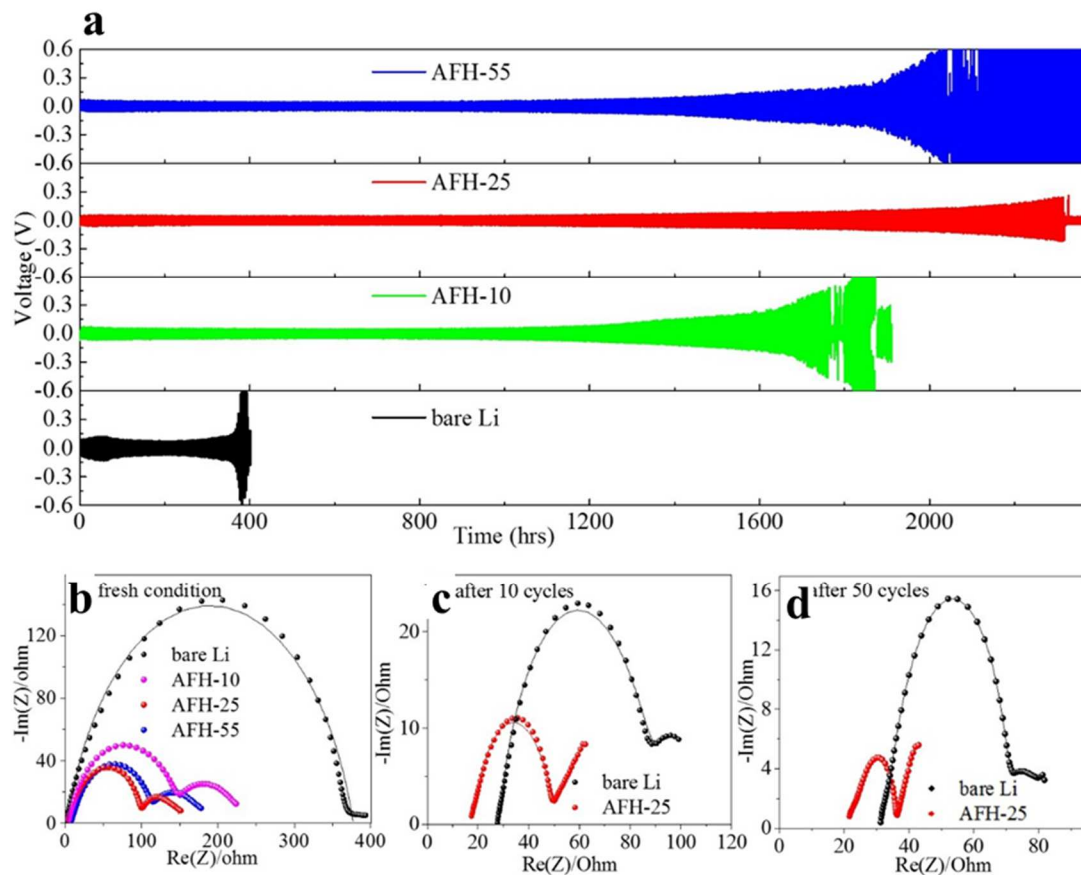


Figure 4. 21: (a) Symmetrical cell test of bare Li, 1, 3, and 5 wt% of SnF_2 treated Li, and (b-d) Nyquist plot of symmetrical cells at fresh condition, after 10th cycle and after 50th cycle of plating/stripping.

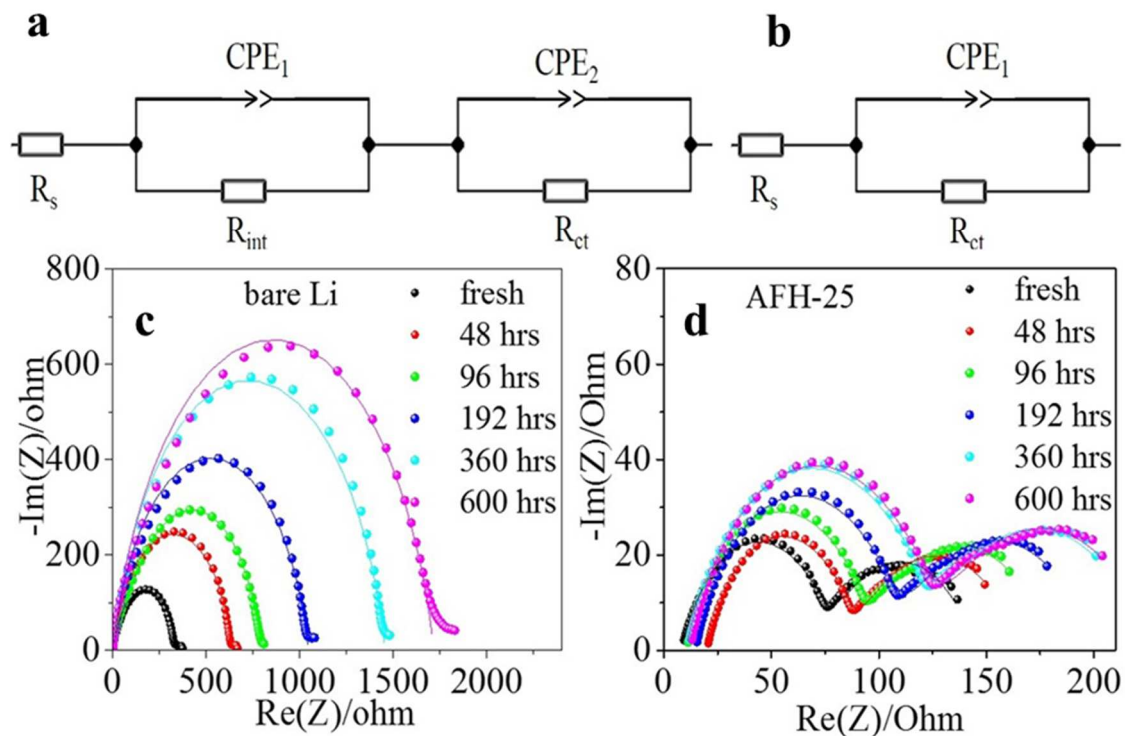


Figure 4. 22: (a,b) Equivalent circuit for fitting the Nyquist plot and Nyquist plot of the symmetrical cell as a function of hours for (c) bare Li and (d) AFH-25 Li.

To further understand the electrochemical stability, the EIS measurement was carried out as a function of hours. In bare Li symmetrical cells, the R_{ct} increases rapidly from $\sim 350 \Omega$ at the fresh condition to more than 1700Ω after 600 hours. This continuous increase in the R_{ct} can be attributed to the continuous side reactions between the hyperactive Li and electrolyte. In contrast, the R_{ct} of AFH-25 symmetrical cell increases in a very slow manner and becomes steady after 360 hours, implying the significant control on the side reaction. The physical barrier provided by the SEI and formation of stabilized SEI with the time helps to minimize the R_{ct} .

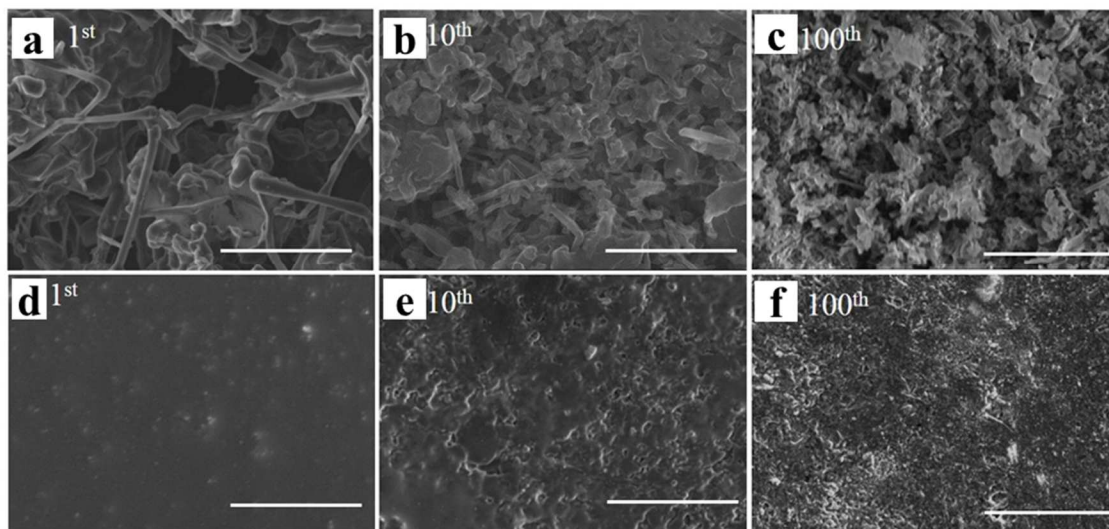


Figure 4. 23: SEM iamges of (a-c) bare Li and (d-f) AFH-25 Li after 1st , 10th and 100th plating.

Figure 4.23a-c shows the SEM images of bare Li after 1st plating, 10th plating, and 100th plating. The formation of dendritic Li growth consumes excess electrolyte and can pierce the separator, challenging the performance and safety concern of the battery. The longer plating/stripping cycles in bare Li can result in the formation of mossy and dead inactive Li, responsible for increasing the cells' impedance. In contrast, Li deposition is regulated by the AFH-25. The uniform and smooth Li deposition can be achieved in 1st, 10th, and even in 100th plating as shown in Figure 4.23(d-f). The synergetic effect of uniformly distributed SEI components governs the uniform Li-ion flux, leading to dendrite-free Li deposition.

For a detailed understanding of the plating/stripping behavior, symmetrical cell tests were carried out at 0.5 mA cm^{-2} and at 1 mA cm^{-2} to achieve a capacity of 1 mAh cm^{-2} as shown in Figure 4.24 (a,b). The longer plating/stripping hours with reduced overpotential was achieved for AFH-25 compared to the bare Li. The lower nucleation overpotential was

achieved for AFH-25 symmetrical cells compared to the bare Li as shown in the inset. At a current density of 0.5 mA cm^{-2} and 1 mA cm^{-2} , the bare Li cell dies at ~ 400 hours and ~ 300 hours, respectively. In contrast, the AFH-Li symmetrical cell shows stable plating/stripping for more than 2300 hours and 800 hours at 0.5 mA cm^{-2} and 1 mA cm^{-2} , respectively. The corresponding voltage hysteresis shows that the lower voltage hysteresis was obtained for AFH-Li symmetrical cell compared to bare Li symmetrical cell. In bare Li symmetrical cell, the voltage hysteresis rises too high more than 600 mV and the cell dies but it is more stable for a longer period of cycles in AFH-25 symmetrical cell.

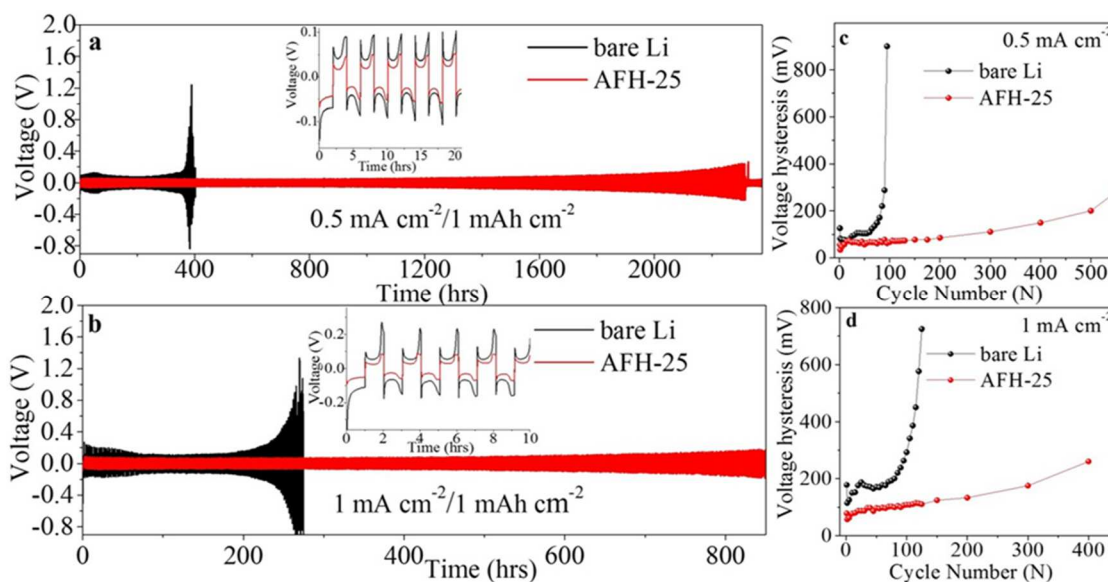


Figure 4. 24: (a,b) Symmetrical cell test of bare Li and AFH-25: Inset shows the first five plating/stripping cycles, and (c,d) corresponding voltage hysteresis.

The symmetrical cell tests were carried out at constant current densities and capacities such as $2 \text{ mA cm}^{-2}/2\text{mAh cm}^{-2}$, $2 \text{ mA cm}^{-2}/2\text{mAh cm}^{-2}$, and $5 \text{ mA cm}^{-2}/1\text{mAh cm}^{-2}$ as shown in Figure 4.25a-c. In all the cases, AFH-25 symmetrical cells improved symmetrical cell performance.

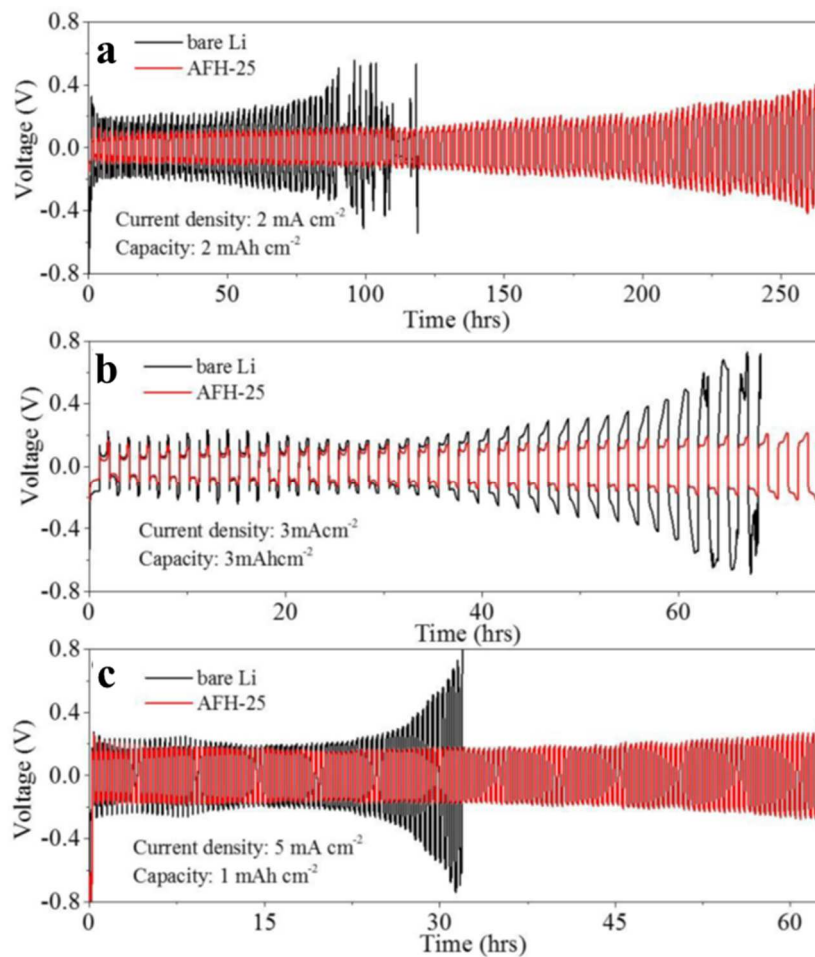


Figure 4. 25: Symmetrical cell tests at various current densities and capacities.

The bare Li and AFH-25 symmetrical cells were tested at various current densities from 1 to 5 mA cm⁻² and fixed areal capacity to 1 mAh cm⁻² for each current density. It was found that the AFH-15 cell shows stable plating/stripping with lower voltage overpotential compared to the bare Li symmetrical cell as shown in Figure 4.26a,b.

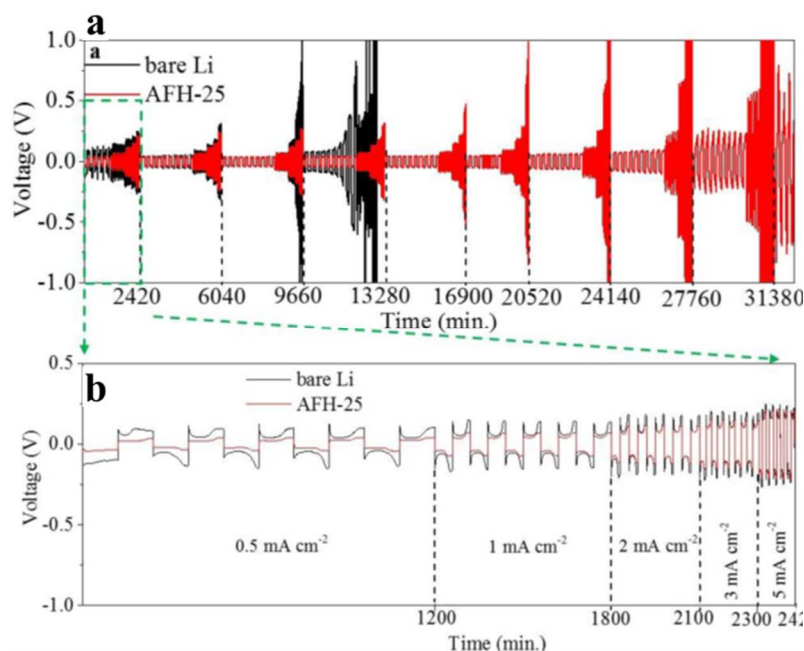


Figure 4. 26: (a) Symmetrical cell test at various current densities from 0.5 to 5 mA cm⁻² to achieve a constant capacity of 1 mAh cm⁻² and (b) The zoomed plating /stripping in the beginning hours.

Figure 4.27 shows the CV measurement of bare Li symmetrical cell and AFH-25 symmetrical cell. The bare Li symmetrical cell shows a straight line as shown in Figure 4.27(a), implying the Li plating/stripping mechanism. In contrast, the AFH-25 symmetrical cell shows the redox peaks at ~ 0.12 V as shown in Figure 4.27(b), indicating the redox reaction. The lithiation and delithiation of electrochemically active Sn in the SEI contributed to the storage of Li. Thus the hybrid SEI stores Li by both Li plating and Li-Sn alloy formation. As a result excess, Li can be stored and the uniform Li deposition can be expected even at higher current density. The straight line and reversible alloy/dealloy formation improve the electrochemical symmetrical and full cell battery performance.

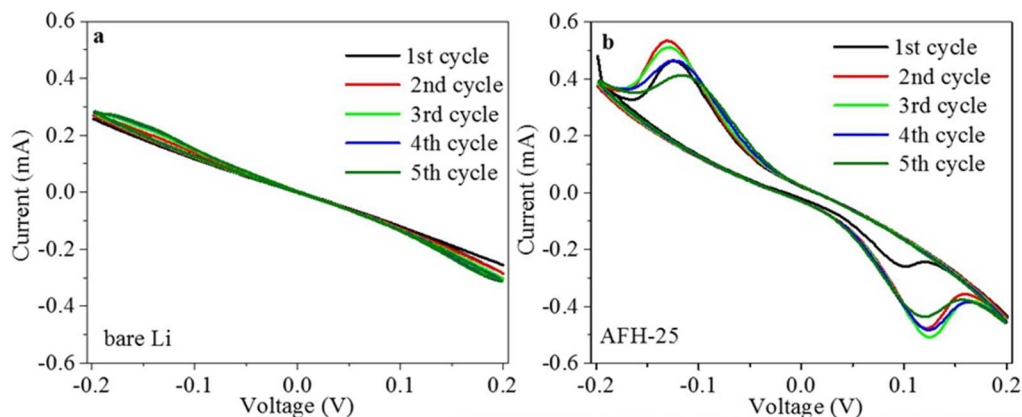


Figure 4.27: CV measurement of (a) bare Li and (b) AFH-25 symmetrical cells.

Figure 4.28 shows the cross-sectional SEM images of bare Li and AFH-25 electrode after 100 the cycle of Li plating/stripping in symmetrical cells. It can be observed in Figure 4.28(a) that the bare Li electrode has a thickness of 120 μm Li deposition. This can be attributed to irreversible Li deposition. The higher thickness of Li deposition increases the cell's impedance and leads to sluggish Li-ion transport. From Figure 4.28(b), it can be observed that in the AFH-25 electrode the thickness of Li deposition is only 60 μm including the 25 μm thick ASEI. The thin Li deposition indicates the reversible Li plating and reversible alloy/dealloy formation. As a result, the consumption of Li and electrolyte can be effectively controlled.

Figure 4.29(a) shows the electrochemical full cell cycling performance using NMC111 cathode when paired with bare Li and AFH-25 Li anode. The AFH-25 Li anode shows the 1st CE of $\sim 83\%$. Besides, AFH-25 Li anode demonstrated capacity retention of $\sim 80\%$ with $\sim 105 \text{ mAh g}^{-1}$ specific capacity at the 150th cycle compared to the stabilized specific capacity at the 3rd cycle. In contrast, bare Li anode shows the 1st CE of $\sim 81\%$. Besides, the

bare Li anode demonstrated capacity retention of $\sim 60\%$ with $\sim 80 \text{ mAh g}^{-1}$ specific capacity at the 150th cycle compared to the stabilized specific capacity at the 3rd cycle.

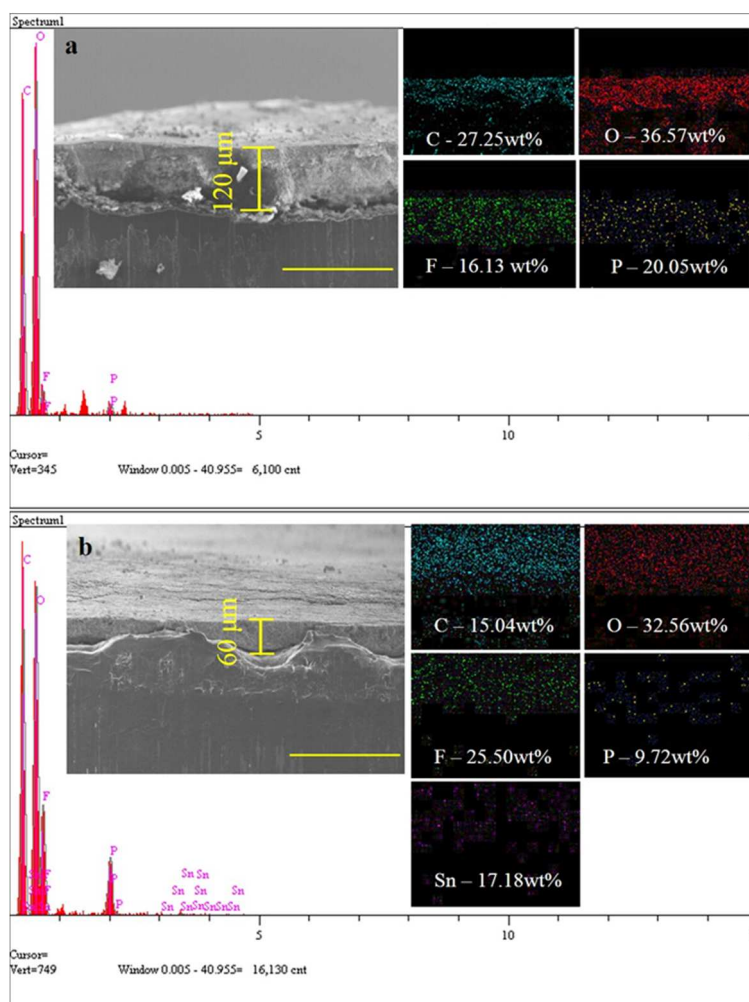


Figure 4. 28: (a,b) Cross-sectional SEM images and corresponding elemental mapping after 100 cycles of plating/stripping in bare Li and AFH-25 Li symmetrical cell.

Figure 4.29(b,c) shows the voltage profile of bare Li/NMC and AFH-Li/NMC full cell at the beginning 3rd cycle and 150th cycle. It can be observed that the voltage profile overlaps in the beginning cycles. However, the voltage overpotential increases in bare Li/NMC compared to AFH-Li/NMC full cell at a higher cycle (150th cycle). This indicates the effective approach of reviving lithium metal anode by the pretreatment with SnF_2 .

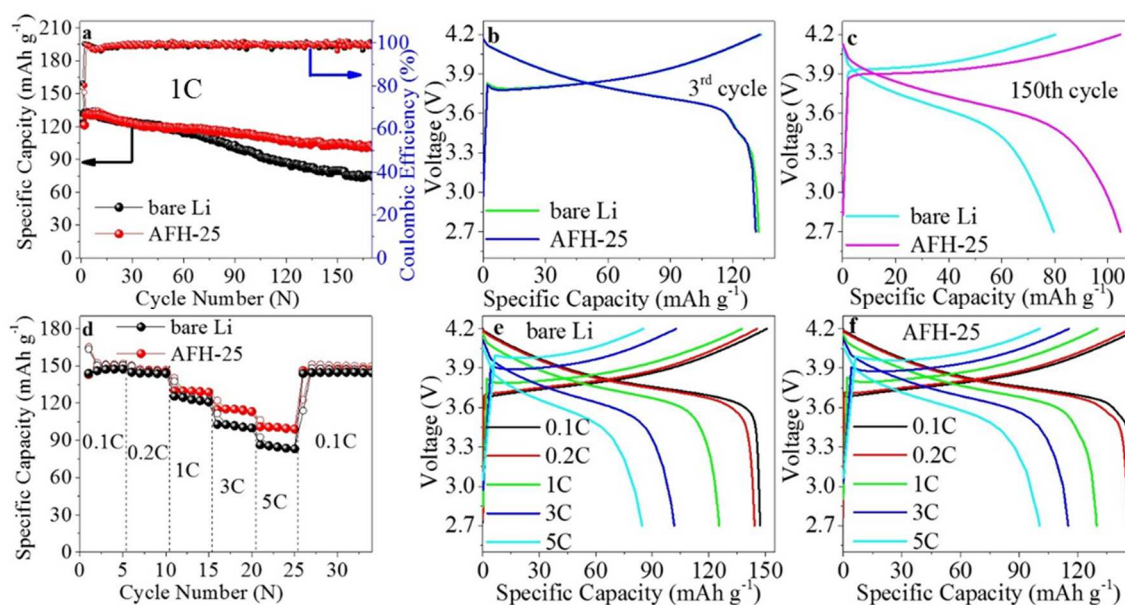


Figure 4. 29: (a-c) Full cell battery performance at a constant rate and corresponding voltage profiles and (d-f) Full cell battery performance at a different rate and corresponding voltage profiles.

Figure 4.29(d) shows the rate capability test using bare Li and AFH-25 Li anode coupled with NMC111 cathode. It can be observed that the AFH-25 Li/NMC full cell showed a higher capacity at a higher current density rate compared to the bare Li/NMC full cell. At 5 C, the AFH-Li/NMC full cell showed a charge /discharge capacity of $\sim 100/100$ mAh g⁻¹, and the bare Li/NMC full cell showed $\sim 85/84$ mAh g⁻¹. The stabilized SEI in AFH-Li allows fast Li-ion transport even at a higher current density rate. Similarly, the improved voltage profile with lower voltage overpotential was achieved with AFH-25 Li/NMC compared to the bare Li/NMC full cell. The full cell test results are in good agreement with the symmetrical cell test. The synergetic effect of SEI components enhanced electrochemical battery performance.

CHAPTER 5: SUMMARY AND CONCLUSIONS

5.1 Summary

Lithium metal batteries are considered as a promising next-generation energy storage devices to drive high energy-requiring battery applications in consumer and industrial applications. Lithium metal anode is the key factor for aiming the energy density of 500 Wh kg⁻¹ at the cell level. The inherent problems such as infinite volume expansion issues and the hyperactive nature of lithium limit its commercialization. The lithium batteries with high performance, safety, and low cost can balance the standard way of living and green environment. Thus, it is highly recommended addressing the issues of lithium metal batteries such as the formation of unstable SEI and lithium dendrite growth. Besides, the use of lean electrolyte, high mass loading cathode, lean lithium, and optimization of other cell components such as separator, and spring can substantially increase the energy density of the batteries. The practical pathways for achieving the high energy densities under harsh conditions such as a low ratio of the anode to cathode capacity ($N/P < 2$), and the lean electrolyte of $< 3 \text{ g (Ah)}^{-1}$ at fast charging rates is very challenging. The in-depth understanding of the SEI formation mechanism and electrode stability during the charge/discharge process by the advanced state-of-art characterization tools is essential [51, 84, 89, 101, 153-175]. The synchrotron X-ray analytical techniques, cryogenic electron microscopy, XPS, time of flight secondary ion mass spectrometry (TOF-SIMS), Fourier transform infrared spectroscopy (FTIR), atomic force microscopy (AFM), transmission electron microscopy (TEM), cryo-TEM, enhanced Raman spectroscopy, auger electron spectroscopy (AES) are being widely deployed in better understanding the lithium metal batteries. Besides, simulation techniques [40-44, 176-179] such as the finite

Peled model, Mosaic model, coulombic interaction mechanism model, element method, phase field theory, molecular dynamics, first-principle density functional theory are also equally investigated.

Various methods have been established for reviving the lithium metal anode. Among them, the development of solid-state electrolyte is considered a promising strategy to replace flammable liquid electrolyte, but is still in its infancy period, owing to its challenges such as low li-ion conductivity and interface instabilities. The development of Li host is considered a significant technique to provide sufficient space for Li expansion issues and confine the Li dendrites. However, the use of excess Li host increase the total mass of the battery, and further modifications such as optimization of porosity, and lithiophilic coating are required to suppress the Li dendrite growth. The formation of *in-situ* artificial solid electrolyte interphase can suppress the Li dendrite growth but consume both Li and electrolyte during the battery operation. Recently, the engineering the *ex-situ* artificial SEI by physical and chemical deposition method has attracted great attention in addressing the inherent issues of lithium metal anode. The physical deposition on the surface of Li metal with sufficient control on the distribution, thickness, and mechanical/electrochemical stability can render the uniform Li-ion flux and regulates the uniform Li deposition. Besides physical coating, interlayer between the lithium metal and liquid electrolyte are also widely investigated in protecting the lithium metal anode. Such interlayers are supposed to have a sufficient Li-ion diffusion coefficient. The chemical surface treatment of lithium could provide the high anchorage affinity of the formed SEI with Li metal anode. Although various strategies of developing the *ex-situ* ASEI has been investigated, an ideal SEI with high Young's modulus, excellent Li-ion conductivity, electrochemical &

mechanical stability, high flexibility, high mechanical stability, or strong anchorage affinity to the lithium metal can only revive the lithium metal for significant improvement in LMBs. The poor electronic conductivity of ASEI also inhibits the flow of electrons, resulting in the suppression of Li dendrite growth. Recently, mixed ionic conductors are also widely used as ASEI where the synergetic effect of both Li-ion conductors and electronic conductors play a significant role in uniform Li deposition. The electronic conductors such as Cu and Ti in SEI has the ability of surface storage or grain boundary capture ability. Other electronic conductors such as Sn, Zn, Ag, and Au can store Li by alloy formation. The ionic conductors allow sufficient Li-ion diffusion bath for capturing the Li-ions. The development of ASEI with high flexibility can buffer the volume expansion issues during Li plating/stripping cycles.

5.2 Conclusions

In the first project, reduced WO_3 (R- WO_3) was successfully prepared by the incorporation of urea in pristine WO_3 (P- WO_3) and annealing at 500°C for two hours under the N_2 environment. The R- WO_3 anode material facilitates faster electron-transfer kinetics and leads to improved electrochemical battery performance. The outcome reveals the unique self-recovery of the specific capacity with $\sim 193\%$, 179% , and 166% in R- WO_3 compared to the preceding discharge specific capacity at 15th, 36th, and 45th cycles. The observed discharge/charge specific capacity was $\sim 521/457$, $\sim 538/536$, and $\sim 555/555\text{ mAh g}^{-1}$ at those respective cycles. R- WO_3 exhibits the first discharge capacity of $\sim 959\text{ mAh g}^{-1}$ and still maintains as high as 558 mAh g^{-1} at the 100th cycle. In contrast, P- WO_3 demonstrated a quick discharge capacity loss from 670 mAh g^{-1} at the 1st cycle to 236 mAh g^{-1} at the 100th cycle. Besides, at different current density rates starting from 35 mA g^{-1} to 280 mA

g^{-1} and back to 35 mA g^{-1} , R- WO_3 showed a superior rate capability of $\sim 94\%$ when the capacity at 22^{nd} was compared to the capacity at the 2^{nd} cycle. In contrast, P- WO_3 showed a rate capability of only $\sim 88\%$. The excellent electrochemical reversibility and cycling stability in R- WO_3 can be attributed to the higher surface area (smaller particle size), lower charge transfer resistance (lower bandgap), and oxygen vacancies in R- WO_3 compared to P- WO_3 . Moreover, the presence of defects reactivates with cycling to obtain the self-recovery of capacity.

In the second project, the *ex-situ* SEI was developed successfully by the physical deposition method. Here, in this project, we used R-F sputtering to deposit the ultrathin bilayer of graphite and SiO_2 on top of the lithium metal anode. The symmetrical cell test and full cell test were compared between the bare Li anode and graphite- SiO_2 deposited Li anode. At a current density of 0.5 mA cm^{-2} , the bare Li symmetrical cell dies at ~ 350 hours and shows the dendritic Li deposition. In contrast, the graphite- SiO_2 Li symmetrical lasts for more than 1200 hours and exhibited dendrite-free uniform Li deposition at a current density of 0.5 mA cm^{-2} . Besides, in full cell test, the bare Li anode showed 1^{st} CE of $\sim 86\%$ (NMC cathode) and $\sim 84\%$ (LTO cathode). The bare Li/NMC full cell showed capacity retention of $\sim 50\%$ at the 150^{th} cycle ($\sim 54 \text{ mAh g}^{-1}$) and bare Li/LTO full cell showed capacity retention of $\sim 80\%$ at the 400^{th} cycle (charge capacity of $\sim 100 \text{ mAh g}^{-1}$). In contrast, graphite- SiO_2 Li/NMC full cell showed capacity retention of $\sim 74\%$ at the 150^{th} cycle ($\sim 125 \text{ mAh g}^{-1}$) and graphite- SiO_2 Li/LTO full cell showed capacity retention of $\sim 88\%$ at the 400^{th} cycle (charge capacity of $\sim 132 \text{ mAh g}^{-1}$). Moreover, in the rate capability test under different current rates, the bare Li/NMC full cell showed capacity retention of $\sim 83\%$ at the 28^{th} cycle and the bare Li/LTO full cell showed capacity retention of $\sim 92\%$ at the 53^{rd}

cycle. In contrast, in the rate capability test under different current rates, the graphite-SiO₂ Li/NMC full cell showed capacity retention of ~ 96% at the 28th cycle and the graphite-SiO₂ Li/LTO full cell showed capacity retention of ~ 97% at the 53rd cycle. This significant outstanding electrochemical performance with the use of *ex-situ* based graphite-SiO₂ bilayer SEI can be attributed to the synergetic effect of graphite and SiO₂. The graphite is electronically conductivity which acts as a bridge to electrically connect the plated Li with the bulk Li electrode. Besides, the graphite offers flexibility to afford the volume expansion of Li during plating/stripping cycles. Similarly, SiO₂ provides sufficient Li-ion conductivity and prevents the electron flow. Besides, SiO₂ has a higher electrolyte affinity for fast Li-ion transport and high enough Young's modulus to suppress the growth of Li dendrites. Moreover, the amorphous SiO₂ stores' excess Li by the formation of Li-Si alloy.

In the third project, the *ex-situ* SEI was developed successfully by the chemical deposition method. Here, in this project, we used a drop cast method to generate the artificial SEI on top of the lithium metal anode. Tin fluoride (SnF₂) containing electrolyte was drop-casted on the surface of lithium metal. The replacement reaction occurs between the hyperactive lithium metal and SnF₂ to form LiF, electrochemically active Sn, and Li-Sn alloy as SEI components. At a current density of 0.5 mA cm⁻², the bare Li symmetrical cell dies at ~ 350 hours and shows the dendritic Li deposition. In contrast, the artificially fluorinated hybrid SEI with 25 μm thickness (AFH-25) Li symmetrical lasts for more than 2300 hours and exhibited dendrite-free uniform Li deposition at a current density of 0.5 mA cm⁻². Besides, in the full cell test, the bare Li/NMC full cell showed 1st CE of ~ 81% but AFH-25 Li/NMC showed 1st CE of 83%. The bare Li/NMC full cell showed capacity retention of ~ 60% at the 150th cycle (~79 mAh g⁻¹). In contrast, AH-25 Li/NMC full cell showed

capacity retention of $\sim 80\%$ at the 150th cycle ($\sim 105 \text{ mAh g}^{-1}$). Moreover, in the rate capability test under different current rates, the AFH-25 Li/NMC full cell showed excellent capacity retention compared to the bare Li/NMC full cell. At a higher rate of 5C, AFH-25/NMC full cell exhibited a specific charge/discharge capacity of 100.54/100.44 mAh g^{-1} which is significantly higher than that of bare Li/NMC full cell (85.29/84.60 mAh g^{-1}). The outstanding electrochemical cycling performance and dendrite free Li deposition was achieved with AFH-25 SEI Li anode. This can be attributed to the synergetic effect of SEI components (LiF, Sn Sn-Li alloy). The higher electrolyte affinity, the higher Young's modulus, and the higher transference number of the AFH-25 SEI facilitate fast Li-ion transport and suppression of Li dendrite growth. The higher Li-ionic conductivity and poor electronic conductivity of LiF, the ability of electrochemically active Sn to store Li by alloy formation, and the ability of Li-Sn alloy to stabilize the interface contributed to the stabilized SEI, dendrite-free Li deposition, and improved battery performance.

5.3 Future Work

For project 1, the technique of creating oxygen vacancies that we used in WO_3 to improve the charge transport dynamics.

- (1) This technique can also be applied to other transitional metal oxides such as MoO_3 which has higher theoretical capacity. This will help to improve the reversibility and cycling stability of high capacity anode materials.
- (2) The TMOs can be annealed under vacuum without the incorporation of chemicals to study the oxygen vacancy. This will lower the preparation cost.
- (3) The materials which can reduce into H_2 can be incorporated with TMOs which ultimately reduces the TMOs.

For projects 2 and 3, the technique of developing SEI by physical deposition and chemical deposition was used to modify the lithium metal surface.

- (1) The use of similar organic/inorganic bilayer can be applied using different organic and inorganic materials. The organic layer provides the flexibility and the inorganic layer can provide the high Young's modulus.
- (2) The heterogeneous structure bilayer or trilayer with different properties such as Li-ion conductivity and electronic property can also be utilized to benefit from the synergetic effect of each layer.
- (3) The various gas or solution which can react with lithium can be used to develop the SEI. The different sources of gases such as N_2 , carbon, and fluorine can be utilized to pretreat the lithium metal surface.
- (4) The elements similar to Sn which can make an alloy with Li can be used to pretreat the lithium metal.
- (5) The development of such ex-situ SEI can also be applied to the top of 3D metal-based, carbon-based, and other polymer-based Li hosts.
- (6) Engineering of the interfacial layer similar to our approach could provide a pathway for the rapid integration of SSE in lithium metal batteries. The development of an artificial layer not only protects the lithium metal but also improve the performance of solid-state electrolyte.

References

- [1] G. Zheng, "Beyond Lithium Ion: Developing High Energy Density Lithium Sulfur Batteries," Stanford University, 2014.
- [2] T. Trigg *et al.*, "Global EV outlook: understanding the electric vehicle landscape to 2020," *Int. Energy Agency*, vol. 1, pp. 1-40, 2013.
- [3] *Today in Energy. International Energy Outlook. Jan 13, 2020.*
Available: <https://www.eia.gov/todayinenergy/detail.php?id=42342>
- [4] E. Adhamash, R. Pathak, Q. Qiao, Y. Zhou, and R. McTaggart, "Gamma-radiated biochar carbon for improved supercapacitor performance," *RSC Advances*, vol. 10, no. 50, pp. 29910-29917, 2020.
- [5] R. Pathak, K. Chen, Y. Zhou, and Q. Qiao, "Advances in Conversion-Type Li-Metal Fluoride Battery: A Mini-Review," 2019.
- [6] Z. Zhao, R. Pathak, X. Wang, Z. Yang, H. Li, and Q. Qiao, "Sulfiphilic FeP/rGO as a highly efficient sulfur host for propelling redox kinetics toward stable lithium-sulfur battery," *Electrochimica Acta*, p. 137117, 2020.
- [7] E. Adhamash *et al.*, "High-Energy Plasma Activation of Renewable Carbon for Enhanced Capacitive Performance of Supercapacitor Electrode," *Electrochimica Acta*, p. 137148, 2020.

- [8] M. S. Whittingham, "Electrical energy storage and intercalation chemistry," *Science*, vol. 192, no. 4244, pp. 1126-1127, 1976.
- [9] A. Yoshino, "The birth of the lithium-ion battery," *Angewandte Chemie International Edition*, vol. 51, no. 24, pp. 5798-5800, 2012.
- [10] A. Manthiram, "A reflection on lithium-ion battery cathode chemistry," *Nature Communications*, vol. 11, no. 1, pp. 1-9, 2020.
- [11] D. Lin, Y. Liu, and Y. Cui, "Reviving the lithium metal anode for high-energy batteries," *Nature nanotechnology*, vol. 12, no. 3, p. 194, 2017.
- [12] J. Liu *et al.*, "Pathways for practical high-energy long-cycling lithium metal batteries," *Nature Energy*, vol. 4, no. 3, pp. 180-186, 2019.
- [13] Y.-P. Wu, C. Jiang, C. Wan, and R. Holze, "Anode materials for lithium ion batteries by oxidative treatment of common natural graphite," *Solid State Ionics*, vol. 156, no. 3, pp. 283-290, 2003.
- [14] C. K. Chan *et al.*, "High-performance lithium battery anodes using silicon nanowires," *Nature nanotechnology*, vol. 3, no. 1, pp. 31-35, 2008.
- [15] A. Gurung *et al.*, "Tin selenide–multi-walled carbon nanotubes hybrid anodes for high performance lithium-ion batteries," *Electrochimica Acta*, vol. 211, pp. 720-725, 2016.

- [16] P.-L. Taberna, S. Mitra, P. Poizot, P. Simon, and J.-M. Tarascon, "High rate capabilities Fe₃O₄-based Cu nano-architected electrodes for lithium-ion battery applications," *Nature materials*, vol. 5, no. 7, pp. 567-573, 2006.
- [17] M. S. Park, G. X. Wang, Y. M. Kang, D. Wexler, S. X. Dou, and H. K. Liu, "Preparation and Electrochemical Properties of SnO₂ Nanowires for Application in Lithium-Ion Batteries," *Angewandte Chemie*, vol. 119, no. 5, pp. 764-767, 2007.
- [18] M. F. Hassan, Z. Guo, Z. Chen, and H.-K. Liu, "Carbon-coated MoO₃ nanobelts as anode materials for lithium-ion batteries," *Journal of Power Sources*, vol. 195, no. 8, pp. 2372-2376, 2010.
- [19] B. Varghese *et al.*, "Fabrication of NiO nanowall electrodes for high performance lithium ion battery," *Chemistry of Materials*, vol. 20, no. 10, pp. 3360-3367, 2008.
- [20] G. Wang, J. Liu, S. Tang, H. Li, and D. Cao, "Cobalt oxide-graphene nanocomposite as anode materials for lithium-ion batteries," *Journal of Solid State Electrochemistry*, vol. 15, no. 11-12, pp. 2587-2592, 2011.
- [21] F. Liu, J. G. Kim, C. W. Lee, and J. S. Im, "A mesoporous WO₃-X/graphene composite as a high-performance Li-ion battery anode," *Applied Surface Science*, vol. 316, pp. 604-609, 2014.

- [22] R. Pathak *et al.*, "Capacity Revival of Tungsten trioxide Anode Material in Lithium-Ion Battery," in *2019 IEEE International Conference on Electro Information Technology (EIT)*, 2019, pp. 1-5: IEEE.
- [23] K. Chen *et al.*, "SnO₂ Nanoparticles Embedded Biochar as Anode Material in Lithium Ion Batteries," in *2019 IEEE International Conference on Electro Information Technology (EIT)*, 2019, pp. 1-4: IEEE.
- [24] P. Poizot, S. Laruelle, S. Grugeon, L. Dupont, and J. Tarascon, "Nano-sized transition-metal oxides as negative-electrode materials for lithium-ion batteries," *Nature*, vol. 407, no. 6803, pp. 496-499, 2000.
- [25] S. A. Pervez, D. Kim, C.-H. Doh, U. Farooq, H.-Y. Choi, and J.-H. Choi, "Anodic WO₃ mesosponge@ carbon: A novel binder-less electrode for advanced energy storage devices," *ACS applied materials & interfaces*, vol. 7, no. 14, pp. 7635-7643, 2015.
- [26] K. Huang and Q. Zhang, "Rechargeable lithium battery based on a single hexagonal tungsten trioxide nanowire," *Nano Energy*, vol. 1, no. 1, pp. 172-175, 2012.
- [27] Y. Qiu, G.-L. Xu, Q. Kuang, S.-G. Sun, and S. Yang, "Hierarchical WO₃ flowers comprising porous single-crystalline nanoplates show

- enhanced lithium storage and photocatalysis," *Nano research*, vol. 5, no. 11, pp. 826-832, 2012.
- [28] Y. Liu, Y. Jiao, H. Zhou, X. Yu, F. Qu, and X. Wu, "Rational design of WO₃ nanostructures as the anode materials for lithium-Ion batteries with enhanced electrochemical performance," *Nano-Micro Letters*, vol. 7, no. 1, pp. 12-16, 2015.
- [29] W.-J. Li and Z.-W. Fu, "Nanostructured WO₃ thin film as a new anode material for lithium-ion batteries," *Applied Surface Science*, vol. 256, no. 8, pp. 2447-2452, 2010.
- [30] X.-Y. Xue, B. He, S. Yuan, L.-L. Xing, Z.-H. Chen, and C.-h. Ma, "SnO₂/WO₃ core-shell nanorods and their high reversible capacity as lithium-ion battery anodes," *Nanotechnology*, vol. 22, no. 39, p. 395702, 2011.
- [31] J. Yang *et al.*, "Facile preparation and electrochemical properties of hierarchical chrysanthemum-like WO₃·0.33 H₂O," *Journal of Materials Chemistry*, vol. 22, no. 9, pp. 3699-3701, 2012.
- [32] A. Santhosha, S. K. Das, and A. J. Bhattacharyya, "Tungsten Trioxide (WO₃) Nanoparticles as a New Anode Material for Sodium-Ion Batteries," *Journal of Nanoscience and Nanotechnology*, vol. 16, no. 4, pp. 4131-4135, 2016.

- [33] C. Lian *et al.*, "Preparation of hexagonal ultrathin WO₃ nano-ribbons and their electrochemical performance as an anode material in lithium ion batteries," *Nano Research*, vol. 9, no. 2, pp. 435-441, 2016.
- [34] R. Pathak, Y. Zhou, and Q. Qiao, "Recent Advances in Lithiophilic Porous Framework toward Dendrite-Free Lithium Metal Anode," *Applied Sciences*, vol. 10, no. 12, p. 4185, 2020.
- [35] K. Chen *et al.*, "A copper-clad lithiophilic current collector for dendrite-free lithium metal anodes," *Journal of Materials Chemistry A*, vol. 8, no. 4, pp. 1911-1919, 2020.
- [36] A. Gurung *et al.*, "A review on strategies addressing interface incompatibilities in inorganic all-solid-state lithium batteries," *Sustainable Energy & Fuels*, vol. 3, no. 12, pp. 3279-3309, 2019.
- [37] Z. Gao *et al.*, "Promises, challenges, and recent progress of inorganic solid-state electrolytes for all-solid-state lithium batteries," *Advanced materials*, vol. 30, no. 17, p. 1705702, 2018.
- [38] D. H. Tan, A. Banerjee, Z. Chen, and Y. S. Meng, "From nanoscale interface characterization to sustainable energy storage using all-solid-state batteries," *Nature nanotechnology*, pp. 1-11, 2020.

- [39] A. Manthiram, X. Yu, and S. Wang, "Lithium battery chemistries enabled by solid-state electrolytes," *Nature Reviews Materials*, vol. 2, no. 4, pp. 1-16, 2017.
- [40] E. Peled, "The electrochemical behavior of alkali and alkaline earth metals in nonaqueous battery systems—the solid electrolyte interphase model," *Journal of The Electrochemical Society*, vol. 126, no. 12, p. 2047, 1979.
- [41] K. Kanamura, S. Shiraishi, and Z. i. Takehara, "Electrochemical deposition of very smooth lithium using nonaqueous electrolytes containing HF," *Journal of the Electrochemical Society*, vol. 143, no. 7, p. 2187, 1996.
- [42] Y. Ein-Eli, "A New Perspective on the Formation and Structure of the Solid Electrolyte Interface at the Graphite Anode of Li-Ion Cells," *Electrochemical and Solid State Letters*, vol. 2, no. 5, p. 212, 1999.
- [43] J. Thevenin and R. Muller, "Impedance of lithium electrodes in a propylene carbonate electrolyte," *Journal of The Electrochemical Society*, vol. 134, no. 2, p. 273, 1987.
- [44] J. Thevenin, "Passivating films on lithium electrodes. An approach by means of electrode impedance spectroscopy," *Journal of Power Sources*, vol. 14, no. 1-3, pp. 45-52, 1985.

- [45] G. Li *et al.*, "Organosulfide-plasticized solid-electrolyte interphase layer enables stable lithium metal anodes for long-cycle lithium-sulfur batteries," *Nature communications*, vol. 8, no. 1, pp. 1-10, 2017.
- [46] J. Zheng *et al.*, "Electrolyte additive enabled fast charging and stable cycling lithium metal batteries," *Nature Energy*, vol. 2, no. 3, pp. 1-8, 2017.
- [47] J. Qian *et al.*, "High rate and stable cycling of lithium metal anode," *Nature communications*, vol. 6, no. 1, pp. 1-9, 2015.
- [48] R. Weber *et al.*, "Long cycle life and dendrite-free lithium morphology in anode-free lithium pouch cells enabled by a dual-salt liquid electrolyte," *Nature Energy*, vol. 4, no. 8, pp. 683-689, 2019.
- [49] X. Q. Zhang, X. B. Cheng, X. Chen, C. Yan, and Q. Zhang, "Fluoroethylene carbonate additives to render uniform Li deposits in lithium metal batteries," *Advanced Functional Materials*, vol. 27, no. 10, p. 1605989, 2017.
- [50] L. Suo *et al.*, "Fluorine-donating electrolytes enable highly reversible 5-V-class Li metal batteries," *Proceedings of the National Academy of Sciences*, vol. 115, no. 6, pp. 1156-1161, 2018.

- [51] C. Yan *et al.*, "Toward Critical Electrode/Electrolyte Interfaces in Rechargeable Batteries," *Advanced Functional Materials*, p. 1909887, 2020.
- [52] X. B. Cheng, R. Zhang, C. Z. Zhao, F. Wei, J. G. Zhang, and Q. Zhang, "A review of solid electrolyte interphases on lithium metal anode," *Advanced Science*, vol. 3, no. 3, p. 1500213, 2016.
- [53] R. Pathak *et al.*, "Ultrathin bilayer of graphite/SiO₂ as solid interface for reviving Li metal anode," *Advanced Energy Materials*, vol. 9, no. 36, p. 1901486, 2019.
- [54] R. Pathak *et al.*, "Fluorinated hybrid solid-electrolyte-interphase for dendrite-free lithium deposition," *Nature communications*, vol. 11, no. 1, pp. 1-10, 2020.
- [55] A. Ostadhossein, S.-Y. Kim, E. D. Cubuk, Y. Qi, and A. C. Van Duin, "Atomic insight into the lithium storage and diffusion mechanism of SiO₂/Al₂O₃ electrodes of lithium ion batteries: ReaxFF reactive force field modeling," *The Journal of Physical Chemistry A*, vol. 120, no. 13, pp. 2114-2127, 2016.
- [56] Y.-Q. Wang *et al.*, "Rutile-TiO₂ nanocoating for a high-rate Li₄Ti₅O₁₂ anode of a lithium-ion battery," *Journal of the American Chemical Society*, vol. 134, no. 18, pp. 7874-7879, 2012.

- [57] S. Sim, P. Oh, S. Park, and J. Cho, "Critical Thickness of SiO₂ Coating Layer on Core@ Shell Bulk@ Nanowire Si Anode Materials for Li⁺ Ion Batteries," *Advanced Materials*, vol. 25, no. 32, pp. 4498-4503, 2013.
- [58] Y. Zhang, Y. Li, Z. Wang, and K. Zhao, "Lithiation of SiO₂ in Li-ion batteries: in situ transmission electron microscopy experiments and theoretical studies," *Nano letters*, vol. 14, no. 12, pp. 7161-7170, 2014.
- [59] X. Xiao, P. Lu, and D. Ahn, "Ultrathin multifunctional oxide coatings for lithium ion batteries," *Advanced Materials*, vol. 23, no. 34, pp. 3911-3915, 2011.
- [60] K. Yan *et al.*, "Ultrathin two-dimensional atomic crystals as stable interfacial layer for improvement of lithium metal anode," *Nano letters*, vol. 14, no. 10, pp. 6016-6022, 2014.
- [61] J.-S. Kim, D. W. Kim, H. T. Jung, and J. W. Choi, "Controlled lithium dendrite growth by a synergistic effect of multilayered graphene coating and an electrolyte additive," *Chemistry of Materials*, vol. 27, no. 8, pp. 2780-2787, 2015.
- [62] X. B. Cheng *et al.*, "Dendrite-Free Lithium Deposition Induced by Uniformly Distributed Lithium Ions for Efficient Lithium Metal Batteries," *Advanced Materials*, vol. 28, no. 15, pp. 2888-2895, 2016.

- [63] K. Liu *et al.*, "Extending the life of lithium-based rechargeable batteries by reaction of lithium dendrites with a novel silica nanoparticle sandwiched separator," *Advanced Materials*, vol. 29, no. 4, 2016.
- [64] E. Kazyak, K. N. Wood, and N. P. Dasgupta, "Improved cycle life and stability of lithium metal anodes through ultrathin atomic layer deposition surface treatments," *Chemistry of Materials*, vol. 27, no. 18, pp. 6457-6462, 2015.
- [65] C. Yan *et al.*, "Dual-Layered Film Protected Lithium Metal Anode to Enable Dendrite-Free Lithium Deposition," *Advanced Materials*, p. 1707629, 2018.
- [66] Y. Zhao *et al.*, "Inorganic-organic coating via molecular layer deposition enables long life sodium metal anode," *Nano letters*, vol. 17, no. 9, pp. 5653-5659, 2017.
- [67] R. Khurana, J. L. Schaefer, L. A. Archer, and G. W. Coates, "Suppression of lithium dendrite growth using cross-linked polyethylene/poly (ethylene oxide) electrolytes: a new approach for practical lithium-metal polymer batteries," *Journal of the American Chemical Society*, vol. 136, no. 20, pp. 7395-7402, 2014.
- [68] W. Xu *et al.*, "Lithium metal anodes for rechargeable batteries," *Energy & Environmental Science*, vol. 7, no. 2, pp. 513-537, 2014.

- [69] N. W. Li, Y. X. Yin, C. P. Yang, and Y. G. Guo, "An artificial solid electrolyte interphase layer for stable lithium metal anodes," *Advanced Materials*, vol. 28, no. 9, pp. 1853-1858, 2016.
- [70] R. Xu *et al.*, "Artificial soft–rigid protective layer for dendrite-free lithium metal anode," *Advanced Functional Materials*, vol. 28, no. 8, p. 1705838, 2018.
- [71] G. Zheng *et al.*, "Interconnected hollow carbon nanospheres for stable lithium metal anodes," *Nature nanotechnology*, vol. 9, no. 8, pp. 618-623, 2014.
- [72] Y. Zhao *et al.*, "Carbon paper interlayers: a universal and effective approach for highly stable Li metal anodes," *Nano Energy*, vol. 43, pp. 368-375, 2018.
- [73] H. Lee, J. Song, Y.-J. Kim, J.-K. Park, and H.-T. Kim, "Structural modulation of lithium metal-electrolyte interface with three-dimensional metallic interlayer for high-performance lithium metal batteries," *Scientific reports*, vol. 6, no. 1, pp. 1-10, 2016.
- [74] L. Wang, Q. Wang, W. Jia, S. Chen, P. Gao, and J. Li, "Li metal coated with amorphous Li_3PO_4 via magnetron sputtering for stable and long-cycle life lithium metal batteries," *Journal of Power Sources*, vol. 342, pp. 175-182, 2017.

- [75] Y. Zhang *et al.*, "Magnetron sputtering amorphous carbon coatings on metallic lithium: Towards promising anodes for lithium secondary batteries," *Journal of Power Sources*, vol. 266, pp. 43-50, 2014.
- [76] Q. Li *et al.*, "Homogeneous interface conductivity for lithium dendrite-free anode," *ACS Energy Letters*, vol. 3, no. 9, pp. 2259-2266, 2018.
- [77] L. Wang *et al.*, "Long lifespan lithium metal anodes enabled by Al₂O₃ sputter coating," *Energy Storage Materials*, vol. 10, pp. 16-23, 2018.
- [78] E. Cha *et al.*, "2D MoS₂ as an efficient protective layer for lithium metal anodes in high-performance Li-S batteries," *Nature nanotechnology*, vol. 13, no. 4, pp. 337-344, 2018.
- [79] A. C. Kozen *et al.*, "Next-generation lithium metal anode engineering via atomic layer deposition," *ACS nano*, vol. 9, no. 6, pp. 5884-5892, 2015.
- [80] Y. Liu *et al.*, "An ultrastrong double-layer nanodiamond interface for stable lithium metal anodes," *Joule*, vol. 2, no. 8, pp. 1595-1609, 2018.
- [81] H. Lee, D. J. Lee, Y.-J. Kim, J.-K. Park, and H.-T. Kim, "A simple composite protective layer coating that enhances the cycling stability of lithium metal batteries," *Journal of Power Sources*, vol. 284, pp. 103-108, 2015.

- [82] D. J. Lee, H. Lee, Y. J. Kim, J. K. Park, and H. T. Kim, "Sustainable redox mediation for lithium–oxygen batteries by a composite protective layer on the lithium–metal anode," *Advanced Materials*, vol. 28, no. 5, pp. 857-863, 2016.
- [83] Y. Liu *et al.*, "An artificial solid electrolyte interphase with high Li⁺ ion conductivity, mechanical strength, and flexibility for stable lithium metal anodes," *Advanced Materials*, vol. 29, no. 10, p. 1605531, 2017.
- [84] S. K. Cho *et al.*, "Printable Solid Electrolyte Interphase Mimic for Antioxidative Lithium Metal Electrodes," *Advanced Functional Materials*, p. 2000792, 2020.
- [85] G. Ma, Z. Wen, Q. Wang, C. Shen, J. Jin, and X. Wu, "Enhanced cycle performance of a Li–S battery based on a protected lithium anode," *Journal of Materials Chemistry A*, vol. 2, no. 45, pp. 19355-19359, 2014.
- [86] Z. Tu *et al.*, "Designing artificial solid-electrolyte interphases for single-ion and high-efficiency transport in batteries," *Joule*, vol. 1, no. 2, pp. 394-406, 2017.
- [87] M. S. Kim *et al.*, "Langmuir–Blodgett artificial solid-electrolyte interphases for practical lithium metal batteries," *Nature Energy*, vol. 3, no. 10, pp. 889-898, 2018.

- [88] P. Li *et al.*, "Anchoring an artificial solid–electrolyte interphase layer on a 3D current collector for high-performance lithium anodes," *Angewandte Chemie*, vol. 131, no. 7, pp. 2115-2119, 2019.
- [89] Z. Ju *et al.*, "Biomacromolecules enabled dendrite-free lithium metal battery and its origin revealed by cryo-electron microscopy," *Nature communications*, vol. 11, no. 1, pp. 1-10, 2020.
- [90] Y.-C. Yin *et al.*, "Metal chloride perovskite thin film based interfacial layer for shielding lithium metal from liquid electrolyte," *Nature communications*, vol. 11, no. 1, pp. 1-9, 2020.
- [91] D. Lin *et al.*, "Three-dimensional stable lithium metal anode with nanoscale lithium islands embedded in ionically conductive solid matrix," *Proceedings of the National Academy of Sciences*, vol. 114, no. 18, pp. 4613-4618, 2017.
- [92] C. P. Yang, Y. X. Yin, S. F. Zhang, N. W. Li, and Y. G. Guo, "Accommodating lithium into 3D current collectors with a submicron skeleton towards long-life lithium metal anodes," *Nature communications*, vol. 6, p. 8058, 2015.
- [93] F. Ding *et al.*, "Dendrite-free lithium deposition via self-healing electrostatic shield mechanism," *Journal of the American Chemical Society*, vol. 135, no. 11, pp. 4450-4456, 2013.

- [94] G. A. Umeda, E. Menke, M. Richard, K. L. Stamm, F. Wudl, and B. Dunn, "Protection of lithium metal surfaces using tetraethoxysilane," *Journal of Materials Chemistry*, vol. 21, no. 5, pp. 1593-1599, 2011.
- [95] C. Yan *et al.*, "Dual-layered film protected lithium metal anode to enable dendrite-free lithium deposition," *Advanced Materials*, vol. 30, no. 25, p. 1707629, 2018.
- [96] X. Liang *et al.*, "A facile surface chemistry route to a stabilized lithium metal anode," *Nature Energy*, vol. 2, no. 9, p. 17119, 2017.
- [97] X. Q. Zhang *et al.*, "Columnar lithium metal anodes," *Angewandte Chemie International Edition*, vol. 56, no. 45, pp. 14207-14211, 2017.
- [98] Y. Yuan *et al.*, "Regulating Li deposition by constructing LiF-rich host for dendrite-free lithium metal anode," *Energy Storage Materials*, vol. 16, pp. 411-418, 2019.
- [99] K. Liao *et al.*, "Developing a "Water-Defendable" and "Dendrite-Free" lithium-metal anode using a simple and promising GeCl_4 pretreatment method," *Advanced Materials*, vol. 30, no. 36, p. 1705711, 2018.
- [100] J. Yan, J. Yu, and B. Ding, "Mixed ionic and electronic conductor for Li-metal anode protection," *Advanced Materials*, vol. 30, no. 7, p. 1705105, 2018.

- [101] Z. Wang *et al.*, "Building Artificial Solid-Electrolyte Interphase with Uniform Intermolecular Ionic Bonds toward Dendrite-Free Lithium Metal Anodes," *Advanced Functional Materials*, p. 2002414, 2020.
- [102] F. Liu *et al.*, "A Mixed Lithium-Ion Conductive Li₂S/Li₂Se Protection Layer for Stable Lithium Metal Anode," *Advanced Functional Materials*, vol. 30, no. 23, p. 2001607, 2020.
- [103] H. Chen *et al.*, "Uniform high ionic conducting lithium sulfide protection layer for stable lithium metal anode," *Advanced Energy Materials*, vol. 9, no. 22, p. 1900858, 2019.
- [104] M. He, R. Guo, G. M. Hobold, H. Gao, and B. M. Gallant, "The intrinsic behavior of lithium fluoride in solid electrolyte interphases on lithium," *Proceedings of the National Academy of Sciences*, vol. 117, no. 1, pp. 73-79, 2020.
- [105] J. Zhao *et al.*, "Surface fluorination of reactive battery anode materials for enhanced stability," *Journal of the American Chemical Society*, vol. 139, no. 33, pp. 11550-11558, 2017.
- [106] D. Lin *et al.*, "Conformal lithium fluoride protection layer on three-dimensional lithium by nonhazardous gaseous reagent freon," *Nano letters*, vol. 17, no. 6, pp. 3731-3737, 2017.

- [107] K. Chen *et al.*, "Flower-shaped lithium nitride as a protective layer via facile plasma activation for stable lithium metal anodes," *Energy Storage Materials*, vol. 18, pp. 389-396, 2019.
- [108] J. Pan, Y. T. Cheng, and Y. Qi, "General method to predict voltage-dependent ionic conduction in a solid electrolyte coating on electrodes," *Physical Review B*, vol. 91, no. 13, p. 134116, 2015.
- [109] Y. Lu, Z. Tu, and L. A. Archer, "Stable lithium electrodeposition in liquid and nanoporous solid electrolytes," *Nature materials*, vol. 13, no. 10, p. 961, 2014.
- [110] S. Choudhury and L. A. Archer, "Lithium fluoride additives for stable cycling of lithium batteries at high current densities," *Advanced Electronic Materials*, vol. 2, no. 2, p. 1500246, 2016.
- [111] C. Yan *et al.*, "An armored mixed conductor interphase on a dendrite-free lithium-metal anode," *Advanced Materials*, p. 1804461, 2018.
- [112] X. Fan *et al.*, "Fluorinated solid electrolyte interphase enables highly reversible solid-state Li metal battery," *Science advances*, vol. 4, no. 12, p. eaau9245, 2018.
- [113] K. Kanamura, S. Shiraishi, and Z. I. Takehara, "Electrochemical deposition of very smooth lithium using nonaqueous electrolytes

- containing HF," *Journal of The Electrochemical Society*, vol. 143, no. 7, pp. 2187-2197, 1996.
- [114] Z. Tu *et al.*, "Fast ion transport at solid–solid interfaces in hybrid battery anodes," *Nature Energy*, vol. 3, no. 4, p. 310, 2018.
- [115] S. Choudhury *et al.*, "Electroless formation of hybrid lithium anodes for fast interfacial ion transport," *Angewandte Chemie International Edition*, vol. 56, no. 42, pp. 13070-13077, 2017.
- [116] K. Yan *et al.*, "Selective deposition and stable encapsulation of lithium through heterogeneous seeded growth," *Nature Energy*, vol. 1, no. 3, p. 16010, 2016.
- [117] M. T. Rahman *et al.*, "Metallic 1T Phase Tungsten Disulfide Microflowers for Trace Level Detection of Hg²⁺ Ions," *Advanced Sustainable Systems*, p. 2000068.
- [118] M. T. Rahman *et al.*, "Graphene oxide–silver nanowire nanocomposites for enhanced sensing of Hg²⁺," *ACS Applied Nano Materials*, vol. 2, no. 8, pp. 4842-4851, 2019.
- [119] Z. Lendzion-Bielun, U. Narkiewicz, and W. Arabczyk, "Cobalt-based catalysts for ammonia decomposition," *Materials*, vol. 6, no. 6, pp. 2400-2409, 2013.

- [120] T. Bell and L. Torrente-Murciano, "H₂ production via ammonia decomposition using non-noble metal catalysts: a review," *Topics in Catalysis*, vol. 59, no. 15-16, pp. 1438-1457, 2016.
- [121] A. K. Hill and L. Torrente-Murciano, "In-situ H₂ production via low temperature decomposition of ammonia: insights into the role of cesium as a promoter," *International Journal of Hydrogen Energy*, vol. 39, no. 15, pp. 7646-7654, 2014.
- [122] S. Phanichphant, "Semiconductor metal oxides as hydrogen gas sensors," *Procedia Engineering*, vol. 87, pp. 795-802, 2014.
- [123] C. Prajapati and P. Sahay, "Studies on metal-oxide semiconductor ZnO as a hydrogen gas sensor," *Journal of Nano-and Electronic Physics*, vol. 3, no. 1, p. 714, 2011.
- [124] H. Elbohy, K. M. Reza, S. Abdulkarim, and Q. Qiao, "Creation of oxygen vacancies to activate WO₃ for higher efficiency dye-sensitized solar cells," *Sustainable Energy & Fuels*, 2018.
- [125] C. Ramana, S. Utsunomiya, R. Ewing, C. Julien, and U. Becker, "Structural stability and phase transitions in WO₃ thin films," *The Journal of Physical Chemistry B*, vol. 110, no. 21, pp. 10430-10435, 2006.

- [126] S. Adhikari and D. Sarkar, "Electrochemical Response for Spherical and Rod Shaped WO_3 Nanoparticles," *ISRN Nanotechnology*, vol. 2013, 2013.
- [127] Y.-C. Nah, I. Paramasivam, R. Hahn, N. K. Shrestha, and P. Schmuki, "Nitrogen doping of nanoporous WO_3 layers by NH_3 treatment for increased visible light photoresponse," *Nanotechnology*, vol. 21, no. 10, p. 105704, 2010.
- [128] G. Wang *et al.*, "Hydrogen-treated WO_3 nanoflakes show enhanced photostability," *Energy & Environmental Science*, vol. 5, no. 3, pp. 6180-6187, 2012.
- [129] Y. H. Li *et al.*, "Local atomic structure modulations activate metal oxide as electrocatalyst for hydrogen evolution in acidic water," *Nature communications*, vol. 6, 2015.
- [130] A. S. Arico, P. Bruce, B. Scrosati, J.-M. Tarascon, and W. Van Schalkwijk, "Nanostructured materials for advanced energy conversion and storage devices," *Nature materials*, vol. 4, no. 5, p. 366, 2005.
- [131] R. Qing and W. Sigmund, "Morphological and crystallite size impact on electrochemical performance of electrospun rutile and rutile/multiwall carbon nanotube nanofibers for lithium ion batteries," *Ceramics International*, vol. 40, no. 4, pp. 5665-5669, 2014.

- [132] A. M. Bruck, C. A. Cama, C. N. Gannett, A. C. Marschilok, E. S. Takeuchi, and K. J. Takeuchi, "Nanocrystalline iron oxide based electroactive materials in lithium ion batteries: the critical role of crystallite size, morphology, and electrode heterostructure on battery relevant electrochemistry," *Inorganic Chemistry Frontiers*, vol. 3, no. 1, pp. 26-40, 2016.
- [133] J. Sottmann *et al.*, "How Crystallite Size Controls the Reaction Path in Nonaqueous Metal Ion Batteries: The Example of Sodium Bismuth Alloying," *Chemistry of Materials*, vol. 28, no. 8, pp. 2750-2756, 2016.
- [134] T. Anwar, W. Li, N. Hussain, W. Chen, R. U. R. Sagar, and L. Tongxiang, "Effect of Annealing Atmosphere Induced Crystallite Size Changes on the Electrochemical Properties of TiO₂ Nanotubes Arrays," *Journal of Electrical Engineering*, vol. 4, pp. 43-51, 2016.
- [135] B. Li *et al.*, "Mesoporous Tungsten Trioxide Polyaniline Nanocomposite as an Anode Material for High-Performance Lithium-Ion Batteries," *ChemNanoMat*, vol. 2, no. 4, pp. 281-289, 2016.
- [136] S. Yoon, S.-G. Woo, K.-N. Jung, and H. Song, "Conductive surface modification of cauliflower-like WO₃ and its electrochemical

- properties for lithium-ion batteries," *Journal of Alloys and Compounds*, vol. 613, pp. 187-192, 2014.
- [137] D. Lin *et al.*, "Layered reduced graphene oxide with nanoscale interlayer gaps as a stable host for lithium metal anodes," *Nature nanotechnology*, vol. 11, no. 7, pp. 626-632, 2016.
- [138] Q. Sun, B. Zhang, and Z.-W. Fu, "Lithium electrochemistry of SiO₂ thin film electrode for lithium-ion batteries," *Applied Surface Science*, vol. 254, no. 13, pp. 3774-3779, 2008.
- [139] N. Yan *et al.*, "Hollow porous SiO₂ nanocubes towards high-performance anodes for lithium-ion batteries," *Scientific reports*, vol. 3, p. 1568, 2013.
- [140] M. Miyachi, H. Yamamoto, H. Kawai, T. Ohta, and M. Shirakata, "Analysis of SiO anodes for lithium-ion batteries," *Journal of the electrochemical society*, vol. 152, no. 10, pp. A2089-A2091, 2005.
- [141] R. Pathak *et al.*, "Self-recovery in Li-metal hybrid lithium-ion batteries via WO₃ reduction," *Nanoscale*, vol. 10, no. 34, pp. 15956-15966, 2018.
- [142] K. Chen *et al.*, "Flower-Shaped Lithium Nitride as a Protective Layer via Facile Plasma Activation for Stable Lithium Metal Anodes," *Energy Storage Materials*, vol. 18, pp. 389-396, 2019.

- [143] A. M. Gaikwad, B. V. Khau, G. Davies, B. Hertzberg, D. A. Steingart, and A. C. Arias, "A high areal capacity flexible lithium-ion battery with a strain-compliant design," *Advanced Energy Materials*, vol. 5, no. 3, p. 1401389, 2015.
- [144] E. Cha *et al.*, "2D MoS₂ as an efficient protective layer for lithium metal anodes in high-performance Li-S batteries (vol 13, pg 521, 2018)," *NATURE NANOTECHNOLOGY*, vol. 13, no. 6, pp. 521-521, 2018.
- [145] Y.-H. Xu, S.-X. Zhao, Y.-F. Deng, H. Deng, and C.-W. Nan, "Improved electrochemical performance of 5 V spinel LiNi_{0.5}Mn_{1.5}O₄ microspheres by F-doping and Li₄SiO₄ coating," *Journal of Materiomics*, vol. 2, no. 3, pp. 265-272, 2016.
- [146] S.-Y. Kim and Y. Qi, "Property evolution of Al₂O₃ coated and uncoated Si electrodes: A first principles investigation," *Journal of The Electrochemical Society*, vol. 161, no. 11, pp. F3137-F3143, 2014.
- [147] C.-P. Yang, Y.-X. Yin, S.-F. Zhang, N.-W. Li, and Y.-G. Guo, "Accommodating lithium into 3D current collectors with a submicron skeleton towards long-life lithium metal anodes," *Nature communications*, vol. 6, p. 8058, 2015.

- [148] A. Gurung *et al.*, "Highly efficient perovskite solar cell photocharging of lithium ion battery using DC–DC booster," *Advanced Energy Materials*, vol. 7, no. 11, p. 1602105, 2017.
- [149] A. Gurung *et al.*, "Rear-Illuminated Perovskite Photorechargeable Lithium Battery," *Advanced Functional Materials*, p. 2001865, 2020.
- [150] J. Zheng *et al.*, "Highly Stable Operation of Lithium Metal Batteries Enabled by the Formation of a Transient High-Concentration Electrolyte Layer," *Advanced Energy Materials*, vol. 6, no. 8, p. 1502151, 2016.
- [151] L. Zhang, K. Zhang, Z. Shi, and S. Zhang, "LiF as an artificial SEI layer to enhance the high-temperature cycle performance of $\text{Li}_4\text{Ti}_5\text{O}_{12}$," *Langmuir*, vol. 33, no. 42, pp. 11164-11169, 2017.
- [152] C. Li *et al.*, "Two-dimensional molecular brush-functionalized porous bilayer composite separators toward ultrastable high-current density lithium metal anodes," *Nature communications*, vol. 10, no. 1, p. 1363, 2019.
- [153] W. Zhang *et al.*, "Colossal Granular Lithium Deposits Enabled by the Grain-Coarsening Effect for High-Efficiency Lithium Metal Full Batteries," *Advanced Materials*, p. 2001740, 2020.

- [154] P. M. Le *et al.*, "Excellent Cycling Stability of Sodium Anode Enabled by a Stable Solid Electrolyte Interphase Formed in Ether-Based Electrolytes," *Advanced Functional Materials*, p. 2001151, 2020.
- [155] X. C. Ren, X. Q. Zhang, R. Xu, J. Q. Huang, and Q. Zhang, "Analyzing Energy Materials by Cryogenic Electron Microscopy," *Advanced Materials*, p. 1908293, 2020.
- [156] F. Lin *et al.*, "Synchrotron X-ray analytical techniques for studying materials electrochemistry in rechargeable batteries," *Chemical reviews*, vol. 117, no. 21, pp. 13123-13186, 2017.
- [157] S.-M. Bak, Z. Shadike, R. Lin, X. Yu, and X.-Q. Yang, "In situ/operando synchrotron-based X-ray techniques for lithium-ion battery research," *NPG Asia Materials*, vol. 10, no. 7, pp. 563-580, 2018.
- [158] Y. Yan, C. Cheng, L. Zhang, Y. Li, and J. Lu, "Deciphering the Reaction Mechanism of Lithium–Sulfur Batteries by In Situ/Operando Synchrotron-Based Characterization Techniques," *Advanced Energy Materials*, vol. 9, no. 18, p. 1900148, 2019.
- [159] K. R. Adair, M. N. Banis, Y. Zhao, T. Bond, R. Li, and X. Sun, "Temperature-Dependent Chemical and Physical Microstructure of Li

- Metal Anodes Revealed through Synchrotron-Based Imaging Techniques," *Advanced Materials*, p. 2002550, 2020.
- [160] Z. Deng *et al.*, "Recent Progress on Advanced Imaging Techniques for Lithium-Ion Batteries," *Advanced Energy Materials*, p. 2000806.
- [161] S. Lou *et al.*, "Interface Issues and Challenges in All-Solid-State Batteries: Lithium, Sodium, and Beyond," *Advanced Materials*, p. 2000721, 2020.
- [162] X. Shen, R. Zhang, X. Chen, X. B. Cheng, X. Li, and Q. Zhang, "The Failure of Solid Electrolyte Interphase on Li Metal Anode: Structural Uniformity or Mechanical Strength?," *Advanced Energy Materials*, vol. 10, no. 10, p. 1903645, 2020.
- [163] M. Yan *et al.*, "Stabilizing polymer–lithium interface in a rechargeable solid battery," *Advanced Functional Materials*, vol. 30, no. 6, p. 1908047, 2020.
- [164] W. Ling *et al.*, "A Flexible Solid Electrolyte with Multilayer Structure for Sodium Metal Batteries," *Advanced Energy Materials*, vol. 10, no. 9, p. 1903966, 2020.
- [165] Q. Zhou *et al.*, "A Temperature-Responsive Electrolyte Endowing Superior Safety Characteristic of Lithium Metal Batteries," *Advanced Energy Materials*, vol. 10, no. 6, p. 1903441, 2020.

- [166] N. Wu *et al.*, "In Situ Formation of Li₃P Layer Enables Fast Li⁺ Conduction across Li/Solid Polymer Electrolyte Interface," *Advanced Functional Materials*, vol. 30, no. 22, p. 2000831, 2020.
- [167] H. Sun *et al.*, "High-Safety and High-Energy-Density Lithium Metal Batteries in a Novel Ionic-Liquid Electrolyte," *Advanced Materials*, p. 2001741, 2020.
- [168] X. Liu, J. Liu, T. Qian, H. Chen, and C. Yan, "Novel Organophosphate-Derived Dual-Layered Interface Enabling Air-Stable and Dendrite-Free Lithium Metal Anode," *Advanced Materials*, vol. 32, no. 2, p. 1902724, 2020.
- [169] Y. Ding, X. Guo, Y. Qian, L. Xue, A. Dolocan, and G. Yu, "Room-Temperature All-Liquid-Metal Batteries Based on Fusible Alloys with Regulated Interfacial Chemistry and Wetting," *Advanced Materials*, p. 2002577, 2020.
- [170] P. Zhai *et al.*, "In Situ Generation of Artificial Solid-Electrolyte Interphases on 3D Conducting Scaffolds for High-Performance Lithium-Metal Anodes," *Advanced Energy Materials*, vol. 10, no. 8, p. 1903339, 2020.

- [171] O. Sheng *et al.*, "In Situ Construction of a LiF-Enriched Interface for Stable All-Solid-State Batteries and its Origin Revealed by Cryo-TEM," *Advanced Materials*, p. 2000223.
- [172] D. Chen *et al.*, "In situ preparation of thin and rigid COF film on Li anode as artificial solid electrolyte interphase layer resisting Li dendrite puncture," *Advanced Functional Materials*, vol. 30, no. 7, p. 1907717, 2020.
- [173] Z. Wang *et al.*, "An Anion-Tuned Solid Electrolyte Interphase with Fast Ion Transfer Kinetics for Stable Lithium Anodes," *Advanced Energy Materials*, vol. 10, no. 14, p. 1903843, 2020.
- [174] C. Cui *et al.*, "A Highly Reversible, Dendrite-Free Lithium Metal Anode Enabled by a Lithium-Fluoride-Enriched Interphase," *Advanced Materials*, vol. 32, no. 12, p. 1906427, 2020.
- [175] Z. Peng *et al.*, "High-Power Lithium Metal Batteries Enabled by High-Concentration Acetonitrile-Based Electrolytes with Vinylene Carbonate Additive," *Advanced Functional Materials*, p. 2001285, 2020.
- [176] X. Chen *et al.*, "Lithiophilicity chemistry of heteroatom-doped carbon to guide uniform lithium nucleation in lithium metal anodes," *Science advances*, vol. 5, no. 2, p. eaau7728, 2019.

- [177] L. Li *et al.*, "Self-heating–induced healing of lithium dendrites," *Science*, vol. 359, no. 6383, pp. 1513-1516, 2018.
- [178] D. Cao *et al.*, "3D Printed High-Performance Lithium Metal Microbatteries Enabled by Nanocellulose," *Advanced Materials*, vol. 31, no. 14, p. 1807313, 2019.
- [179] R. Zhang, X. Shen, X.-B. Cheng, and Q. Zhang, "The dendrite growth in 3D structured lithium metal anodes: electron or ion transfer limitation?," *Energy Storage Materials*, vol. 23, pp. 556-565, 2019.